

Peter Micheuz, BSc

Structural and petrological studies of two selected high-pressure units within the Alpine orogen (External Hellenides, Eastern Alps)

MASTERARBEIT

zur Erlangung des akademischen Grades

Master of Science

Masterstudium Erdwissenschaften

eingereicht an der

Technischen Universität Graz

Betreuer

Priv.-Doz. Mag. Dr.rer.nat. Kurt Krenn

Institute of Earth Sciences
Mineralogy & Petrology, Universitätsplatz 2, A-8010 Graz

Ao.Univ.-Prof. Dr.phil. Harald Fritz
Geology & Paleontology, Heinrichstraße 26, A-8010 Graz

EIDESSTATTLICHE ERKLÄRUNG

AFFIDAVIT

Ich erkläre an Eides statt, dass ich die vorliegende Arbeit selbstständig verfasst, andere als die angegebenen Quellen/Hilfsmittel nicht benutzt, und die den benutzten Quellen wörtlich und inhaltlich entnommenen Stellen als solche kenntlich gemacht habe. Das in TUGRAZonline hochgeladene Textdokument ist mit der vorliegenden Masterarbeit identisch.

I declare that I have authored this thesis independently, that I have not used other than the declared sources/resources, and that I have explicitly indicated all material which has been quoted either literally or by content from the sources used. The text document uploaded to TUGRAZonline is identical to the present master's thesis.

Datum / Date

Unterschrift / Signature

Acknowledgements

First of all I thank my supervisors Prof. Kurt Krenn and Prof. Harald Fritz for their support and fruitful discussions all over the last years. I particularly thank Prof. Kurt Krenn for helping me through tough moments and for his patience to supervise this master thesis.

Additionally, I thank Prof. Walter Kurz for correcting the paper draft and all the nice discussions.

I thank Jürgen Neubauer for helping me with the SEM, Anton Pock for polishing the thin sections and all department members.

Special thanks to Manu for the common time in the Ötztal and numerous inimitable stories (sedimental im Dolomitenhotel).

Of course I thank my classmates who made studying and discussing a memorable time. Listing all of them would give a far too long list, that is why I want to bring up the most important. Thank you Cy, Isti, Klaus, Sara, Babsi, and Paul, we had a lot to laugh about at and beside university.

Last but not least I thank my beloved parents, brother, sister and girlfriend for their love and support, which always kept me going. I cannot even express how much you mean to me and I am glad to have you by my side.

Thank you all!

Abstract

This master thesis consists of two parts. The first part comprises a paper draft, which has been submitted to a special volume in the Austrian Journal of Earth Sciences. The study deals with the tectonic evolution of the Phyllite-Quartzite Unit within the external Hellenides, at Mani peninsula (Southern Peloponnese, Greece). Methods like field mapping, micro-structural and petrographic analysis of thin sections, mineral chemical analysis, microthermometry and Raman spectroscopy of fluid inclusions of different quartz veins have been applied. The aim of this study was to reconstruct the structural evolution and P/T conditions during exhumation of the Phyllite-Quartzite Unit. Four exhumation related deformation stages were distinguished: D1 - uniaxial stretching, D2 - rotational shearing and folding, D3 - folding and D4 - normal faulting. Fluid inclusion study of D4 - related extensional quartz boudin necks constrained maximum P/T conditions for D4 of ca. 6 kbar and 400°C. The results of the study were combined with published P-T paths representative for the study area and a new tectonic model was proposed.

The second part of the master thesis comprises a petrographic and structural study within the Ötztal Complex, at Vent and Obergurgl village (Tyrol, Austria). Currently the Ötztal Complex as part of the Ötztal-Bundschuh nappe system forms the upper plate of the eo-Alpine high-pressure wedge within the Austroalpine Units. Methods like field mapping, petrographic and structural analysis of thin sections, as well as mineral chemical analysis of representative samples have been applied. The aim of the study was to compare the Ötztal Complex with the basement of the eo-Alpine high-pressure wedge (Texel Complex). Five deformation stages have been distinguished, which seem to be comparable to already published deformation stages within the Texel Complex. Data combined with petrographic similarities between the Ötztal Complex and the Texel Complex could be an important evidence that the Texel Complex is the southern continuation of the Ötztal Complex, which means that they belong to the same tectonic plate before and during eo-Alpine formation of the high-pressure wedge.

Zusammenfassung

Diese Masterarbeit besteht aus zwei Teilen. Der erste Teil beinhaltet ein Manuskript, welches in einer Spezialausgabe des Austrian Journal of Earth Sciences eingereicht wurde. Die Studie beschäftigt sich mit der tektonischen Entwicklung der Phyllit-Quarzit Einheit innerhalb der externen Helleniden, auf der Halbinsel Mani (südliche Peloponnes, Griechenland). Methoden wie Feldkartierung, mikrostrukturelle und petrographische Untersuchungen von Dünnschliffen, chemische Analysen von Mineralen, Mikrothermometrie und Raman Spektroskopie von Flüssigkeitseinschlüssen unterschiedlicher Quarzgänge wurden angewendet. Das Ziel dieser Arbeit war die Rekonstruktion der strukturellen Entwicklung und der dazugehörigen Druck- und Temperaturbedingungen von Gesteinsproben der Phyllit-Quarzit Einheit zu erarbeiten. Dabei konnten vier Deformationsphasen unterschieden werden: D1 - uniaxiale Streckung, D2 - Scherung und Faltung, D3 - Faltung und D4 - dehnungsbezogene Abschiebungen. Flüssigkeitseinschlüsse aus mehreren Quarzdehnungsgängen ergeben maximale Druck- und Temperaturbedingungen für deren Bildung um ca. 6 kbar und 400°C. Die Resultate dieser Studie wurden mit bereits publizierten Druck- und Temperaturpfaden kombiniert um einen repräsentativen Pfad für das Untersuchungsgebiet zu erhalten. Des Weiteren wurde ein neues tektonisches Model für die Phyllit-Quarzit Einheit vorgeschlagen.

Der zweite Teil der Masterarbeit beinhaltet eine petrographische und struktureologische Studie innerhalb des Ötztal Komplexes, bei Vent und Obergurgl (Tirol, Österreich). Innerhalb der Ostalpinen Einheiten bildet der Ötztal Komplex, als Teil des Ötztal-Bundschuh Deckensystems, die Oberplatte zu einer liegenden eo-Alpinen Hochdruckeinheit. Methoden wie Feldkartierung, petrographische und struktureologische Analysen von Dünnschliffen, sowie chemische Analysen von repräsentativen Proben wurden durchgeführt. Das Ziel der Studie war es den Ötztal Komplex mit der eo-Alpinen Hochdruckeinheit (Texel Komplex) zu vergleichen. Dabei konnten fünf Deformationsphasen unterschieden werden, welche mit bereits publizierten Deformationsphasen innerhalb des Texel Komplexes vergleichbar sind. Verknüpft mit petrographischen Ähnlichkeiten zwischen dem Ötztal und dem Texel Komplex, könnten diese neuen Erkenntnisse einen Hinweis drauf geben, dass der Texel Komplex die südliche Fortsetzung des Ötztal Komplexes bildet. Dies würde beide Komplexe zur selben tektonischen Großeinheit vor und während der eo-Alpinen Entstehung der Hochdruckeinheit zählen.

Content

First part: Tectonic evolution of blueschist-facies rocks within the Phyllite-Quartzite Unit of the External Hellenides (Mani, Greece)	1.0 – 1.20
Appendix	1.21
Second part: Petrographic and structural analysis of the Ötztal Complex and surrounding tectonic units at Obergurgl and Vent	2.0 – 2.35
Appendix	2.36 – 2.51

First part

Tectonic evolution of blueschist-facies rocks within the Phyllite-Quartzite Unit of the External Hellenides (Mani, Greece)

Micheuz Peter, Krenn Kurt, Fritz Harald and Kurz Walter

Institute of Earth Sciences, University of Graz, Universitätsplatz 2, A-8010 Graz
(Austria)
(e-mail: peter.micheuz@edu.uni-graz.at)

Submitted to a special volume of the Austrian Journal of Earth Sciences.

Abstract

The Phyllite-Quartzite Unit (PQU) of the southern Peloponnese (Mani, Greece) experienced HP-LT metamorphism as result of eastward-directed subduction of the Adriatic plate beneath the Eurasian plate during the Late Oligocene to Early Miocene. On the basis of macro-, micro-scale and LPO textures the PQU experienced four deformation stages: D1 - uniaxial stretching, D2 - rotational shearing and folding, D3 - folding and D4 - extension. Superposition of D2 related shear folds F2 and subsequent open-spaced folds F3 (D3) indicate a large-scale F2/F3 fold interference pattern including relics of earliest F1 constriction folds. Microstructures of blueschist-facies micaschists contain chloritoid 1 porphyroblasts including an earliest foliation S1 which was overprinted by SSW directed shearing (D2). Blueschists show syngenetic chloritoid 1 and glaucophane, both rotated parallel to the dominant foliation S2 consisting of mica and graphite. Fluid inclusions microthermometry was performed using foliation-parallel shear band boudins (Qtz1) as well as late stage D4 extensional quartz boudin necks (Qtz2). Fluid data combined with rheological characteristics has been used to constrain conditions for deformation stages along a published P-T path representative for the southern Peloponnese. Fluid density isochores related to Qtz1 indicate density loss from peak conditions down to ca. 6 kbar along non-isochoric exhumation (isothermal decompression between 450-500°C) and deformation stages D1-D3. Conditions < 6 kbar and 400°C for deformation stage D4 has been derived by primary fluid inclusions in Qtz2 subsequent to isobaric cooling.

Introduction

High pressure (HP) and low temperature (LT) rocks provide a solid base to understand mineral reactions in subduction zones combined with subsequent exhumation processes. Related ductile structures can record early deformation stages after and/or during peak metamorphism. Beside conventional analytical methods minimum conditions for ductile and/or brittle deformation overprint can be determined by fluid inclusion microthermometry on late stage discordant quartz-bearing extensional veins (e.g. Krenn et al., 2008; Krenn, 2010). In the External Hellenides, the Phyllite-Quartzite Unit (PQU) contains blueschist-facies rocks of Oligocene-Miocene age that record a HP-LT evolution (e.g. Katagas, 1980; Ring et al., 2001). Previous studies related to the PQU focussed on regions on Crete and the central Peloponnese but are rare in the region on the Mani peninsula in the southern Peloponnese (e.g. Chatzaras et. al, 2006; Jolivet, et al., 2010). Here, fluid inclusion microthermometry linked with structural data is presented in order to constrain the tectonometamorphic history of the PQU.

Geological setting

The Hellenides as part of the Alpine orogen extend from northwestern Greece to the Peloponnese and continue towards Crete and Rhodos (Fig. 1). They are divided into an internal and external part by the so-called Pindos Ophiolitic Suture Zone (Smith, Woodcock and Naylor, 1979). The external part contains a HP-LT-belt which contours the Hellenic arc. HP-LT metamorphism resulted from northeastward subduction of the Adriatic plate (southern margin of the Apulian plate after Schmid et al., 2008) beneath the Eurasian plate which was followed by an extensive up to 1000 km large south-directed slab-retreat during Late Oligocene-Miocene time (e.g., Jolivet and Faccenna, 2000; Jolivet et al., 2003). The HP units of the External Hellenides were exhumed during sustained underplating which compensated crustal thinning along a N(E)-dipping detachment in the hanging-wall of the PQ unit (Ring et al., 2001, 2007; Ring and Reischmann, 2002).

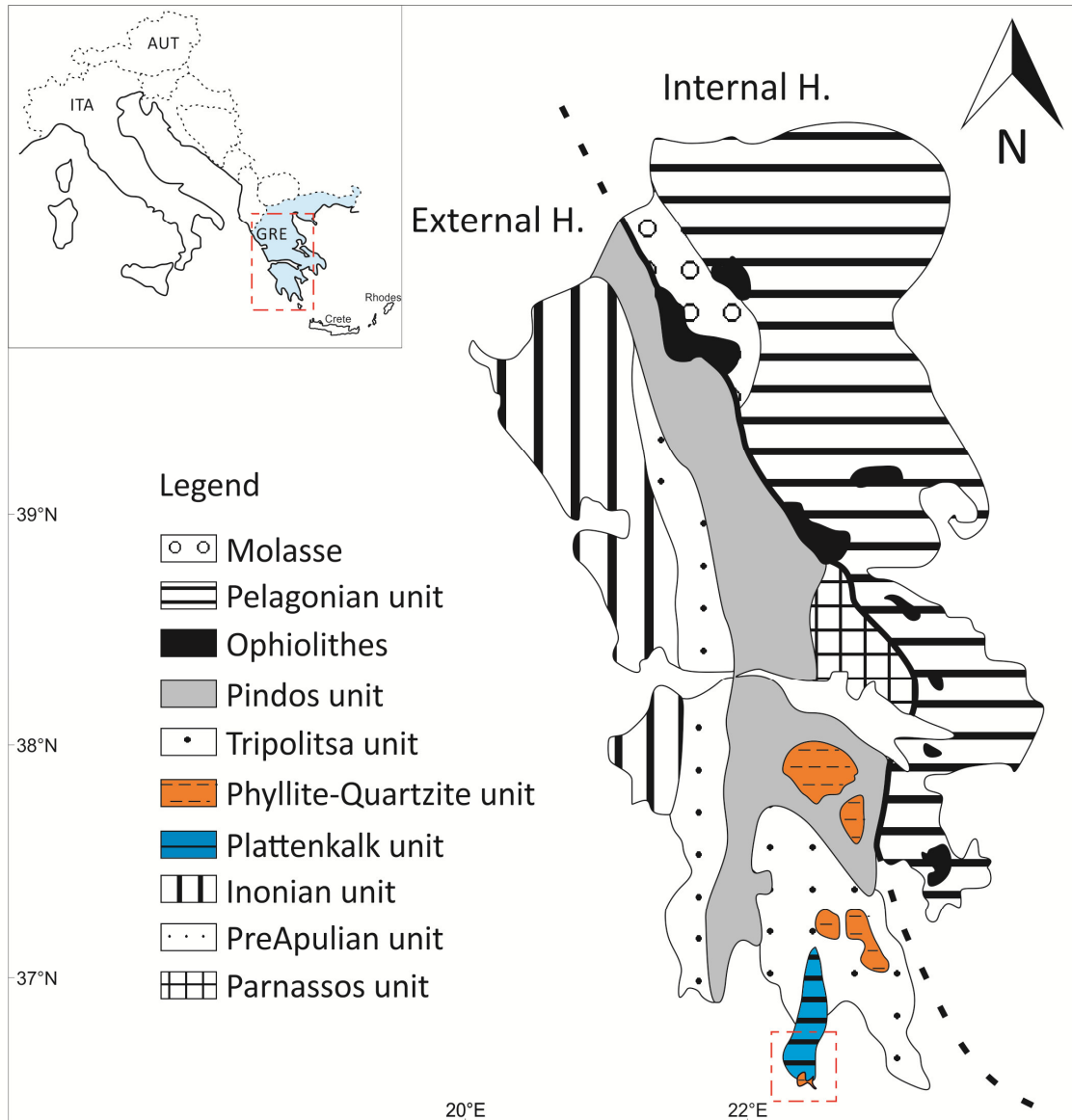


Figure 1 Geological overview of the Hellenides modified after Jacobshagen et al. (1986). Red rectangle in the southernmost area of the Peloponnese indicates study area at the Mani peninsula.

Tectonostratigraphically, the external Hellenides are divided into upper and lower tectonic units (Fig. 2). The lower tectonic units consist of the PQU on top and the Plattenkalk unit with peak metamorphism during Late Oligocene to Early Miocene times (e.g., Chatzaras et al., 2006). In contrast the upper tectonic units have not suffered high-grade metamorphism and are characterized as cover thrust sheets.

Main tectonic units		Lithology / protolith age	Peak metamorphic conditions age
Upper tectonic units	Uppermost unit	 Serpentinites (<i>Ophiolitic subunit</i>) / U. Jurassic  Amphibolites, gneisses, pillow-lavas, pelagic limestones and clastic sediments (<i>Ophiolitic mélange</i>) / U. Jurassic	low-pressure/high-temperature (4-6 kbar/650-700°C) Late Cretaceous
	Pindos unit	 Flysch deposits / Eocene  Deep-water carbonate rocks / Triassic-Paleocene	—
	Tripolitsa unit	 Flysch deposits / U. Eocene-Oligocene  Shallow-water carbonate rocks / Triassic-Eocene	low-pressure/low-temperature (~ 3 kbar/~ 250°C)
Lower tectonic units	Phyllite-Quartzite unit	 Eliated massive marbles and metavolcanic rocks (<i>Vasiliko unit</i>)  Phyllites, quartzites and metaconglomerates with marble intercalations / U. Carboniferous-Triassic	unknown high-pressure/low-temperature (10 ± 3 kbar/400 ± 50°C) Late Oligocene-Early Miocene
	Plattenkalk unit	 Flysch deposits / M. Oligocene  Marbles with nodular cherts / L. Jurassic-Eocene  Dolomitic marbles / U. Triassic-L. Jurassic  Marbles and schists / U. Carboniferous-U. Triassic	high-pressure/low-temperature (7 - 10 kbar/~ 350°C) Late Oligocene-Early Miocene

Figure 2 Tectonostratigraphy of the main tectonic units of the external Hellenides after Chatzaras et al. (2006). Circle shows tectonostratigraphic level of the study area.

The allochthonous PQU is represented by phyllites, quartzites, metaconglomerates and marbles and corresponds to an Upper Carboniferous to Triassic rift sequence (Robertson, 2006). Trotet et al. (2006) differentiated the PQU by its metamorphic evolution into the *Alagonia Unit* composed of greenschist-facies micaschists with chloritoid and albite; the *Metaconglomerate Unit* consisting of blueschist-facies metaconglomerates and micaschists; the *Lada Unit* built up by HT blueschist-facies micaschists with garnet and glaucophane and the *Blueschists Unit* made up of blueschist-facies micaschists with chloritoid and lenses of glaucophanites. The underlying Plattenkalk Unit is represented by layers of Upper Carboniferous to Eocene carbonates (Bonneau, 1973; Krahl et al., 1988) with a thin sequence composed of Middle Oligocene flysch on top (Bizon et al., 1976) (Fig. 2). On the Peloponnese the lack of HP-LT minerals within the Plattenkalk Unit supports the assumption that the PQU was thrust onto the Plattenkalk Unit during exhumation from HP conditions (e.g. Doutsos et al., 2000). According to Blumör et al. (1994) P-T conditions for the Plattenkalk Unit on the Peloponnese are 7 - 8 kbar and 310 - 360 °C.

Peak metamorphism within the PQU changes from the northern Peloponnese to Crete due to (a) different velocities of slab retreat, (b) the type of subduction channel and (c) the circulation characteristics of exhuming material (Jolivet et al., 2010). Thus temperature variations from 550°C in the northern part of the Peloponnese down to 400 ± 50°C in Crete at peak pressures of ~ 13 - 18 kbar occur. In the investigated area peak conditions for the PQU are 13 - 17 kbar and ca. 450 °C (e.g. Xypolias, 2007).

Analytical Methods

Mineral chemical analysis of silicate phases on polished thin sections were performed with a scanning electron microscope JEOL JSM-6310, attached to a wavelength dispersive system with an acceleration voltage of 15 kV, at the University of Graz, Institute of Earth Sciences (Department of Mineralogy and Petrology).

Lattice preferred orientation (LPO) patterns of quartz have been performed to analyse deformation geometries and shear directions. Therefore the software package “crystal imaging system G50 Fabric Analyser” by Russell-Head Instruments was used to estimate quartz $\langle c \rangle$ axis [001] data. Contoured stereograms were generated using Fabric 8 by Wallbrecher (2013). Shear directions were determined with respect to the foliation.

To obtain minimum conditions for deformation stages in the PQU, fluid inclusion microthermometry on concordant and discordant quartz boudin structures were performed. Primary fluid inclusions should additionally give important information about the fluid which was present during quartz vein precipitation. Fluid inclusion microthermometry was combined with micro-Raman spectroscopy on doubly polished thick sections (~ 0.15 mm) using a LINKAM THSMG600 heating - freezing stage with an operating range from -196°C up to +600°C (Shepherd, Rankin and Alderton, 1985), at the University of Graz, Institute of Earth Sciences (Department of Mineralogy and Petrology). Thermally - induced phase transition temperatures, densities and chemical systems of fluid inclusions were observed to determine metamorphic formation conditions for host minerals like the concordant and discordant quartz veins within the blueschists-facies micaschists.

Microthermometry was performed to evaluate phase transition temperatures. Abbreviations and terminology is after Diamond (2003): apparent eutectic temperature T_e (Antarcticite+Hydrohalite+Ice+V \rightarrow Hydrohalite+Ice+L+V); final melting temperature T_m (Ice+L+V \rightarrow L+V), e.g. T_m (Ice), T_m (Hydrohalite), T_m (Halite); total homogenisation temperature T_h (L+V \rightarrow L or V).

Fluid inclusion compositions were determined using the three component system H₂O-NaCl-CaCl₂ based on Steele-MacInnis et al. (2010). In order to identify constituents in wt. % (e.g. X_{NaCl} , X_{CaCl_2}) final melting temperature of halite was evaluated in the H₂O-NaCl-CaCl₂ system. To determine the $X_{NaCl}:X_{CaCl_2}$ ratio observations of Samson and Walker (2000) were used. Densities and amount-of-substance fractions were calculated with the software BULK (Bakker, 2003). Therefore T_m (Ice), T_h and relative NaCl- and

CaCl₂-values with equations according to Naden (1996) and Oakes et al. (1990) in a manually defined system (H₂O-NaCl-CaCl₂) was used. Salinity of solid phase halite was calculated after Bodnar (2003). Isochores were estimated with the software ISOC (Bakker, 2003) using the equation of state after Zhang and Frantz (1987).

Low temperature micro-Raman spectroscopy down to -190 °C with a HORIBA JOBIN YVON LabRam-HR 800 micro-Raman spectrometer has been performed at the University of Graz. A 50 mW Ar⁺-laser with the 532 nm emission line through an OLYMPUS 100X objective (N.A. 0.9) was used. Thus a laser spot with a diameter of about 1 µm and a power of 20 mW was produced on the sample surface. To disperse the light a holographic grating with 1800 grooves/mm was used. A 1024 x 256 open electrode CCD detector collected the dispersed light. In order to determine the spectral resolution (~ 1.8 cm⁻¹) the Rayleigh line of a polished single crystal siliconwafer has been measured. To assure an accuracy of Raman band shifts better than 0.5 cm⁻¹ the zero-order position of the grating were regularly adjusted and controlled by measuring the Rayleigh line. The detection range for measured crystals of the host rock was 100 - 1600 cm⁻¹ and for frozen fluid inclusions 2800 to 3700 cm⁻¹.

Field mapping and macrostructures

The mapped area comprises rocks according to the PQU, such as blueschist-facies micaschists, blueschists, metaconglomerates, and quartzites, and rocks belonging to the Plattenkalk Unit, which are medium-grade marbles and calcareous micaschists with inclusions of elongated marble clasts and boulders. Structural mapping of an area of about 4 km² revealed the distinction of three deformation stages. Deformation stage D1 is rarely preserved and related to structures resulting from uniaxial stretching near peak HP metamorphic conditions. D1 is characterized by tight constrictional F1 folds with steep SW-plunging fold axes (Fig. 3a). The occurrence of F1 is restricted to blueschist facies rocks, i.e. glaucophane - chloritoid-rich lithologies arranged as lenses and layers within quartz-rich metaconglomerates (Fig. 3b). Deformation stage D2 is characterized by SW-directed shearing and the occurrence of asymmetric shear folds F2 with S- to SE-plunging fold axes (Fig. 3c). Deformation stage D3 is characterized by open-spaced F3-folds with shallow W-E trending fold axes (Fig. 3d). Superposition of folding events F2 and F3 forms a large, km-scale type-2 fold interference pattern (referring to Ramsay, 1967) (Fig. 4). Early quartz-filled extensional veins occur frequently and indicate

predominantly N-S directed extension (deformation stage D4). These extensional veins were sampled for fluid inclusion analysis.

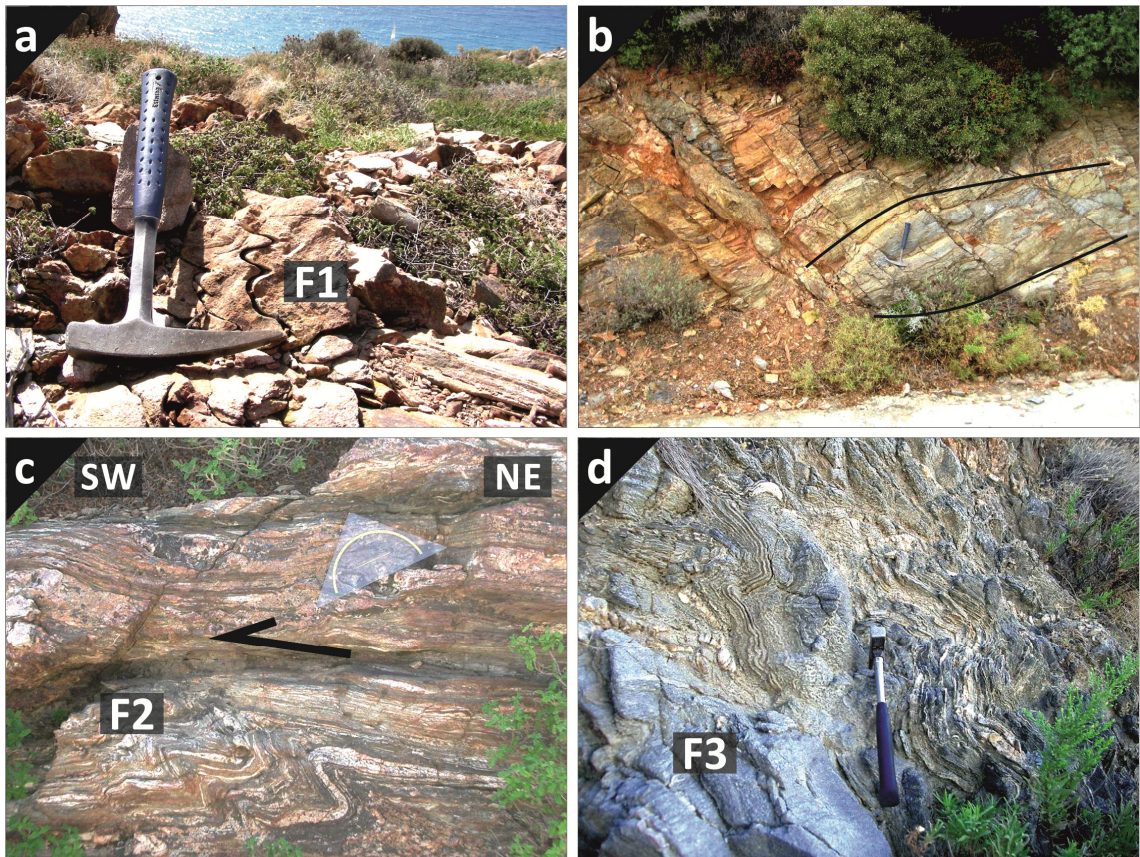


Figure 3 (a) F1 constriction folds in blueschist-facies micaschists. (b) Boudin within blueschist consisting of uniaxial stretched glaucophane-, zoisite- and chloritoid-bearing layers. (c) Asymmetric F2 shear folds indicating SW/SSW- shear direction (D2). (d) Open-spaced F3 folds with subhorizontal W-E trending fold axes (D3).

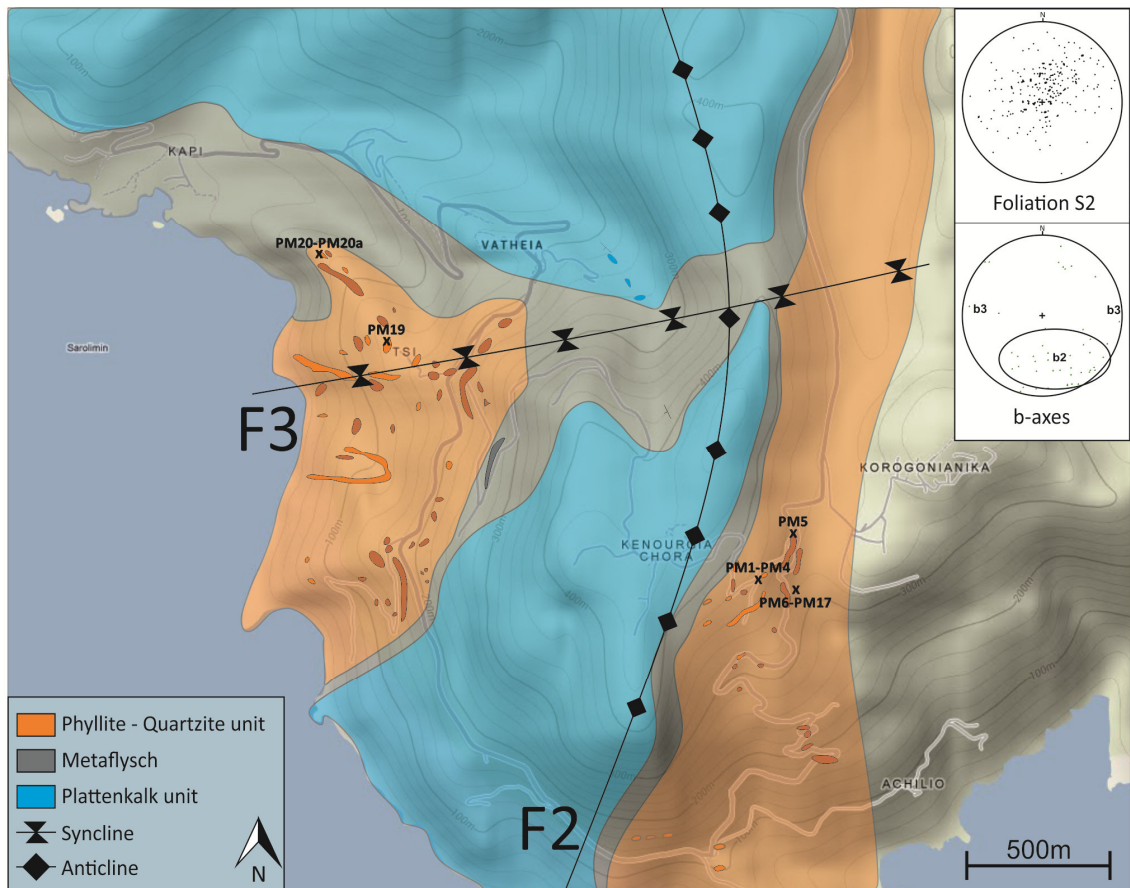


Figure 4 Mapped area of the Mani peninsula. A large-scale fold interference pattern results from superposition of F2 and F3.

Petrography and structural analysis

Blueschists, metaconglomerates and quartzites are embedded as layers and boudins in blueschist-facies micaschists.

Blueschists

The dominant deformation event in blueschists is uniaxial stretching D1. The mineral assemblage is glaucophane + chloritoid 1 + phengite + quartz. Glaucophane forms elongated grains (up to 2.5mm in-size) and is together with chloritoid 1 always aligned parallel to S2, and surrounded by phengite and quartz (Figs. 5a/b).

After Leake et al. (1997) and Mogessie et al. (2004) amphiboles can be classified as sodic, with glaucophane as end member (Figs. 6a/b). Na₂O contents range between 7.68 and 8.41 wt. %. CaO (0.32 wt. %) and K₂O (0.12 wt. %) are only present in trace amounts. Compared to FeO values (~ 13.9 wt. %), MgO values (~ 9.5 wt. %) are significantly lower.

Chloritoid 1 exhibits FeO contents between 24.47 and 26.83 wt. %, average MgO of ~ 2.74 wt. % and insignificant values for MnO (0.01 - 0.94 wt. %).

Phengites display average K₂O, FeO and MgO values of ~ 7.72 wt. %, ~ 4.54 wt. % and ~ 3.28 wt. %, respectively.

Blueschist-facies micaschists

Micaschists consist of two generations of chloritoid (Cld1 and Cld2) + phengite + paragonite + chlorite + graphite + quartz. Syndeformative chloritoid porphyroblasts (Cld1) with up to 2 mm in size contain an earlier internal foliation S1 (D1) and are retrogressed to white mica (phengite), chlorite and graphite. This retrogression was contemporaneous to SSW-directed shearing, that formed the dominant macroscale foliation S2 (D2) (Fig. 5c). Texturally, the internal foliation S1 continues into the external foliation S2. Chloritoid 2 (Cld2) reaches a size of up to 0.8 mm and is texturally arranged in clusters or as foliation-parallel grains up to 1.8 mm. Quartz (< 0.7 mm in size) dominates within the fine grained matrix but is also found as much smaller crystals (< 0.05 mm in size) within pressure shadows (Fig. 5d). The matrix quartz shows typical features of grain boundary migration recrystallization (GBM), such as elongated grains and lobate grain boundaries.

Compared to chloritoid compositions in blueschists (Cld1), those in blueschist-facies micaschists (Cld2) display lower FeO values (22.50 - 24.20 wt. %). MgO contents, however, exhibit average amounts of ~ 2.32 wt. %, showing a similar MgO content as chloritoids within the blueschists. Phengites show FeO and MgO values up to 2.3 wt. % and 2.99 wt. %, respectively. Due to exchange reactions with paragonite their Na₂O contents can reach up to 2.52 wt. %. The ones aligned parallel to the foliation however, exhibit higher MgO contents (3.5 - 4.04 wt. %). Their Na₂O values do not exceed 0.2 wt. %.

Paragonites, when in contact with phengites, display Na₂O values between 5.37 and 8.14 wt. %, whereas FeO (~ 0.72 wt. %) and MgO (~ 0.4 wt. %) are present in trace amounts.

Metaconglomerates

Metaconglomerates consist of quartz + feldspar + chloritoid 2 + mica ± glaucophane. Glaucophane and chloritoid are rather rarely preserved. Feldspar clasts are surrounded by asymmetrically arranged strain shadows that show shearing towards NNE.

Quartzites

Quartzites consist of quartz + chloritoid 2 + mica + chlorite. Accessories are represented by tourmaline and rutile. Fine grained quartz and chloritoid build up the matrix with grain sizes up to 0.5 mm and 1 mm, respectively. Chloritoid is arranged as clusters and widely distributed, overgrowing the penetrative foliation S2; this suggests post-deformative with regard to D2. Deformation mechanisms in quartz are referred to grain boundary migration, indicative for minimum temperatures of about 500 °C (Fig. 5e).

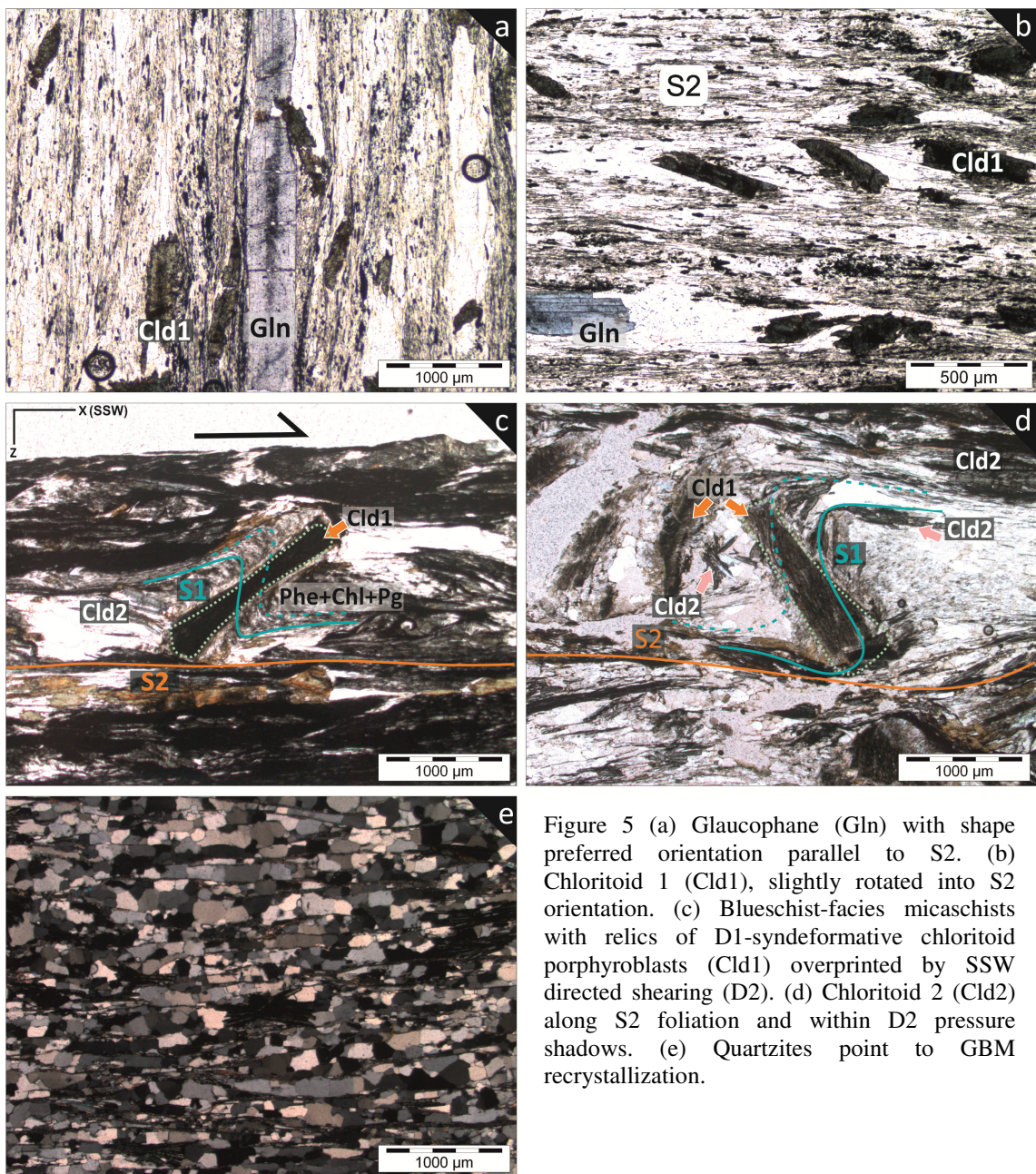


Figure 5 (a) Glaucophane (Gln) with shape preferred orientation parallel to S2. (b) Chloritoid 1 (Cld1), slightly rotated into S2 orientation. (c) Blueschist-facies micaschists with relics of D1-synformative chloritoid porphyroblasts (Cld1) overprinted by SSW directed shearing (D2). (d) Chloritoid 2 (Cld2) along S2 foliation and within D2 pressure shadows. (e) Quartzites point to GBM recrystallization.

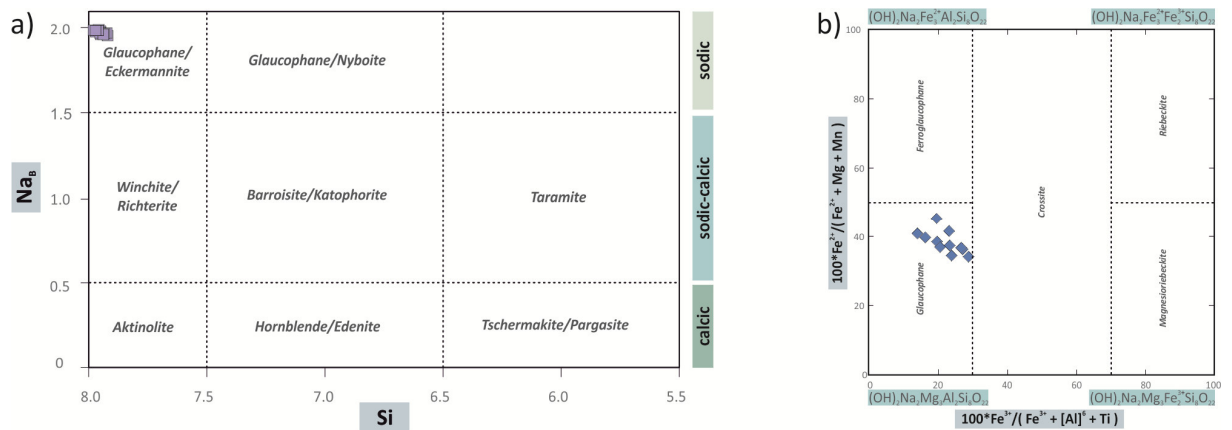


Figure 6 (a) Amphibole classification after Leake et al. (1997) and Mogessie et al. (2004). Chemistry of studied amphiboles plots in the glaucophane field. (b) Mineral chemistry of sodic amphiboles in a $100 * Fe^{2+} / (Fe^{2+} + Mg + Mn)$ vs. $100 * Fe^{3+} / (Fe^{3+} + [Al]^6 + Ti)$ diagram. Chemical compositions indicate glaucophane.

Lattice preferred orientation of quartz

Blueschist-facies micaschists show a symmetric great circle distribution of quartz c-axes along the y-z plane that is typical for D1-uniaxial stretching (Figs. 7a/b). Quartz grains (< 0.7 mm in size) within the fine grained layers exhibit grain boundary recrystallization indicative for temperatures > 500°C (Passchier and Trouw, 2005).

Fine-grained layers of metaconglomerates show quartz grains (< 0.6 mm in size), which exhibit undulatory extinction and show bulges, as well as core and mantle textures (Fig. 7c). Lattice preferred orientations are characterized by dominant maxima at y, which points to prism <a> gliding. Further active glide systems are assumed to be rhomb <a> and basal <a> gliding. A cross-girdle distribution pattern of type 1 (Lister, 1977) indicates shearing towards SW, according to D2.

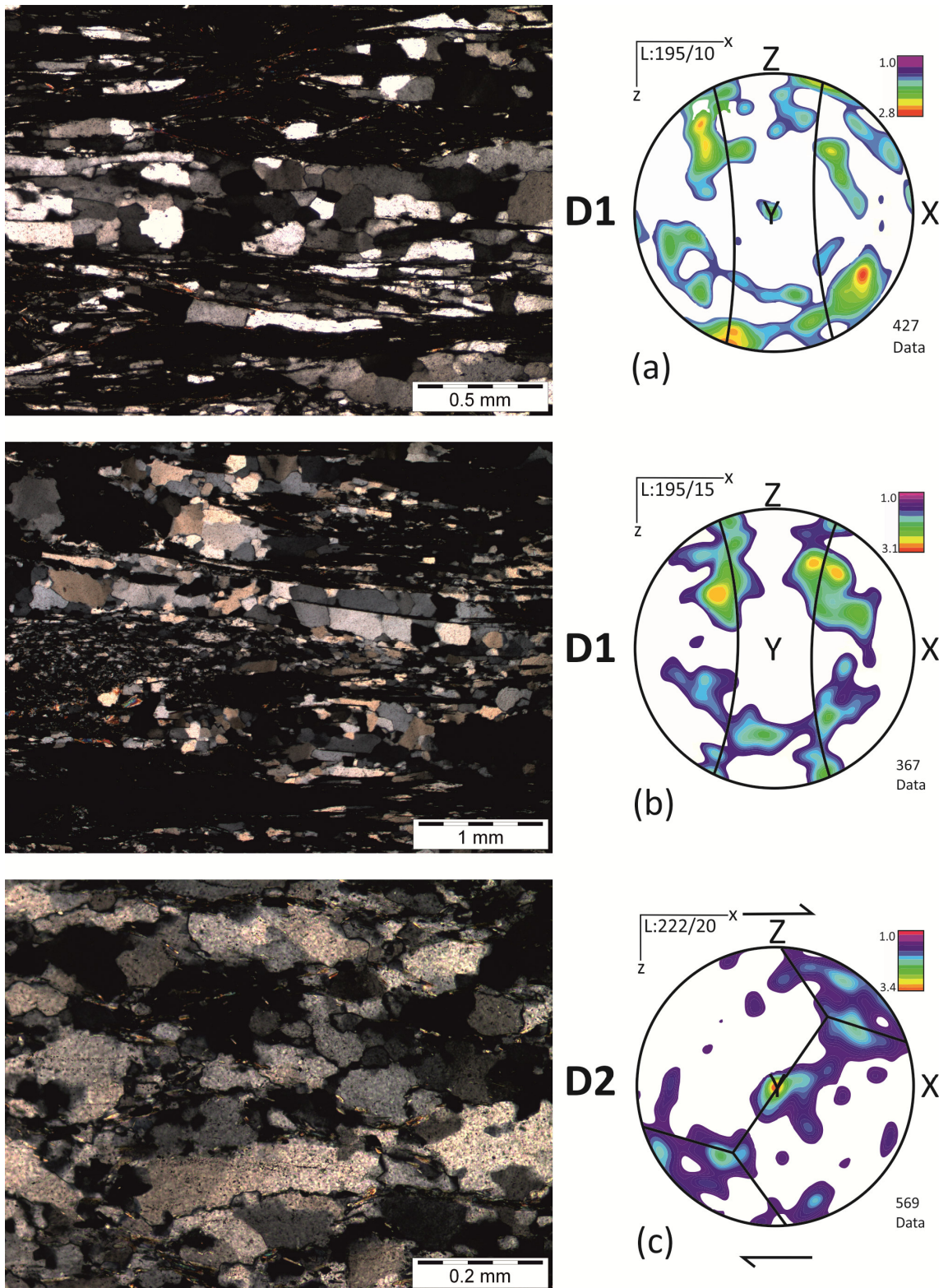


Figure 7 LPO plots combined with microstructures from the blueschist-facies micaschists (a/b) and metaconglomerates (c). (a) & (b) Fine grained quartz (< 0.7 mm) showing grain boundary migration (GBM) recrystallization. Quartz c-axes distributions indicate uniaxial stretching (D1). (c) Quartz (< 0.6 mm) shows undulatory extinction as well as bulging recrystallization and core-mantle textures. Quartz-c-axes distribution displays a cross-girdle pattern of type 1 after Lister (1977). Asymmetry points to SW-directed shearing (D2).

Fluid Inclusion study

Fluid inclusion microthermometry from doubly polished thick sections was performed on representative samples from a foliation-parallel quartz boudin (Qtz1) and a D4-related quartz-filled boudin neck (Qtz2) (Figs. 8a/b) (Appendix 1). No useful fluid inclusions were found in the surrounding host rocks (blueschists and blueschist-facies micaschists). Qtz1 consist mainly of recrystallized fine-grained quartz grains (≤ 0.8 mm) which are overgrown by euhedral dolomite crystals (≤ 1.2 mm) (Fig. 8c). Dolomite was identified by Raman spectroscopy (e.g. Baumgartner and Bakker, 2010). No dolomite crystals have been found as solid phase in fluid inclusions. The quartz filled necks (Qtz2) consist of coarse grained quartz (> 3 mm) and do not contain dolomite. Qtz1 in general displays fluid inclusions along fluid inclusion planes (Fig. 8d). Qtz2 exhibits fluid inclusions arranged mainly as single clusters (Fig. 8e) or along intragranular fluid inclusion planes.

In general, fluid inclusions display a homogeneous saline fluid which occurs both in Qtz1 and Qtz2. On the basis of eutectic temperatures T_e , microthermometry indicates a $H_2O-NaCl-CaCl_2$ chemical system, with halite daughter crystals as solid phase (Figs. 8d/e). After cooling down to -190°C heat runs indicate a first change in the relief of fluid inclusions in Qtz1 from darkening to granular at temperatures between -73 and -71°C , which is seen as a metastable behavior of antarctite during melting (e.g. Samson and Walker, 2000). In Qtz2 fluid inclusions show this relief change between -75 to -73°C . Final melting of ice $T_m(\text{Ice})$ in Qtz1 and Qtz2 occurred before final melting of hydrohalite and was observed at temperatures from -50 to -47°C and -51 to -49°C , respectively. The final melting of a solid phase assumed to be hydrohalite occurred around -35°C . The range in homogenization temperatures T_h of fluid inclusions in Qtz1 (180 to 248°C) and Qtz2 (120 to 182°C) result in different density ranges from 1.19 to 1.13 g/cm^3 and 1.24 to 1.17 g/cm^3 , respectively. Melting of halite occurred between 290 and 390°C in Qtz1 and between 270 and 387°C in Qtz2 indicating almost the same salinities between 36 and 46 wt\% after Bodnar (2003). Evidence for a non-isochoric P-T evolution of the host rocks Qtz1 and Qtz2 is given by decrepitation textures which indicate isothermal decompression (ITD) in Qtz1 and isobaric cooling (IBC) in Qtz2 after Vityk and Bodnar (1995) (Figs. 8f/g). Respective isochores for both types of quartz boudin structures are given in Fig. 8h.

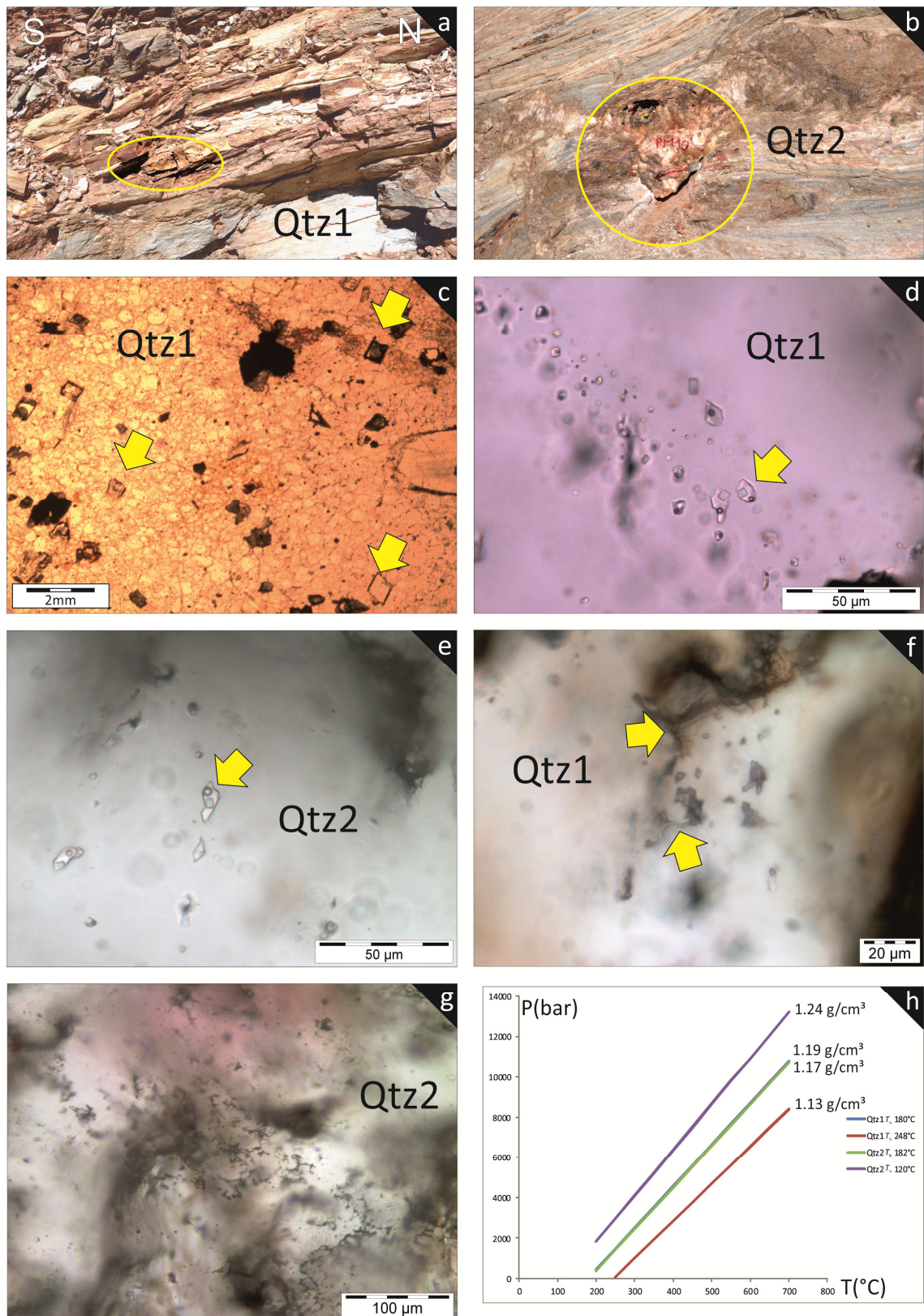


Figure 8 (a) Concordant quartz boudin (Qtz1). (b) Boudin neck filled with Qtz2. (c) Recrystallized fine-grained quartz matrix (Qtz1) including large mm-scale dolomite crystals (yellow arrows). (d) Polyphase (L,V,S) fluid inclusions arranged along intragranular fluid inclusion planes (Qtz1). (e) Polyphase (L,V,S) single fluid inclusions in Qtz2. (f) Hook-like morphology and planes of small inclusions (see arrows) indicative for ITD after Vityk and Bodnar (1995). (g) Irregular dendritic inclusion texture in Qtz2 indicating IBC after Vityk and Bodnar (1995). (h) Calculated isochores from fluid inclusions (densities between 1.19 and 1.13 g/cm^3 for Qtz1 and 1.24 to 1.19 g/cm^3 for Qtz2).

Low temperature Raman spectroscopy of fluid inclusions from Qtz1 shows peaks being typical for a mixture of hydrohalite and antarcticite in the range between -190 to -50°C and a significant broad peak for hydrohalite up to temperatures near 0°C . This points to a metastable behavior of hydrohalite in most fluid inclusions (Fig. 9). A similar intensity of the 3404 and 3436 cm^{-1} peaks is indicative for a fluid composition of $X_{\text{NaCl}}/X_{\text{CaCl}_2} = 2:1$ (after Samson and Walker, 2000). At higher temperatures (up to -20°C) the dominant peaks at 3423.77 cm^{-1} and 3544.58 cm^{-1} can be clearly attributed to hydrohalite.

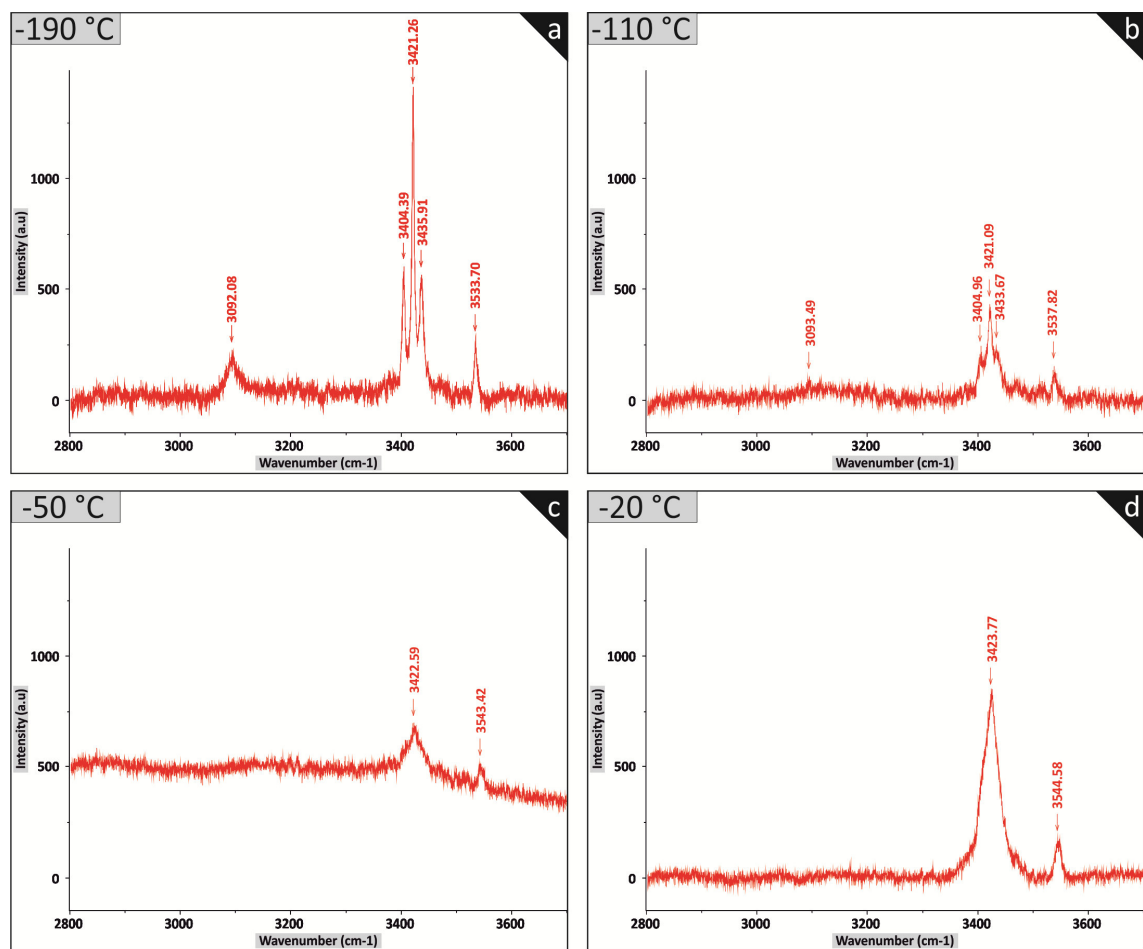


Figure 9 (a-d) Low-temperature Raman spectra of fluid inclusions from -190°C to -20°C . Spectra show ice peak at ca. 3093 cm^{-1} and dominant peaks of a mixture of hydrohalite and antarcticite at higher wavelength. Note that ice peak disappears at temperatures $> -110^{\circ}\text{C}$. Dominant peaks at temperatures $> -50^{\circ}\text{C}$ are attributed to hydrohalite.

Summary and Interpretation

The PQU was affected by uniaxial stretching during the earliest observable deformation stage (F1-constriction folds) at HP conditions, documented by the growth of syndeformative minerals like glaucophane (Gln) and Cld1. In blueschist-facies micaschists Cld1 porphyroblasts with an internal foliation S1 belong to D1 and appear as texturally equal to syndeformative D1 porphyroblasts described by Xypolias et al. (2007). D2 is contemporaneous to retrogression of Cld1 into phengite and chlorite and to the formation of Cld2. The latter is always aligned within the S2 foliation and S2 pressure shadows. In blueschists, Cld1 and Gln appear as syngenetic and were rotated parallel to the S2 foliation.

Assuming peak pressure conditions of about 13-17 kbar after Xypolias et al. (2007) in combination with a representative P-T path after Jolivet et al. (2010) for the southern Peloponnese (Fig. 10), the PQU which was subducted to depths of about 40 to 50 km accompanied with D1 uniaxial stretching (Fig. 11). The occurrence of Qtz1 as foliation-parallel shearband boudin after (Passchier and Trouw, 2005), deformed due to GBM at ca. 450-500°C, suggests formation of Qtz1 structures near peak metamorphic conditions that have been affected by subsequent deformation stage D2. Estimated isochores from fluid inclusions from Qtz1 do not indicate peak metamorphic conditions as well as fluid inclusions from Qtz2. By crossing temperature isotherms with calculated isochores from Qtz1, maximum pressure conditions between 6 and 7 kbar can be estimated (Fig. 10). Density loss is supported by decrepitation textures in Qtz1 which indicate non-isochoric exhumation after fluid entrapment (Fig. 10). Higher densities were calculated for fluid inclusions in discordant Qtz2 that support density loss of fluid inclusions in Qtz1 due to recrystallization and subsequent density re-equilibration of earlier large fluid inclusions. Formation conditions of Qtz1 can therefore be more likely linked with early exhumation stages during the proposed P-T evolution after Jolivet et al. (2010) which would indicate pressures between 13 and 16 kbar. This would suggest density loss of up to 10 kbar as result of ITD in Qtz1. Concerning the fact that Qtz2 is clearly discordant to the surrounding blueschist-facies micaschists, which also experienced D1-D3, the assumed conditions near 6 kbar and <400°C constrain minimum pressures and temperatures for D1-D3 within the PQU and represent formation conditions for Qtz2 boudin neck structures.

Regarding to our model in Figure 11, the structural evolution at the pressure peak and along the exhumation path shows a constrictional strain geometry. This continues into

SSW to SW-directed shear during D2. Subsequent late-stage open folding (D3) resulted into large-scale F2/F3 fold interference. Minimum P-T conditions for D1-D3 are constrained by the formation of D4 related boudin necks, which indicate subsequent extension in the region at Mani peninsula.

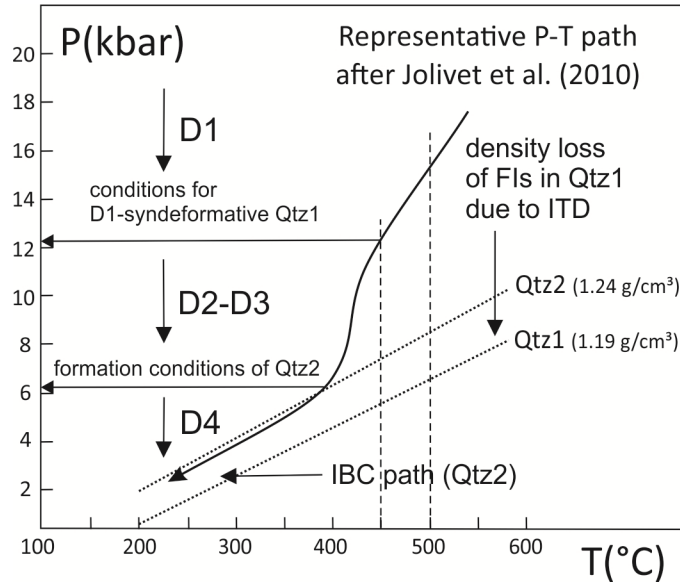


Figure 10 Representative P-T path for blueschists of the southern Peloponnese crossed with calculated isochores from fluid inclusions in Qtz1 and Qtz2. Conditions for Qtz2 constrain deformation stages D1-D3 above 6 kbar and < 400°C. Lower P-T-conditions from fluid inclusions of Qtz1 are interpreted as density-loss due to fluid inclusion re-equilibration.

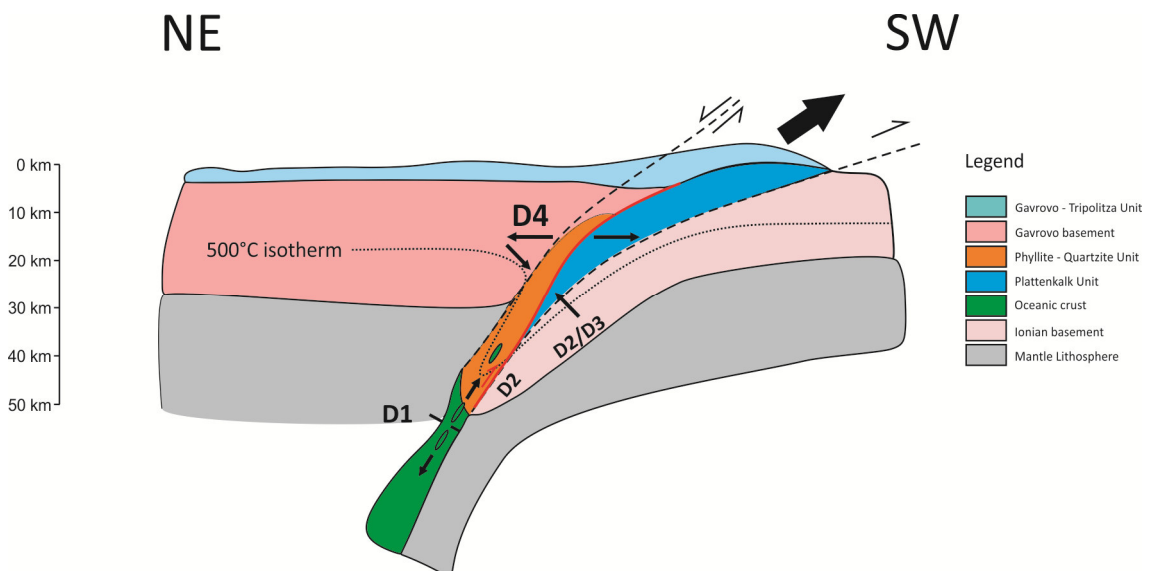


Figure 11 Tectonic model for the evolution of the PQU in the study area at Mani. Sketch is modified after Kurz (2005) and Jolivet et al. (2010).

References

- Baumgartner, M., and Bakker, R. J. (2010). Raman spectra of ice and salt hydrates in synthetic fluid inclusions. *Chemical Geology*, pp. 58-66.
- Bizon, G., Bonneau, M., Leboulenger, P., Matesco, S., and Thiebault, F. (1976). Sur la signification et l'extension des "massifs cristallins externes" en Péloponnèse méridional et dans l'Arc égéen. *Bulletin de la Société géologique de France*(18), pp. 337-345.
- Blumör, T., Dollinger, J., Knobel, M., Mutter, A., Zarda, S., and Kowalczyk, G. (1994). Plattenkalk series and Kastania Phyllites of the Taygetos Mts, new results on structure and succession. *Bull. Geol. Soc.*, pp. 83-92.
- Bodnar, R. J. (2003). Chapter 4. Introduction to aqueous –electrolyte fluid inclusions. In fluid inclusions: Analysis and Interpretation. *Mineralogical Association of Canada, Short Course 32*, pp. 81-99.
- Bonneau, M. (1973). Sur les affinités ioniennes des «calcaires en plaquettes» épimétamorphiques de la Crète, le charriage de la série de Gavrovo-Tripolitsa et la structure de l'arc égéen. *Comptes Rendus de l'Académie des Sciences*(277), pp. 2453-2456.
- Chatzaras, V., Xypolias, P., and Doutsos, T. (2006). Exhumation of high-pressure rocks under continuous compression: a working hypothesis for the southern Hellenides (central Crete, Greece). *Geol. Mag.* (143), pp. 859-876.
- Diamond, L. W. (2003). Glossary: Terms and symbols used in fluid inclusion studies. *Mineralogical Association of Canada*, p. 365-374.
- Doutsos, T., Koukouvelas, I., Poulimenos, G., Kokkalas, S., Xypolias, P., and Skourlis, K. (2000). An exhumation model of the south Peloponnesus, Greece. *International Journal of Earth Sciences*(89), pp. 350-365.
- Jacobshagen, V. (1986). Geologie von Griechenland. *Beiträge zur regionalen Geologie der Erde*.
- Jolivet, L., and Faccenna, C. (2000). Mediterranean extension and the Africa-Eurasia collision. *Tectonics*(19), pp. 1095-1106.
- Jolivet, L., Faccenna, C., Goffé, B., Burov, E., and Agard, P. (2003). Subduction tectonics and exhumation of high-pressure metamorphic rocks in the mediterranean orogens. *American Journal of Science*(303), pp. 353-409.
- Jolivet, L., Trotet, F., Monié, P., Vidal, O., Goffé, B., Labrousse, L., et al. (2010). Along-strike variations of P–T conditions in accretionary wedges and syn-orogenic. *Tectonophysics*, pp. 133-148.
- Katagas, C. (1980). Ferroglaucophane and chloritoid-bearing metapelites from the phyllite series, southern Peloponnese, Greece. *Mineralogical Magazine*(43), pp. 975-978.
- Krahl, J., Richter, D., Forster, O., Kozur, H., and Hall, R. (1988). Zur Stellung der Talea Ori Deckenstapels (Griecheland). *Zeitschrift der deutschen geologischen Gesellschaft*(139), pp. 191-227.
- Krenn, K. (2010). Fluid inclusions in quartz related to subsequent stages of foliation development during a single metamorphic cycle (Schneeberg Fault Zone, Eastern Alps, Austria). *Lithos*(118), pp. 255-268.
- Krenn, K., Bauer, C., Proyer, A., Mposkos, E., and Hoinkes, G. (2008). Fluid entrapment and reequilibration during subduction and exhumation: A case study from the high-grade Nestos shear zone, Central Rhodope, Greece. *Lithos*(104), pp. 33-53.
- Kurz, W. (2005). Constriction during exhumation: Evidence from eclogite microstructures. *Geology*(33), pp. 37-40.
- Leake, B., Woolley, A., Arps, C., Gilbert, M., Grice, J., Hawthorne, F., et al. (1997). Nomenclature of Amphiboles: Report of the subcommittee on amphiboles of the international mineralogical association, commission on new minerals and mineral names. *The Canadian Mineralogist*(35), pp. 219-246.
- Lister, G. (1977). Discussion: crossed-girdle c-axis fabrics in quartzites deformed by plane strain and progressive simple shear. *Tectonophysics*, pp. 51-54.
- Mogessie, A., Ettinger, K., and Leake, B. (2004). Nomenclature of amphiboles: Additions and revisions to the International Mineralogical Association's amphibole nomenclature. *Mineralogical Magazine*(68), pp. 209-215.
- Passchier, C., and Trouw, R. (2005). *Microtectonics*. Berlin Heidelberg: Springer-Verlag.
- Ramsay, J. (1967). Folding and fracturing of rocks. *Mc Graw-Hill*.
- Ring, U., Brachert, T., and Fassoulas, C. (2001). Middle Miocene graben development in Crete and its possible relation to large-scale detachment faults in the southern Aegean. *Terra Nova* 13, pp. 297-304.
- Ring, U., Layer, P. W., and Reischmann, T. (2001). Miocene high-pressure metamorphism in the Cyclades and Crete, Aegean Sea, Greece: Evidence for large-magnitude displacement on the Cretan detachment. *Geology* 29, pp. 395-398.
- Ring, U., Will, T., Glodny, J., Kumerics, C., Gessner, K., Thomson, S., Güngör, T., Monié, P., Okrusch,

- M., and Drüppel, K. (2007). Early exhumation of high-pressure rocks in extrusion wedges: Cycladic blueschists in the eastern Aegean, Greece, and Turkey. *Tectonics*(26), TC2001, doi:10.1029/2005TC001872.
- Robertson, A. (2006). Sedimentary evidence from the south Mediterranean region (Sicily, Crete, Peloponnese, Evia) used to test alternative models for the regional tectonic setting of Tethys during Late Palaeozoic-Early Mesozoic time. *Robertson, A.H.F., Mountrakis, D. (Eds.), Tectonic Development of the Eastern Mediterranean region. Geological Society, London, Special Publications*(260), pp. 91-154.
- Samson, I. M., and Walker, R. T. (2000). Cryogenic Raman spectroscopic studies in the system NaCl–CaCl₂–H₂O and implications for low temperature phase behaviour in aqueous fluid inclusions. *The Canadian Mineralogist*(35), pp. 35-43.
- Schmid, S., Bernoulli, D., Fügenschuh, B., Matenco, L., Schefer, S., Schuster, R., et al. (2008). The Alpine-Carpathian-Dinaridic orogenic system: correlation and evolution of tectonic units. *Swiss Journal of Geoscience*(101), pp. 139-183.
- Shepherd, T. J., Rankin, A. H., and Alderton, D. H. (1985). *A Practical Guide to Fluid Inclusion*. Blackie, London. p. 239 pp.
- Smith, A., Woodcock, N., and Naylor, M. (1979). The structural evolution of a continental margin, Othris Mountains, Greece. *J. geol. Soc.*(136), pp. 589-603.
- Steele-MacInnis, M., Bodnar, R. J., and Naden, J. (2011). Numerical model to determine the composition of H₂O–NaCl–CaCl₂ fluid inclusions based on microthermometric and microanalytical data. *Geochimica et Cosmochimica Acta*, pp. 21-40.
- Trotet, F., Goffé, B., Vidal, O., and Jolivet, L. (2006). Evidence of retrograde Mg-carpholite in the Phyllite - Quartzite nappe of Peloponnese from thermobarometric modelisation - geodynamic implications. *Geodinamica Acta*(19), pp. 323-343.
- Vityk, M. O., Bodnar R. J. (1995). Textural evolution of synthetic fluid inclusions in quartz during reequilibration, with applications to tectonic reconstruction. *Contrib. Mineral. Petrol.*(121), pp. 309-323
- Xypolias, P., Chatzaras, V., and Koukouvelas, I. (2007). Strain gradients in zones of ductile thrusting: Insights from the External Hellenides. *Journal of Structural Geology*(29), pp. 1522-1537.

Figure Index

- Figure 1 Geological overview of the Hellenides modified after Jacobshagen et al. (1986). Red rectangle in the southernmost area of the Peloponnese indicates study area at the Mani peninsula..... 3
- Figure 2 Tectonostratigraphy of the main tectonic units of the external Hellenides after Chatzaras et al. (2006). Circle shows tectonostratigraphic level of the study area. 4
- Figure 3 (a) F1 constriction folds in blueschist-facies micaschists. (b) Boudin within blueschist consisting of uniaxial stretched glaucophane-, zoisite- and chloritoid-bearing layers. (c) Asymmetric F2 shear folds indicating SW/SSW- shear direction (D2). (d) Open-spaced F3 folds with subhorizontal W-E trending fold axes (D3). 7
- Figure 4 Mapped area of the Mani peninsula. A large-scale fold interference pattern results from superposition of F2 and F3. 8
- Figure 5 (a) Glaucophane (Gln) with shape preferred orientation parallel to S2. (b) Chloritoid 1 (Cl1), slightly rotated into S2 orientation. (c) Blueschist-facies micaschists with relics of D1-synformative chloritoid porphyroblasts (Cl1) overprinted by SSW directed shearing (D2). (d) Chloritoid 2 (Cl2) along S2 foliation and within D2 pressure shadows. (e) Quartzites point to GBM recrystallization..... 10
- Figure 6 (a) Amphibole classification after Leake et al. (1997) and Mogessie et al. (2004). Chemistry of studied amphiboles plots in the glaucophane field. (b) Mineral chemistry of sodic amphiboles in a $100*Fe^{2+}/(Fe^{2+} + Mg + Mn)$ vs. $100*Fe^{3+}/(Fe^{3+} + [Al]^6 + Ti)$ diagram. Chemical compositions indicate glaucophane. 11
- Figure 7 LPO plots combined with microstructures from the blueschist-facies micaschists (a/b) and metaconglomerates (c). (a) & (b) Fine grained quartz (< 0.7 mm) showing grain boundary migration (GBM) recrystallization. Quartz c-axes distributions indicate uniaxial stretching (D1). (c) Quartz (< 0.6 mm) shows undulatory extinction as well as bulging recrystallization and core-mantle textures. Quartz-c-axes distribution displays a cross-girdle pattern of type 1 after Lister (1977). Asymmetry points to SW-directed shearing (D2). 12
- Figure 8 (a) Concordant quartz boudin (Qtz1). (b) Boudin neck filled with Qtz2. (c) Recrystallized fine-grained quartz matrix (Qtz1) including large mm-scale dolomite crystals (yellow arrows). (d) Polyphase (L,V,S) fluid inclusions arranged along intragranular fluid inclusion planes (Qtz1). (e) Polyphase (L,V,S) single fluid inclusions in Qtz2. (f) Hook-like morphology and planes of small inclusions (see arrows) indicative for ITD after Vityk and Bodnar (1995). (g) Irregular dendritic inclusion texture in Qtz2

indicating IBC after Vityk and Bodnar (1995). (h) Calculated isochores from fluid inclusions (densities between 1.19 and 1.13 g/cm ³ for Qtz1 and 1.24 to 1.19 g/cm ³ for Qtz2).	14
Figure 9 (a-d) Low-temperature Raman spectra of fluid inclusions from -190°C to -20°C. Spectra show ice peak at ca. 3093 cm ⁻¹ and dominant peaks of a mixture of hydrohalite and antarctite at higher wavelength. Note that ice peak disappears at temperatures > -110°C. Dominant peaks at temperatures > -50°C are attributed to hydrohalite.	15
Figure 10 Representative P-T path for blueschists of the southern Peloponnese crossed with calculated isochores from fluid inclusions in Qtz1 and Qtz2. Conditions for Qtz2 constrain deformation stages D1-D3 above 6 kbar and < 400°C. Lower P-T-conditions from fluid inclusions of Qtz1 are interpreted as density-loss due to fluid inclusion re-equilibration.	17
Figure 11 Tectonic model for the evolution of the PQU in the study area at Mani. Sketch is modified after Kurz (2005) and Jolivet et al. (2010).	17

Appendix

Appendix 1 Data from microthermometric analyses.

Qtz		n	Textural appearance	Size (mm)	n*/phases	T_e (°C)	T_m (Ice) (°C)	T_m (Hydrohalite) (°C)	T_h (partial) (°C)	T_m (Halite) (°C)	Total salinity	Density (g/cm ²)	Chemistry
1	concordant	15	intragranular FIP	< 0.8	3/L-V-S	< -52	- 50 to - 47	- 37 to - 34	182 to 248	290 to 390	37.4 to 46.4	1.13 to 1.19	H ₂ O - NaCl - CaCl ₂
2	discordant	20		intragr. FIP cluster, single	> 3	3/L-V-S	< -52	- 51 to - 49	-35	120 to 182	270 to 387	36 to 46.4	

n...number of measurements;
n*...number of phases

Second part

Petrographic and structural analysis of the Ötztal Complex and surrounding tectonic units at Obergurgl and Vent

Supervisors: Priv.-Doz. Mag. Dr.rer.nat. Kurt Krenn

Ao.Univ.-Prof. Dr.phil. Harald Fritz

Table of contents

1. Introduction.....	2
2. Geological overview	3
2.1 The Alpine orogen	3
2.2 Paleogeography of the Eastern Alps	6
2.3 Geological setting of the study area.....	7
2.3.1 The Ötztal Complex (ÖC).....	7
2.3.2 The Schneeberg Complex (SC).....	8
2.3.3 The Texel Complex (TC).....	8
2.3.4 Structural characteristics of the ÖC, SC and TC.....	9
3. Methods and results.....	9
3.1 Sampled profile and petrographic field description	9
3.2 Deformation stages and profile description	12
3.2.1 Deformation stages.....	13
3.2.2 Part A: Bärenhoppet area to Obergurgl village.....	15
3.2.3 Part B: Ramolhut to Ramoljoch	17
3.2.4 Part C: Ramoljoch to Vent village	18
3.3 Petrography and microstructural analysis	20
3.3.1 Garnet-bearing paragneiss.....	20
3.3.2 Micaschists.....	23
3.3.3 Amphibolites.....	25
3.3.4 Mineral chemical analysis of amphibolites	27
3.3.5 Orthogneiss	30
4. Discussion	31
4.1 The low-angle normal fault near Ramolhut and the discrete shear zone at profile C (study area A in Fig. 25)	31
4.2 Structures of the Ötztal Complex (ÖC) compared with structures of the Texel Complex (TC).....	31
References.....	33
Figure Index	34
Appendix.....	35

1. Introduction

The Ötztal-Bundschuh Complex of the Eastern Alps is a structurally complicated polymetamorphic unit, which rises into several ideas regarding its evolution. Folding events with steep and shallow dipping fold axes led to the former term “Schlingentektonik” (after Schmidegg, 1964). In the Ötztal Complex west of the Tauern Window that can be further subdivided into the Venter-, Stubai-, Mittelberg- and Marzell Schlinge (Mauracher, 1980). The complex structural evolution of this area adjacent to the southern Schneeberg and Texel Complexes is the object of many structural investigations. The latest observations are given in Sölva et al. (2001; 2005), Krenn (2010) and Krenn et al. (2011), focusing on the structural evolution of the Texel Complex and the Schneeberg Complex. The present study includes structural (macro- and microstructures) investigations along three profiles from the SE to the NW in the Ötztal Complex.

According to Schmid et al. (2004) the tectonic situation west of the Tauern Window is made up by an upper and a lower plate, with the eo-Alpine high pressure wedge in between. The upper and lower plates are considered as Ötztal-Bundschuh nappe system and Silvretta-Seckau nappe system, respectively. The eo-Alpine high pressure wedge is referred to as Koralpe-Wölz nappe system. Regarding to this a tectonic boundary should be preserved between upper plate and the high pressure wedge. However, it is documented by several authors that this tectonic boundary between the upper plate and the tectonic wedge appears continuous. This fact and the continuous increase of the grade of eo-Alpine metamorphism from NW to the SE rises to the conclusion that the southern Ötztal Complex may partly be incorporated into subduction and hence was not in upper plate position during eo-Alpine subduction.

To support this idea results have been compared with the Texel Complex that shows structural and petrographic similarities to the Ötztal Complex and is regarded to the eo-Alpine wedge.

2. Geological overview

2.1 The Alpine orogen

The Alpine orogen formed due to the still ongoing convergence between the European and African Plates and the associated closures of corresponding ocean basins (e.g. Schmid et al. 2004). Today the Alps extend along an arc-shaped area reaching from Vienna (Austria) in the E to Monaco (France) in the SW and are subdivided into Western, Central, Southern and Eastern Alps. Their W-E striking portion can be viewed as the Eastern Alps, the realm south of the Periadriatic Lineament is considered as the Southern Alps and the almost NE-SW to N-S striking portions in the west can be attributed to the Central and Western Alps. During Cretaceous and Tertiary times, two main metamorphic events dominate in the Alpine orogen, that led to significant metamorphic and structural imprints in the Austroalpine Units (Eastern Alps) and in the Western Alps, respectively (cf. Oberhänsli, 2004). The Cretaceous event is associated with an intracontinental subduction between the North Apulian and South Apulian Plates. This resulted into the eo-Alpine high pressure belt (Thöni, 1981) within the Austroalpine nappe system (Fig. 1).

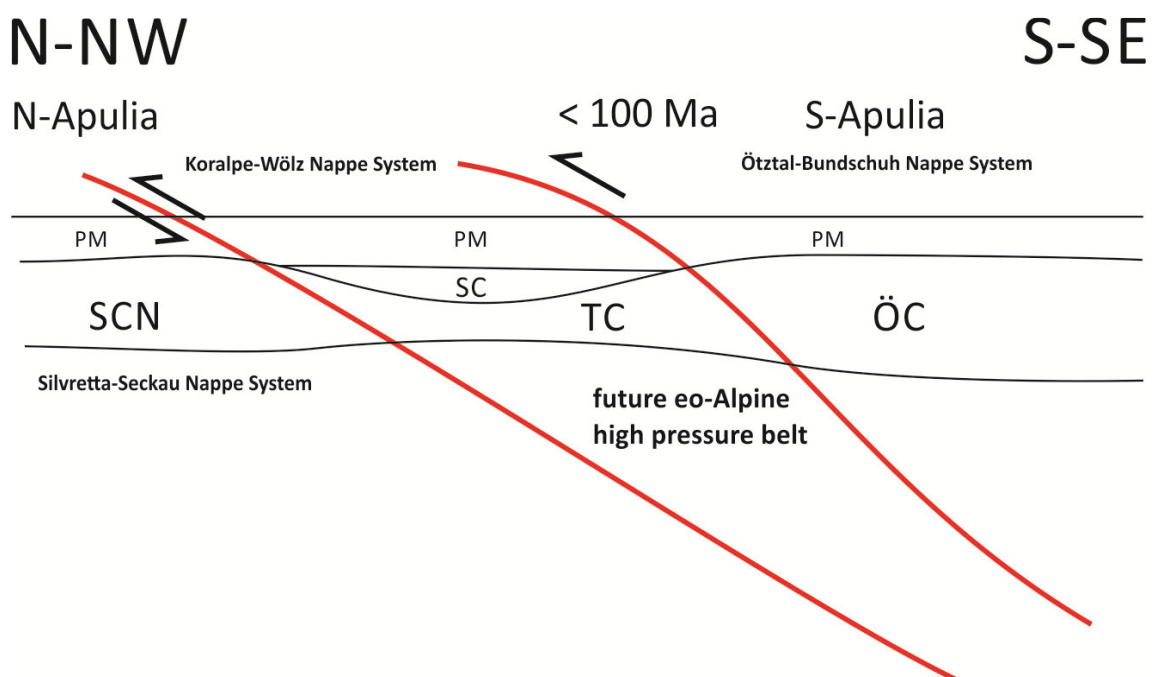


Figure 1 Sketch of the intracontinental subduction during Cretaceous times (modified after Krenn et al., 2011). PM Permomesozoic Cover; SCN Silvretta-Campo Nappe; SC Schneeberg Complex; TC Texel Complex; ÖC Ötztal Complex

The Tertiary event describes the subduction of the Penninic Oceans and the subsequent collision of the European and Apulian Plates (e.g. Schmid et al. 2004). Evidence for this Tertiary metamorphism is situated in tectonic windows, i.e. the Tauern Window, Engadiner Window and the Rechnitz Window within the Eastern Alps (Fig. 2).

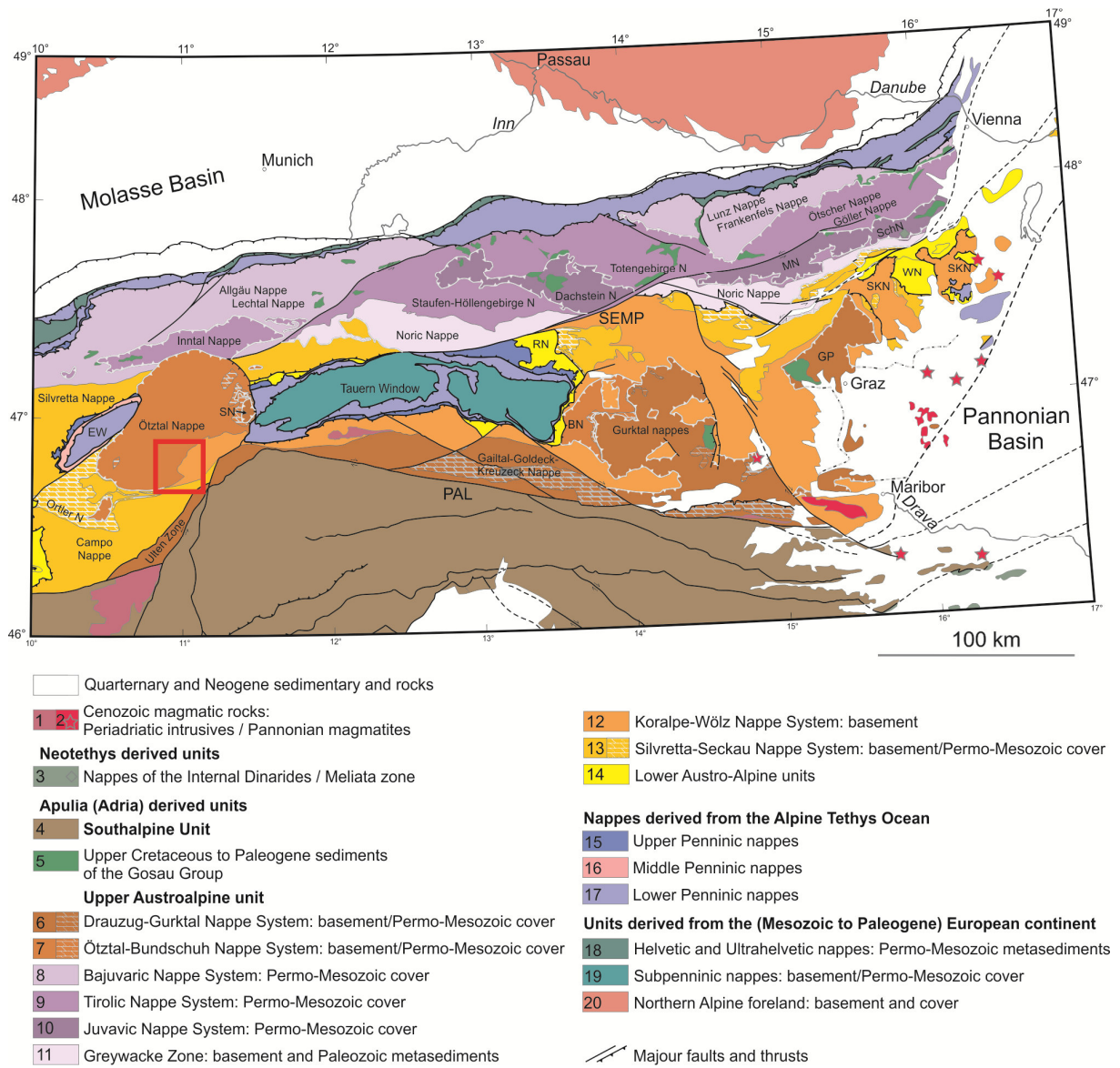


Figure 2 Tectonic nappe subdivision of the Eastern Alps after Schmid et al. (2004). Red rectangle shows study area. PAL Periadriatic Lineament; EW Engadiner Window; SEMP Salzach-Ennstal-Mariazell-Puchberg Fault

The Austroalpine nappes contain the Upper Austroalpine nappes and the Lower Austroalpine nappes, which occur as a complex basement and cover nappe stack of crustal material overlain by Permo-Mesozoic metasediments (Fig. 3). Tectonostratigraphically the uppermost part of the Upper Austroalpine nappes is

represented by the Drauzug-Gurktal nappe system, as highest tectonic unit, underlain by the Ötztal-Bundschuh nappe system. The Ötztal-Bundschuh nappe system shows dominant Variscan but also weak eo-Alpine metamorphic imprints. The Koralpe-Wölz high-pressure nappe system, characterized as an eo-Alpine extruding wedge, comprises a polymetamorphic basement and a Paleozoic and Permo-Mesozoic cover. It is overlain by the Ötztal-Bundschuh nappe system as the upper tectonic plate after Schuster et al. (2004). The basement consists of Variscan, Permian and eo-Alpine metamorphic imprints, whereas the Paleozoic cover, represented by the Schneeberg Complex and Radenthein Complex, shows only an eo-Alpine metamorphic imprint. The lowermost unit within the Upper Austroalpine nappes is considered as the Silvretta-Seckau nappe system and is represented by a pre-Alpine basement and a Permo-Mesozoic cover with a dominant Variscan metamorphic imprint.

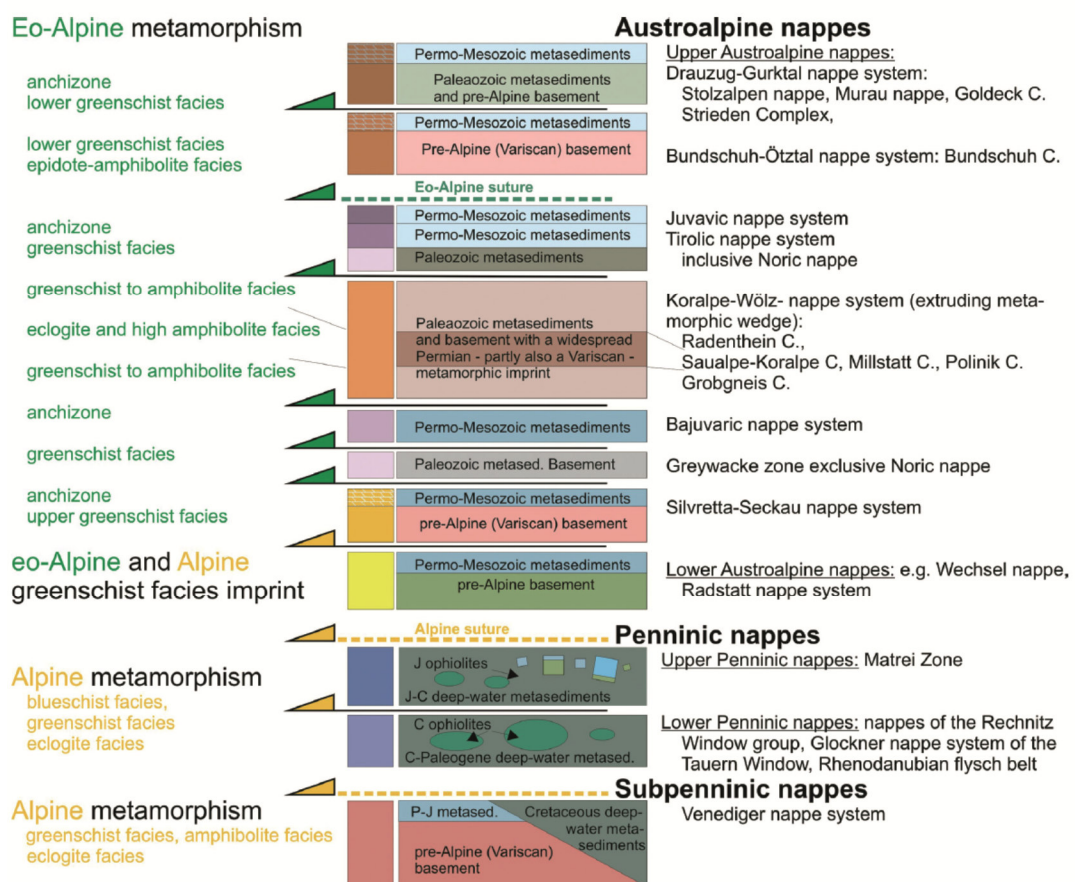


Figure 3 Tectonostratigraphy after Schuster et al. (2004).

2.2 Paleogeography of the Eastern Alps

During Triassic times carbonates at the western margin of the Meliata-Hallstatt Ocean, which are today preserved as parts of the Northern Calcareous Alps, have been deposited at the eastern realm of the future Apulian Plate (Schmid et al., 2004) (Fig. 4a). Due to rifting and opening of the Atlantic Ocean and the eastern prolongation in the northeast (the Alpine Tethys), the Piedmont-Liguria and Valais Oceans, led to the separation of the Apulian Plate from the European Plate since Late Jurassic times (Fig. 4b). Rifting led to the subduction of the Meliata-Hallstatt Ocean and the subsequent WNW-directed obduction of the future Northern Calcareous Alps on the N-Apulian Plate. The late Cretaceous formation of the Koralpe-Wölz high pressure nappe system (eo-Alpine high-pressure belt) containing eo-Alpine eclogites was the result of a S-SE directed intracontinental subduction within the Apulian Plate (Fig. 4c).

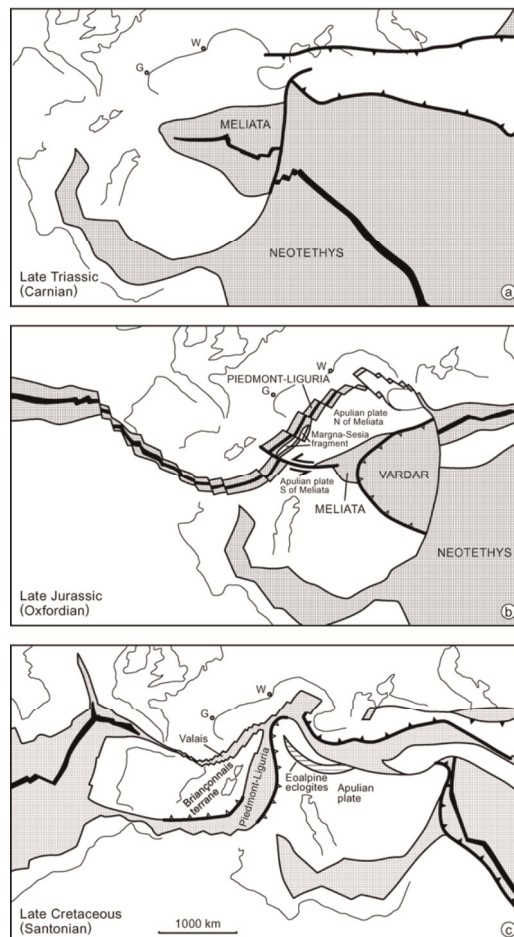


Figure 4 (a-c) Sketches of the paleogeographic evolution from (a) Late Triassic to (c) Late Cretaceous times. G: Genf; W: Wien. (Schmid et al., 2004).

2.3 Geological setting of the study area

The investigated area west of the Tauern Window consists of three units attributed to the Upper Austroalpine basement nappes (after Schmid et al., 2004). These are the Ötztal Complex which is part of the Ötztal-Bundschuh nappe system, the Schneeberg Complex and Texel Complex; both the Schneeberg Complex and Texel Complex are assigned to the Koralpe-Wölz high pressure nappe system (Fig. 5a).

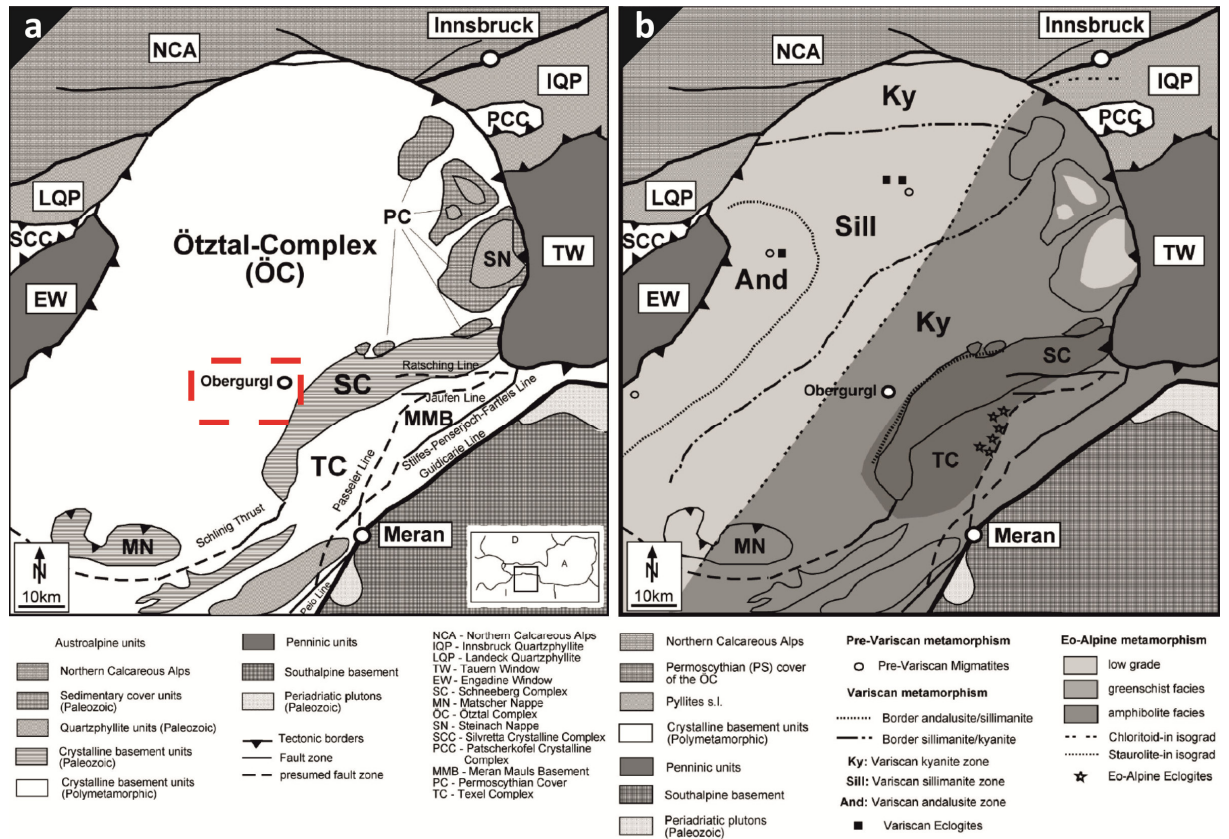


Figure 5 (a/b) Austroalpine units at and around the study area after Tropper and Recheis (2003). Red rectangle points to study area. (b) Influence of Caledonian, Variscan and eo-Alpine metamorphism.

Tectonostratigraphically, the Ötztal Complex is in hanging wall position to the Schneeberg Complex, which is underlain by the Texel Complex. In the following it is focused on these three complexes.

2.3.1 The Ötztal Complex (ÖC)

The Ötztal Complex is characterized by a polymetamorphic history that suffered at least three metamorphic events: Caledonian, Variscan and eo-Alpine (Fig. 5b). It consists of metasediments, orthogneisses and amphibolites as the main rock types. Locally preserved migmatites, e.g. Reschenpass or Winnebach (e.g. Schweigl, 1995; Hoinkes, 1973), represent relics of the Caledonian metamorphism. The Variscan event is the

dominant imprint within the ÖC and is characterized by amphibolite facies conditions ranging from 500-650°C and 4-8 kbar (e.g. Hoinkes and Thöni, 1993). However, the occurrence of Variscan eclogites in the central ÖC indicates eclogite - facies metamorphism with temperatures and pressures of ~730°C and ~27 kbar, respectively (Miller and Thöni, 1995). The eo-Alpine imprint increases from NW to SE and is characterized by a chloritoid-in isograd (Purtscheller, 1969; Thöni, 1981) (Fig. 5b). This rise of eo-Alpine metamorphism to the southeastern area of the chloritoid-in isograd is proven by an eo-Alpine staurolite-in isograd within the Texel Complex, indicating metamorphic conditions of ca. 10 kbar and 600°C (Hoinkes, 1981). Compiled mineral age data (K/Ar- and Rb/Sr-ages of white mica and biotite) by Thöni and Hoinkes (1987) indicate Variscan ages in the NW and eo-Alpine ages in the SE of the ÖC.

2.3.2 The Schneeberg Complex (SC)

Southeast of the ÖC the Schneeberg Complex consisting of metapelites, metacarbonates and metamarl occurs, arranged in synform structures that form the ‘Schneeberg Hauptmulde’, Seeberspitz-, Lodner- and Schrottner- synforms (Mauracher, 1980). Compared to the surrounding ÖC and Texel Complex, the SC shows no evidence for a polymetamorphic history (Fig. 5b). Thus it is interpreted as a Paleozoic sedimentary cover of a Variscan basement (i.e. Texel Complex) (Krenn et al. 2011). The eo-Alpine imprint within the SC reached conditions of 550-600°C and 8-10 kbar (e.g. Hoinkes, 1981, Tropper und Recheis, 2003, Krenn, 2010). Rb/Sr-ages of muscovite (70-100 Ma) support an eo-Alpine metamorphic history (see Thöni and Hoinkes, 1987).

2.3.3 The Texel Complex (TC)

The Texel Complex, geographically situated south of the SC, shows a polymetamorphic evolution, similar to the ÖC. According to Schuster and Stüwe (2008) the TC contains an additional Permian metamorphic imprint up to amphibolite and granulite facies. Nevertheless the eo-Alpine imprint in the TC is clearly dominant, that led to the tectonic position of the TC within the eo-Alpine high pressure wedge with the occurrence of eo-Alpine eclogites (Habler et al., 2006, Hoinkes et al., 1991) (Fig. 5b). Relics of those eo-Alpine high pressure assemblages indicate minimum pressures of 11.5 kbar (Hoinkes et al., 1999).

2.3.4 Structural characteristics of the ÖC, SC and TC

The northern and central parts of the ÖC are dominated by a W-E striking penetrative Variscan field foliation (Purtscheller, 1978). In the southern ÖC however the “Schlingentektonik” (Schmidegg, 1964) dominates, being interpreted as the eo-Alpine overprint of the Variscan structures (e.g. Krenn et al., 2011).

According to Krenn et al. (2011) the SC shows four deformation stages related to the eo-Alpine event. D1 to D3 are characterized by subsequent folding events F1, F2 and F3, where F2 and F3 are responsible for the fold interference that forms the large-scale synform structures in the SC. In the southern area beside the Laas synform structure, a D4-related crenulation cleavage and S-C fabrics formed due to NW-SE shortening, probably released by early shearing along the Pässeier-Jaufen-Fault.

The TC shows no relics of Variscan structures due to the intense amphibolite - to eclogite - facies eo-Alpine tectonometamorphic overprint. Sölva et al. (2001) defined four ductile deformation events during eo-Alpine metamorphism within the TC: D1 to D3 took place during ductile stages and D4 at brittle/ductile conditions. D1 is characterized by a shear event that formed a E-W trending stretching lineation, which was subsequently followed by D2 and D3 folding events. F2 and F3 are the result of E-W and N-S to NW-SE compression, respectively. D4 is documented by an open fold structure with NW-dipping fold axes.

3. Methods and results

3.1 Sampled profile and petrographic field description

Structural observations along three profiles (A, B and C) have been performed over a distance of about 20 km in the Ötztal Complex from Obergurgl to Vent village (Fig. 6). It starts at Bärenhoppet area east-southeast from the Hohe Mut towards west to the Ramoljoch area and ends at Vent village. The study includes oriented sampling of the lithologies and macro- to microstructural observations.

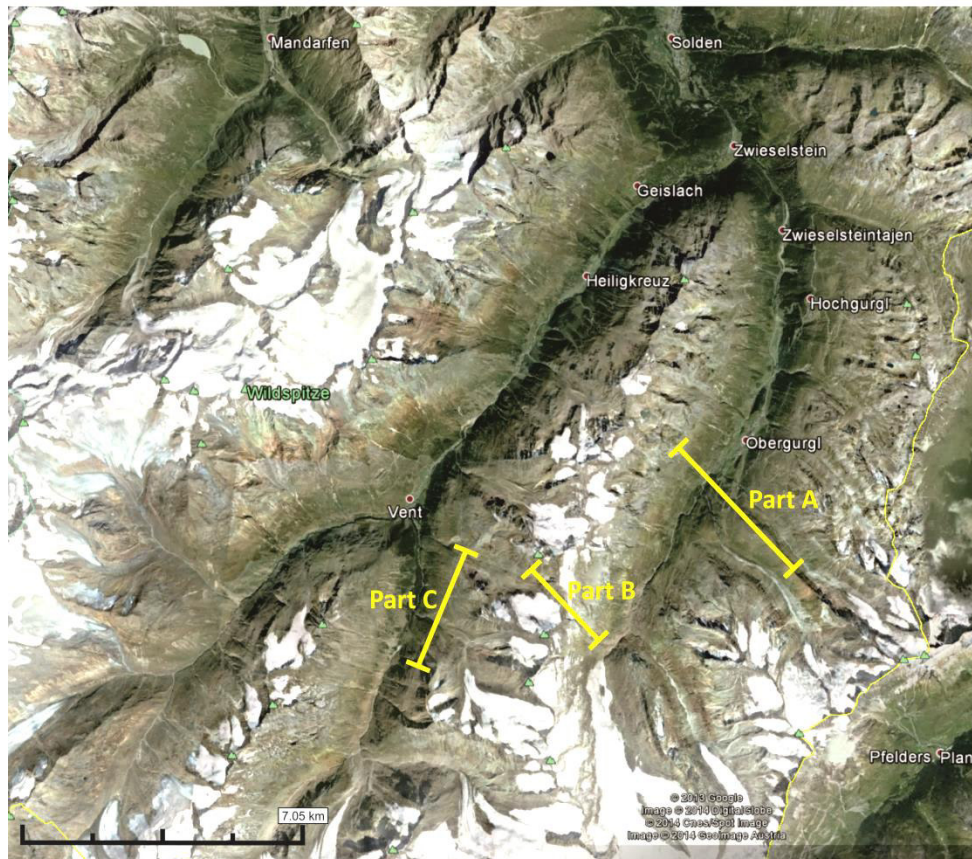
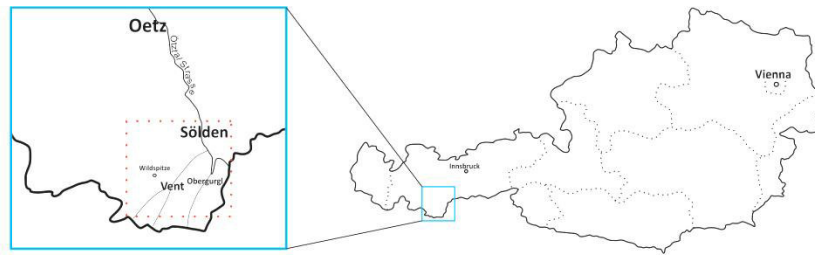


Figure 6 Geographical overview of the investigated area (from Google Earth, 2013). Yellow lines mark the sampled profiles.

A briefly overall description of the occurring lithologies on macro-scale includes:

- *Paragneiss*

Paragneisses are the most frequently sampled and outcropping rocks along the profile. In the investigated areas, however, paragneisses change their mineral content, fabric and grain size (fine grained means components < 1 mm). Easy to recognize and most common mineral assemblages in the paragneisses are garnet + feldspar + biotite + quartz \pm mica \pm chlorite. They are distinguished into 1) coarse-grained paragneisses \pm garnet, 2) quartzitic-/ feldspar-rich paragneisses \pm garnet and 3) fine-grained paragneisses \pm garnet.

- *Micaschist*

Micaschists are similar to the paragneisses by holding a continuous transition. The most reliable difference to the paragneisses here is the occurrence of white mica pseudomorphs after staurolite and locally the presence of kyanite. Mineral assemblage is garnet + quartz + mica + biotite \pm kyanite \pm white mica pseudomorphs after staurolite. Therefore micaschists have been distinguished into 1) garnet micaschists, 2) garnet \pm kyanite micaschists with white mica pseudomorphs after staurolite (Fig. 7) and 3) fine grained quartzitic garnet micaschists.



Figure 7 Garnet micaschist with white mica pseudomorphs after staurolite. Ramolhut.

- *Amphibolite*

Fine grained (< 1 mm) to coarse grained (> 1 mm) amphibolites occur as lenses and can be separated by layers of epidote and garnet. Epidote-rich amphibolites are limited to thin layers (dm-scale). Coarse grained amphibolites display late growth of hornblende (> 5 mm) found as garnet schists that are arranged as boudins within strongly folded paragneisses and micaschists (Fig. 8). Amphibolites have been distinguished into 1) garnet amphibolites; 2) epidote \pm garnet amphibolites and 3) garnet schists.



Figure 8 Garben schists arranged as boudins within folded paragneisses or micaschists. Diembach.

- *Orthogneiss*

Sampled orthogneisses (Fig. 9) show large feldspar clasts (up to 5 cm). They locally contain magmatic textures.



Figure 9 Orthogneisses with large feldspar clasts. Vent village.

3.2 Deformation stages and profile description

Observed field-structures plotted on the lower hemisphere of the Schmidt net and the trend of the profiles is given in Appendix 1.

The profile is subdivided into three parts A-C:

- A Bärenhoppet area to Obergurgl village (Appendix 2)
- B Ramolhut to Ramoljoch (Appendix 3)
- C Ramoljoch to Vent village (Appendix 4)

3.2.1 Deformation stages

Based on the macro- and microstructural observations, combined with petrographic and chemical analysis of the sampled profiles the following deformation stages have been distinguished (Fig. 10):

Used abbreviations are: D_n for deformation increments, S_n for foliation, F_n for fold and b_n for fold axes, where n is the number of deformation stages.

D0: D0 deformation is attributed to a pre-*eo*-Alpine event and only rarely preserved as foliation S₀ in staurolites. A spaced foliation (microlithons) in micaschists as well as pigmented cores of polymetamorphic garnets are additionally related to D0.

D1: D1 is related to the formation of the earliest metamorphic foliation S₁ as result of *eo*-Alpine subduction.

D2 + D3: D2 shearing resulted in the formation of SE-vergent shear folds F₂ with steep NW plunging fold axes, which are dominant along profile C and rarely preserved as small scale shear folds along part A (up to the Ramolhut) and B (up to the Ramoljoch). Subsequent D3 resulted in F₃ folds perpendicular to the D2 folds, forming a large-scale tight fold with fold axes rotating from NNE to N and N to NW in profile parts A/B and part C, respectively. Parasitic folds related to F₃ are also described along profile parts A to C and occur in different sizes. D3 folding event resulted into inverted F₂ shear folds within the footwall and hanging wall fold limbs of F₃. Locally F₂ and F₃ result in a fold interference pattern O₂ after Grasemann et al. (2004). The dominant field foliation S₃, considered as axial plane foliation of F₃ folds, developed during late D3. This S₃ field foliation is more pronounced in micaschists than in surrounding paragneisses. In sections parallel to b₃ fold axes SC-fabrics and ecc-structures occur, suggesting N-directed shearing during D3. Additionally, lithologies containing white mica pseudomorphs after staurolite repeat along the profiles A and B as result of D3 related large-scale folding.

D4: D4 is interpreted as an ESE-directed normal faulting event cutting earlier fold structures by low-angle.

D5: D5 is documented by a distinct sinistral shear zone only found in profile C.

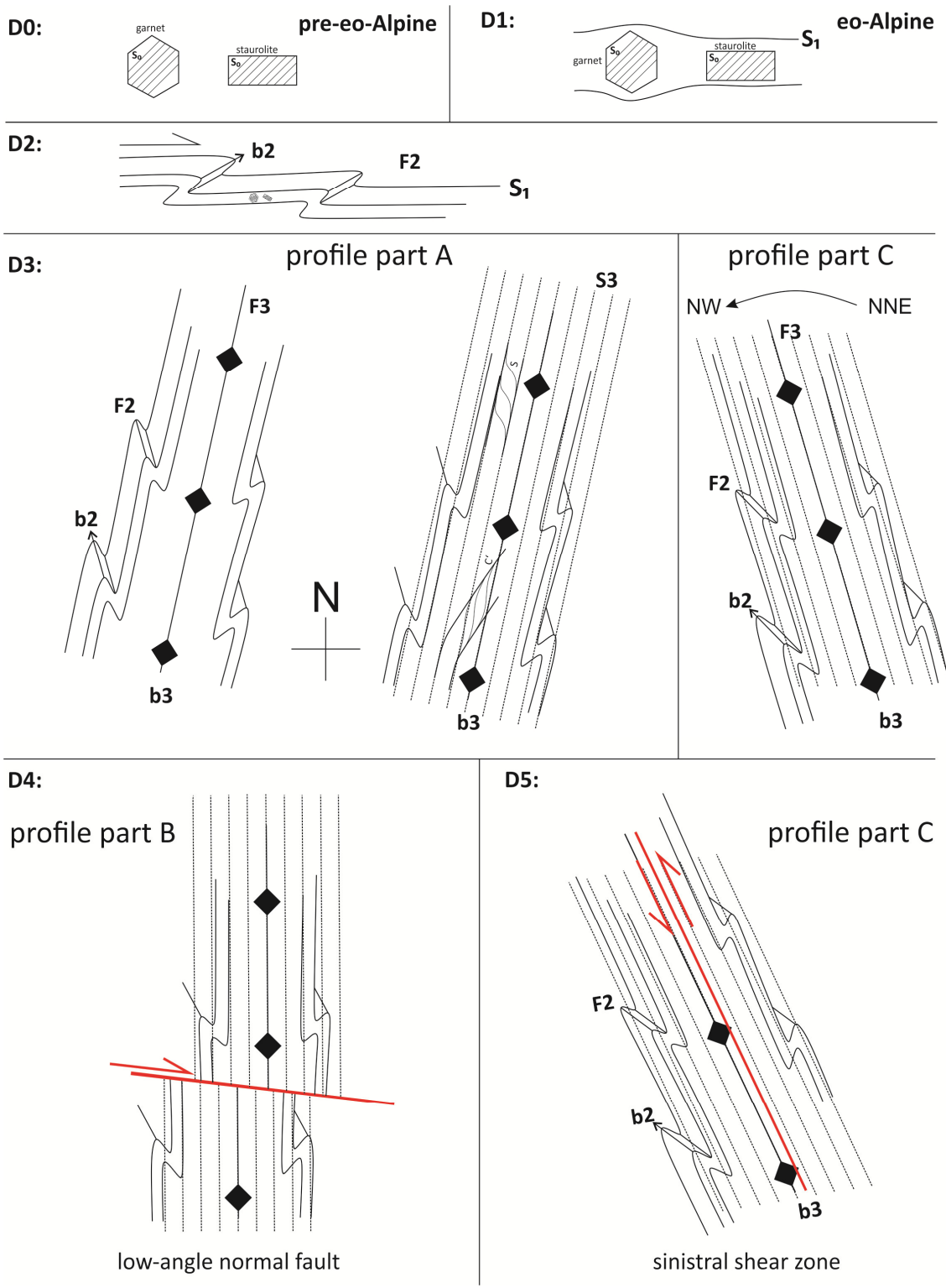


Figure 10 Sketch of deformation stages D0 to D5.

3.2.2 Part A: Bärenhoppet area to Obergurgl village

Length: ca. 5 km; Orientation: NW-SE

Amphibolites with intercalated epidote-garnet bearing layers dominate the area at Bärenhoppet. Towards NW lithologies vary between alternating paragneisses and micaschists. Micaschists are characterized by white mica pseudomorphs after staurolite. Dominant structures are related to D3 and D2. A large-scale tight fold structure, defined as F3 fold structure, with fold axes b3, plunging shallowly to NNE, occurs (Figs. 11a/b). Isoclinal parasitic folds of second order (Figs. 11c/d) occur frequently. The main field foliation is considered as S3 axial plane foliation of the F3 fold structure which strikes NE-SW and dips moderately (ca. 40° dip angle) to the NW. Furthermore, sections parallel to b3 fold axes, exhibit SC-fabrics and ecc-structures indicative for N-NE directed shearing (Fig. 11f). Overprinting criteria like lineations of intersections parallel to b3 occur. A shear fold indicating NNE-directed shearing was observed up to the Ramolhut, which is considered as F2 fold structure (Fig. 11g).

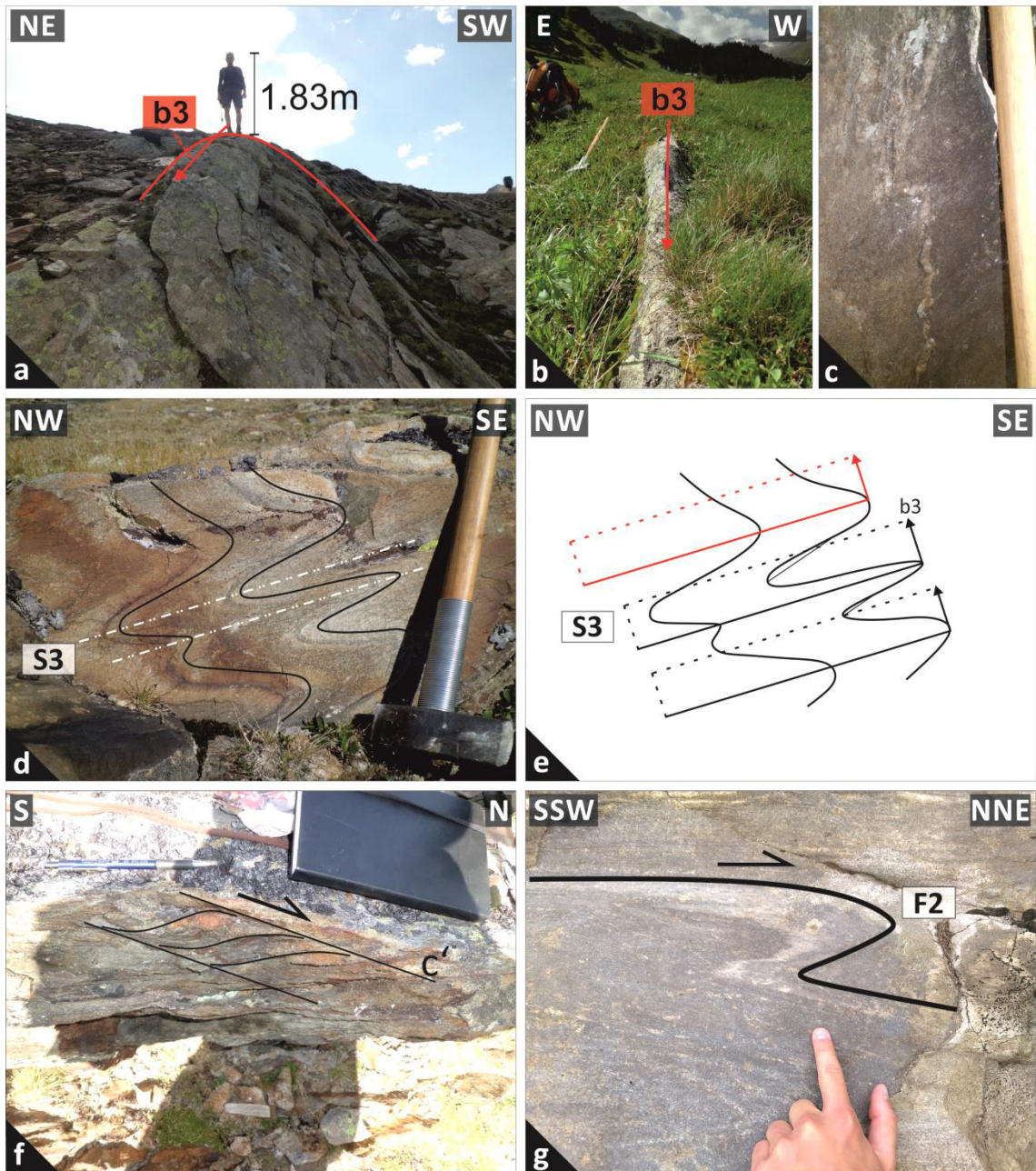


Figure 11 (a/b) Fold hinge with F3 fold axes plunging shallowly to the N. Hohe Mut/ Obergurgl village (c) Parasitic folds attributed to F3. (d/e) Isoclinal fold. Hohe Mut. (d) Dashed-dotted white line indicates axial plane foliation (S3). Black line characterizes the isoclinal parasitic fold of a large-scale tight fold (F3). (e) Sketch shows axial planes in red dipping to the NW; direction of the arrows illustrates the fold axes b3. (f) ECC-structure indicating N-directed shearing. Hohe Mut (g) Shear fold (F2) indicating NNE directed shearing (D2). Way up to the Ramolhut.

3.2.3 Part B: Ramolhut to Ramoljoch

Length: ca. 2.5 km; Orientation: NW-SE

Along part B orthogneisses are integrated in the large-scale tight fold structure (F3). The foliation S3 continuously changes its strike direction from NE-SW (location of sample R3) to NNW-SSE near the Ramoljoch with a variety in dip angle between 45 and 70°. Additionally, plunge directions of fold axes reflect rotation from NNE (part A) to NW (part B). Micaschists indicate a more pronounced axial plane foliation (S3) than paragneisses (Fig. 12a). Locally migmatized paragneisses occur as tight incoherent folds (ptygmatic folds; Fig. 12b) consisting of partial melted material (meso-melanosomes). Lower order folds occur as D3-related Z-shape structures on the way up to the Ramoljoch (Fig. 12c).

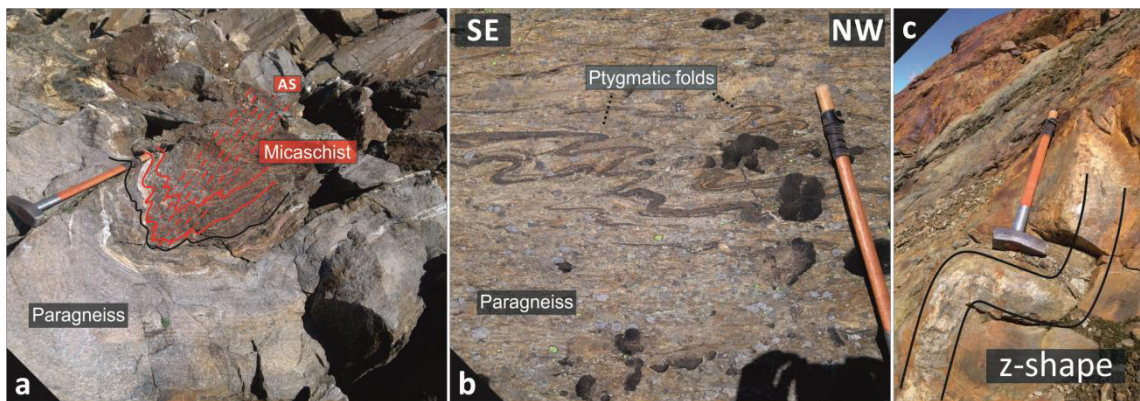


Figure 12 (a) More pronounced axial plane foliation in the micaschists (fold core), missing in the surrounding paragneisses. Near Ramolhut. (b) Meso-melanosome ptygmatic folds in migmatized paragneisses. Near the Ramoljoch. (c) Z-shape fold structures (D3). Near the Ramoljoch.

Ductile shear folds (F2) as well as sigmoidal quartz clasts formed due to SE-directed shearing D2 (Fig. 13a). Locally, D4-related ESE-directed normal faults overprint D2-ductile structures (Fig. 13b).

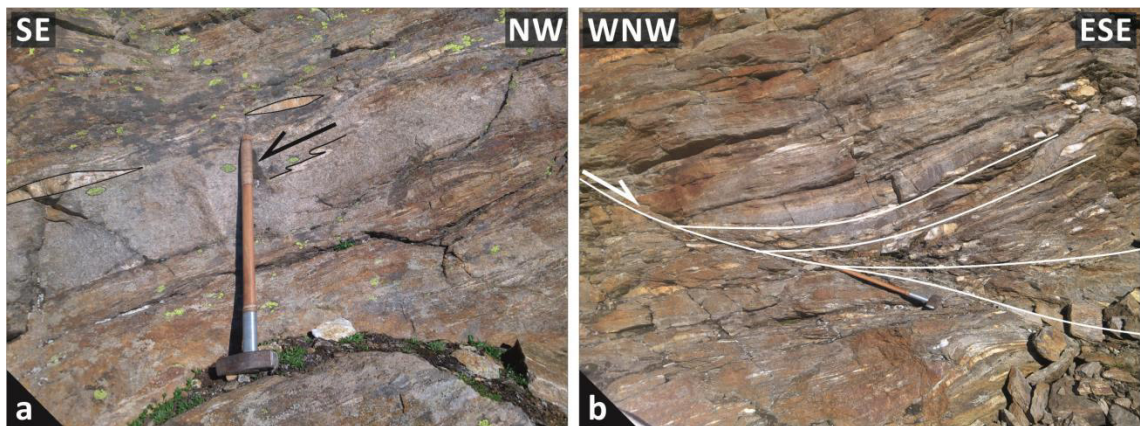


Figure 13 (a) Shear fold F2 and sigmoidal quartz clasts, both indicating shearing to the SE. Near Ramolhut. (b) Late ESE-directed normal faults.

3.2.4 Part C: Ramoljoch to Vent village

Length: ca. 3.5 km; Orientation: NE-SW

Besides paragneisses, micaschists and amphibolites, unconsolidated rocks with large snowball-garnets and hornblendes, probably attributed to the Schneeberg Complex, have been found. The foliation strikes NW-SE with dip angles ranging between 50 and 90°. Shear folds with fold axes plunging steeply to the NW dominate. They correspond to D2 and are SE vergent (Figs. 14a/b and Fig. 15f).

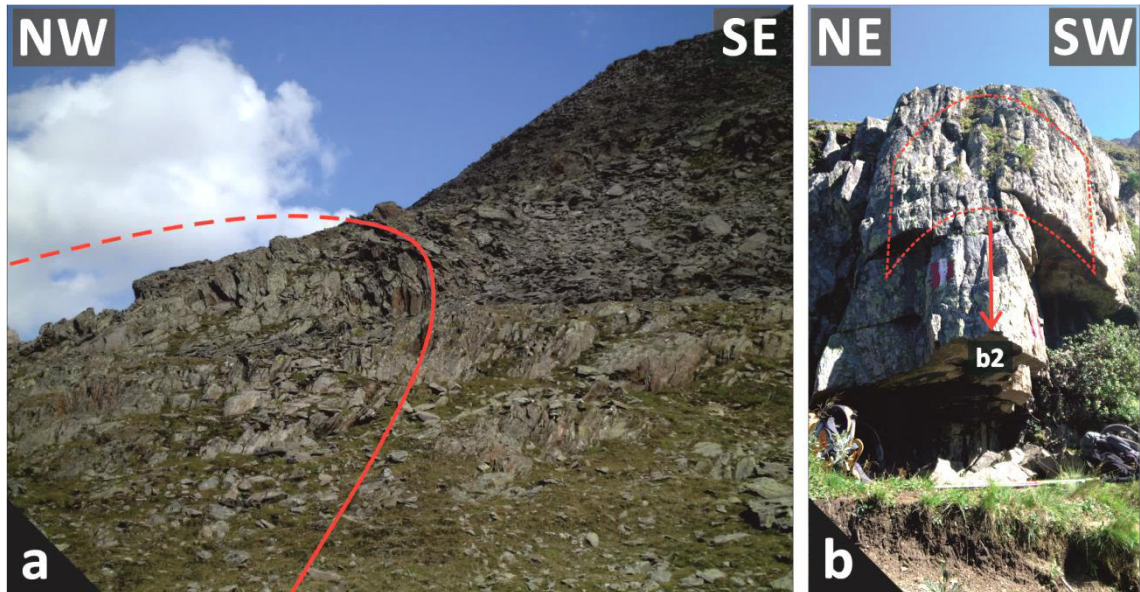


Figure 14 (a) Asymmetric shear fold F2. (b) Fold hinge attributed to F2 with steep NW dipping fold axis. Near Diembach.

Fold structures with fold axes plunging shallowly to the NW are found along the Diembach (samples MS 60 to MS 68) and attributed to F3. F2 and F3 result in superposition indicative for fold interference type O_2 after Grasemann et al. (2004) (Figs. 15a/c/e). Parasitic folds, Z- and M-structures, attributed to F2 have been observed (Fig. 15b).

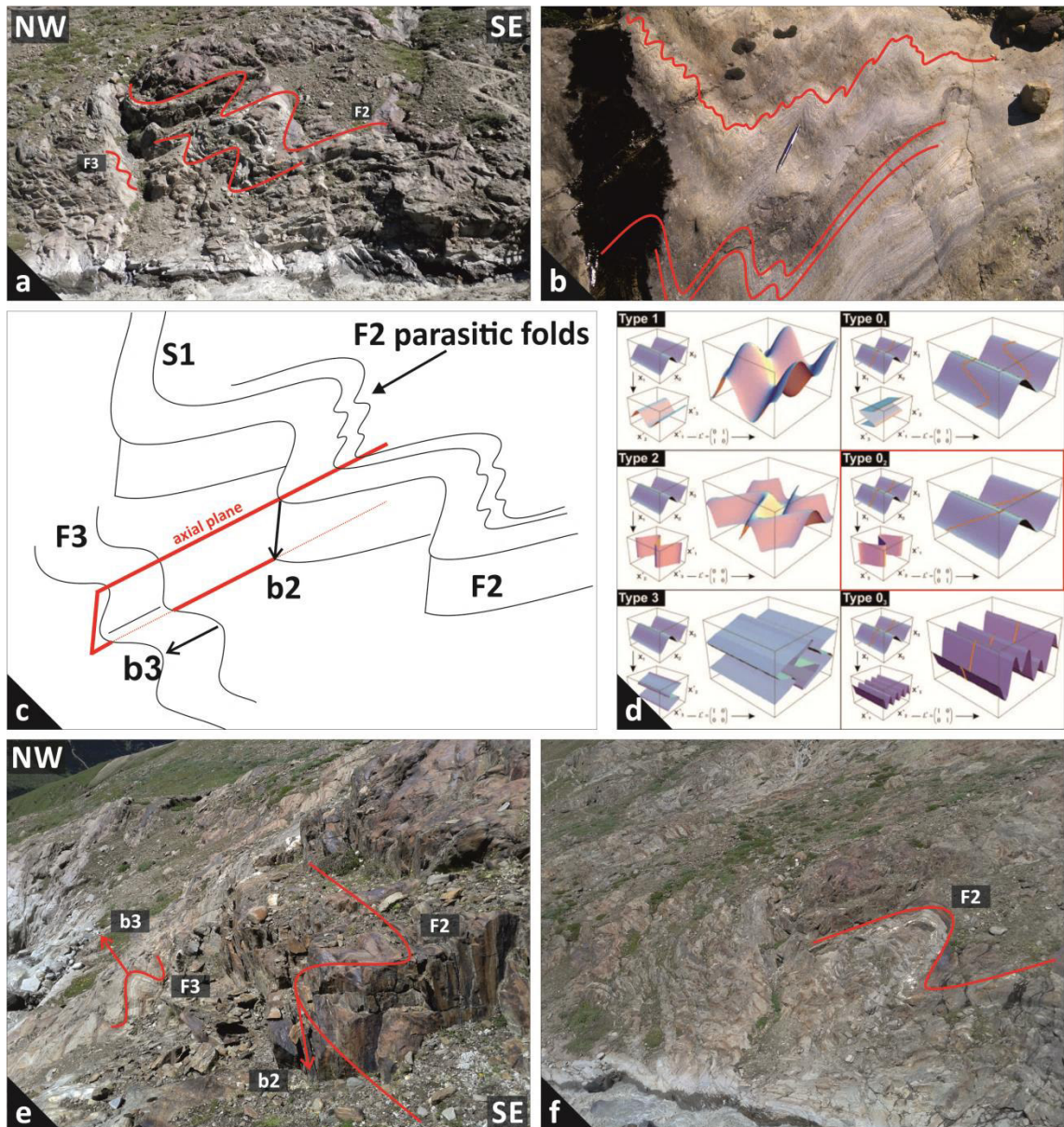


Figure 15 (a) Superposition of shear fold F2 and fold F3, which results in a fold interference type 0_2 after Grasemann et al. (2004). (b) Small-scale F2-parasitic structures. (c) Structural sketch of (a) for the fold interference type displayed in (d). Along Diembach (samples MS 60-68). (e) F2 and F3 fold structures. (f) SE-vergent F2 fold structure.

Most of the occurring shear sense indicators, like shear folds and sigmoidal quartz clasts point to D2 related SE-directed shearing (Figs. 16a/b). A NW-SE striking shear zone which dips steeply towards NE defines a local D5-shearing event (for location see Appendix 1 or Appendix 4). En-echelon extension veins within the shear zone indicate vertical exhumation (Figs. 16c), whereas the opening of vein structures points to NW-directed shearing (D5) (Fig. 16d). Two types of stretching lineation have been observed. Subhorizontal NW-directed stretching lineations have been found in the shear zone area (sample R14 and R15), while vertical stretching lineations occur at the area around Diembach.

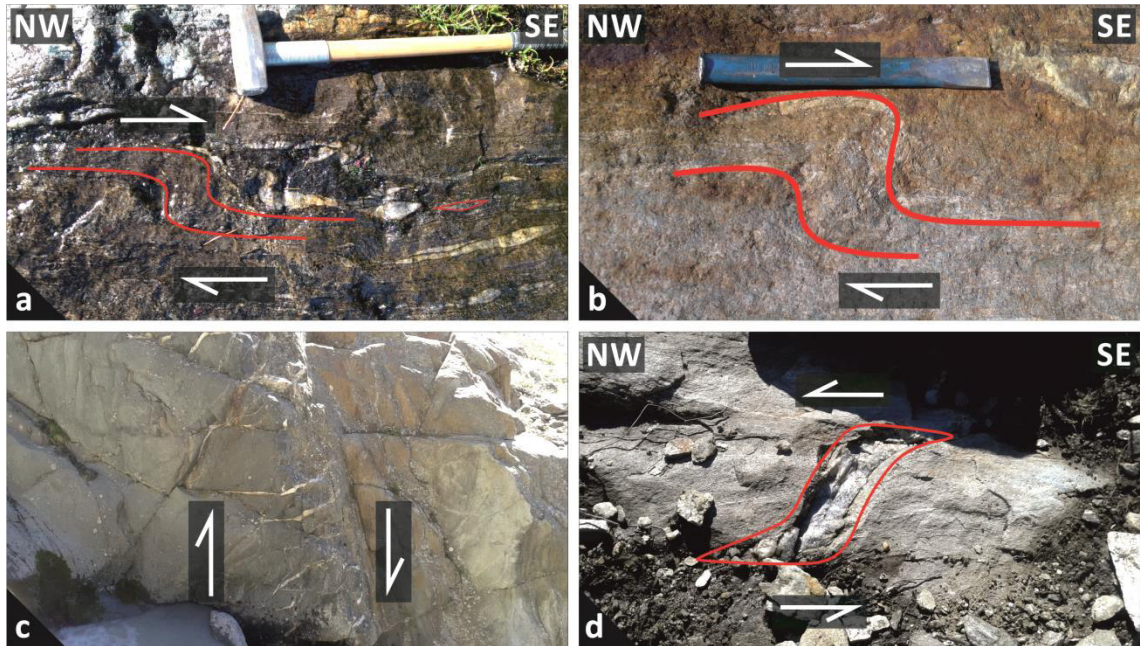


Figure 16 (a/b) Shear folds (F2) indicating a SE-directed shear sense. (c) D5-related en-echelon extension veins indicative for a vertical exhumation. (d) D5-related vein structure indicative for NW-directed shearing and vein opening. Near Diembach.

3.3 Petrography and microstructural analysis

A detailed petrographic study was performed on ca. 100 polished thin sections, sampled along the profiles (A, B and C) (see Appendix 6). Lithologies are generally represented by metasediments (paragneisses and micaschists), as well as minor amphibolites and orthogneisses. Rock names are based on visually estimated modal contents of rock forming minerals (quartz/feldspar to mica ratio). A detailed petrographic description of occurring lithologies, as well as information about micro-structural features is given below.

3.3.1 Garnet-bearing paragneiss

Paragneisses generally contain mineral assemblages of garnet + biotite + chlorite + mica + quartz + feldspar + sericite. Minor amounts of epidote-zoesite group minerals as well as amphiboles are restricted to the shear zone in profile C. Accessoric phases are represented by tourmaline, titanite, zircon, apatite and opaques (ilmenite and rutile).

Garnet-bearing paragneisses are the most common lithology along the profiles (A, B and C). They differ in their quartz/feldspar ratio, as well as in the occurrence of coarser-grained mica-rich bands. Their quartz and feldspar contents change in dm sizes. Quartzitic layers mostly show recrystallized quartz due to grain boundary migration (GBM), indicative for temperatures above 500°C (Stipp et al., 2002). Locally straight grain boundaries display grain boundary area reduction (GBAR), suggesting temperature dominant imprint (Fig. 17a). Intercalated coarse grained foliation parallel mica-rich shear bands are observed locally (Fig. 17b). Feldspar-rich layers can form large completely sericitized feldspar clasts. Garnets are predominantly found as polymetamorphic grains with inclusion-rich cores and inclusion-free rims and are locally concentrated nearby areas of strongly sericitized feldspar clasts (Fig. 17c). The polymetamorphic garnets consist of a pre-*eo*-Alpine core, sometimes preserving an older foliation. Garnets without any inclusions or visible zonation are also preserved, probably indicative for a monometamorphic *eo*-Alpine origin (Fig. 17d). Paragneisses show a main foliation made up by biotite, white mica and quartz. Late growth of biotite porphyroblasts which are often retrogressed to chlorite is observed. Near shear zones the paragneisses display dominant fine grained chlorite and zoisite (< 0.2 mm). Along with sericite, those minerals are arranged in radial directions that overgrew larger feldspar grains. In mylonitic paragneisses (e.g. sample R14) sigmoidal garnet porphyroclasts with asymmetric pressure shadows indicate NW-directed shearing (Fig. 17e). Sigmoidal garnet porphyroclasts and biotite mica fishes at the area around Diembach (sample MS60-68) point to a nearly vertical exhumation of the earlier ductile structures (Fig. 17f).

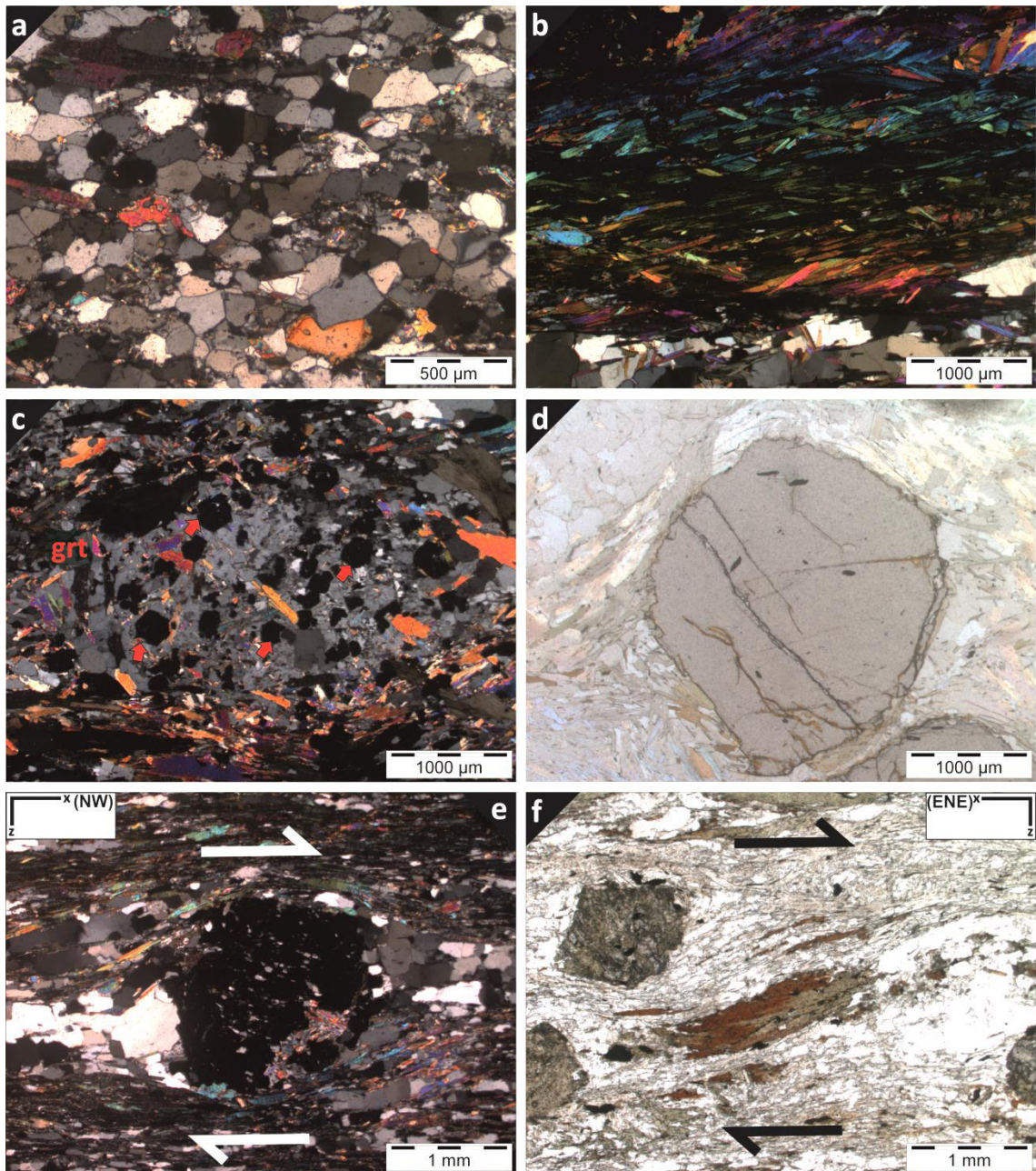


Figure 17 (a) Besides GBM GBAR is the dominant deformation mechanism. (b) Mica band within heterogeneous paragneisses. (c) Strongly sericitized feldspar clasts. (d) Large garnets with no evidence for zonation. (e) Sigmoidal garnet porphyroclasts in mylonitic paragneiss indicative for NW-directed shearing. (f) Micafishes indicating vertical exhumation (average dip angle of 80°). Area at Diembach.

From A to C a change in garnet morphology, zonation and grain size is visible, leading to a textural subdivision into the following types:

Type I (Fig. 18a): Polymetamorphic, fine-grained garnet (< 0.6 mm) with inclusion-rich cores (pre-*eo*-Alpine) and inclusion-free rims (*eo*-Alpine).

Type II (Fig. 18b): Partially angular shaped euhedral garnets with clearly visible optical zoning, forming up to 1 mm large grains.

Type III (Figs. 18c/d): Medium to coarse-grained (up to 6 mm) garnet poikiloblasts with several inclusions of quartz and opaque phases. These inclusions are distributed throughout the core of the garnet and form grains up to 0.3 mm. No visible zonation occurs.

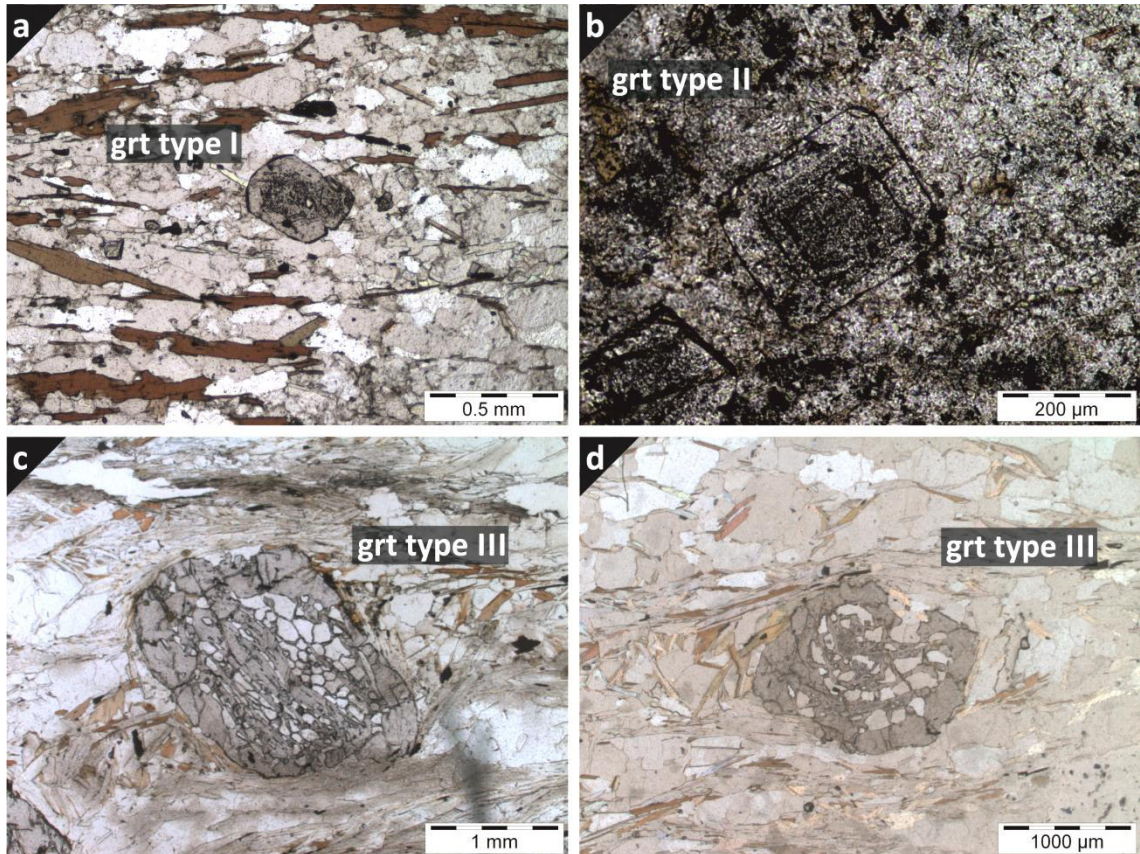


Figure 18 Most common garnet (grt) type along part A and B (a) garnet type I with inclusion-rich core and inclusions-less rim. (b) Garnet type II displays angular shape and sharp defined boundaries between inclusion-rich and inclusion-less rims. Garnet type II occurs only along a small area at the end of profile A, up to the Ramoljoch. Most common garnet type along part C (c/d) snowball garnets with inclusions of quartz (< 0.3 mm) and opaque phases in places.

3.3.2 Micaschists

Garnet - bearing micaschists

Garnet - bearing micaschists contain mineral assemblages of garnet + biotite + mica + quartz ± feldspar ± chlorite ± epidote. Accessories are tourmaline, rutile and zircon.

Garnets show variations in grain size (0.2 mm to 6 mm), morphology and visible zonation, similar to the paragneisses described above. The dominant deformation mechanism of quartz is GBM, indicative for temperatures above 500°C. Locally high amounts of tourmaline could be observed.

Garnet ± kyanite micaschist with white mica pseudomorphs after staurolite

Common mineral assemblages in these micaschists are beside white mica pseudomorphs after staurolite garnet + biotite + chlorite + mica + quartz ± feldspar ± kyanite.

The occurrence of pseudomorphs after staurolite, which are composed of extremely fine grained white mica and quartz (< 0.1 mm) gives the rocks a mottled look (Fig. 19a). Idiomorphic garnets (< 0.4 mm) with no optical zonation are situated within these staurolites (up to 5 mm in size), as well as next to them. Locally kyanite is found, forming grains up to 2 mm in-size. Relics of staurolites sometimes incorporate pre-*eo*-Alpine foliations S0 (Fig. 19b). Spaced foliations, probably formed during formation of S1, preserve microlithons that contain coarse-grained white mica and quartz. Microlithons comprise microfolds of previous foliation S0 (Figs. 19c/d).

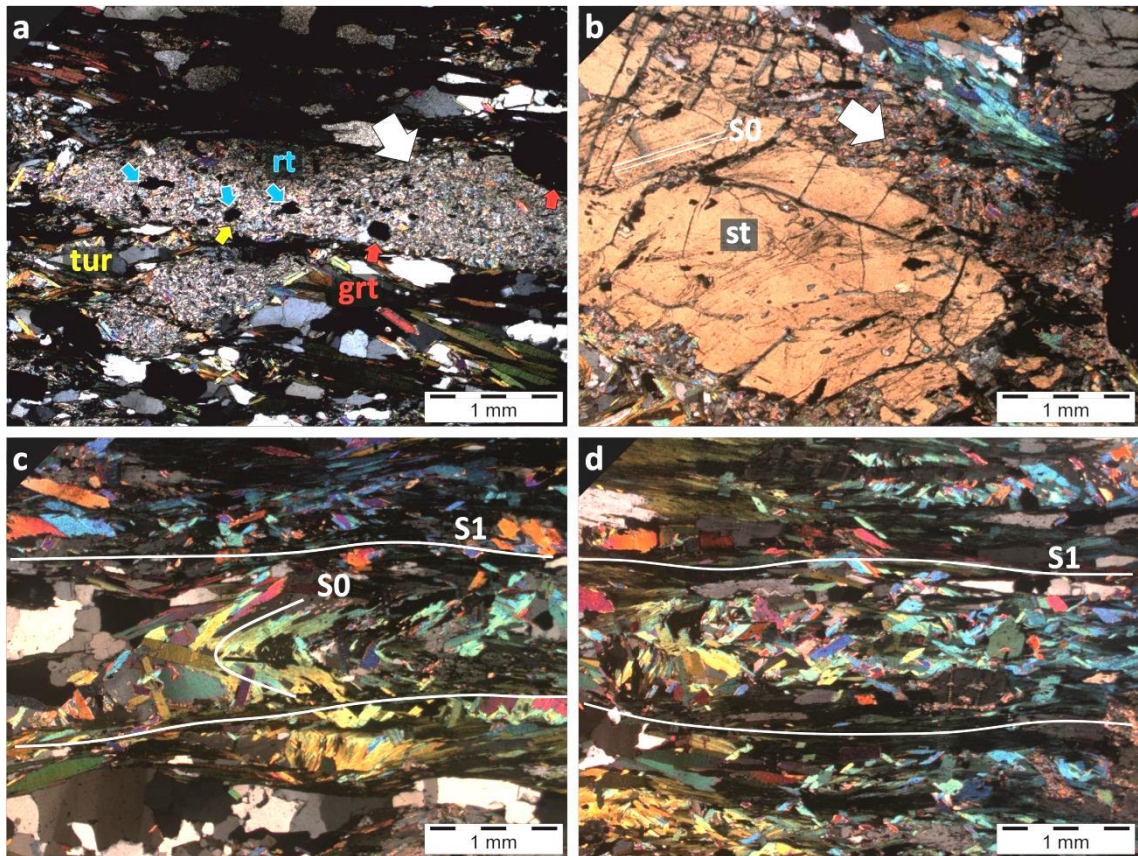


Figure 19 (a) Characteristic staurolite (st) twins, replaced by white mica pseudomorphs after staurolite (white arrows). Inclusions within the extremely fine grained white mica and quartz matrix are garnet (grt, red arrows), tourmaline (tur, yellow arrows) and rutile (rt, blue arrows). (b) Pre-*eo*-Alpine foliation (S0) within staurolite. (c) Spaced foliation with microfolds in between. (d) Microlithons with coarse-grained mica.

3.3.3 Amphibolites

Amphibolites vary in their grain size and mineral assemblages. Most common rock forming minerals are amphibole + quartz + feldspar ± garnet ± epidote ± clinozoisite ± biotite ± chlorite ± carbonate. Titanite, rutile, zircon and apatite represent the accessory phases.

Amphiboles differ in size between fine- (< 0.2 mm) to coarse-grained (up to 1 cm), contrasting to garnet schists, which contain amphibole aggregates larger than 1 cm. A further distinct feature is the variation between a foliated or static growth of amphiboles. Polymetamorphic garnets are characterized by inclusion-rich cores and inclusion-free rims and form grains up to 0.8 mm in size.

Detailed study of one amphibolite outcrop at the Bärenhoppet (profile part A) results in the characterization of four types of amphibolite layers:

Type I: Consists of the mineral assemblage garnet + clinozoisite + amphiboles + epidote + quartz + feldspar ± carbonate. The matrix consists of up to 2 mm large amphiboles and clinozoisite. Small amounts of quartz and feldspar are present. Polymetamorphic garnets occur subordinately (Fig. 20a).

Type II: Compared to type I, type II amphibolites display a foliation composed of clinozoisite (< 2.5 mm), epidote (< 0.5 mm) and amphibole (< 2 mm) (Figs. 20b/c/d). Garnet is absent in this type.

Type III: Foliation is only locally present. Type III is characterized by biotite- and chlorite-rich layers, whereas biotite (< 2 mm) is strongly retrogressed to chlorite (Fig. 20e).

Type IV: Is restricted to the outer areas of amphibolites. This type is more fine-grained and exhibits a foliated matrix consisting of small amphiboles (< 0.6 mm) and quartz (< 0.4 mm). Typical for this type is the late growth of biotite porphyroblasts (up to 5 mm), as well as the minor occurrence of garnet (Fig. 20f).

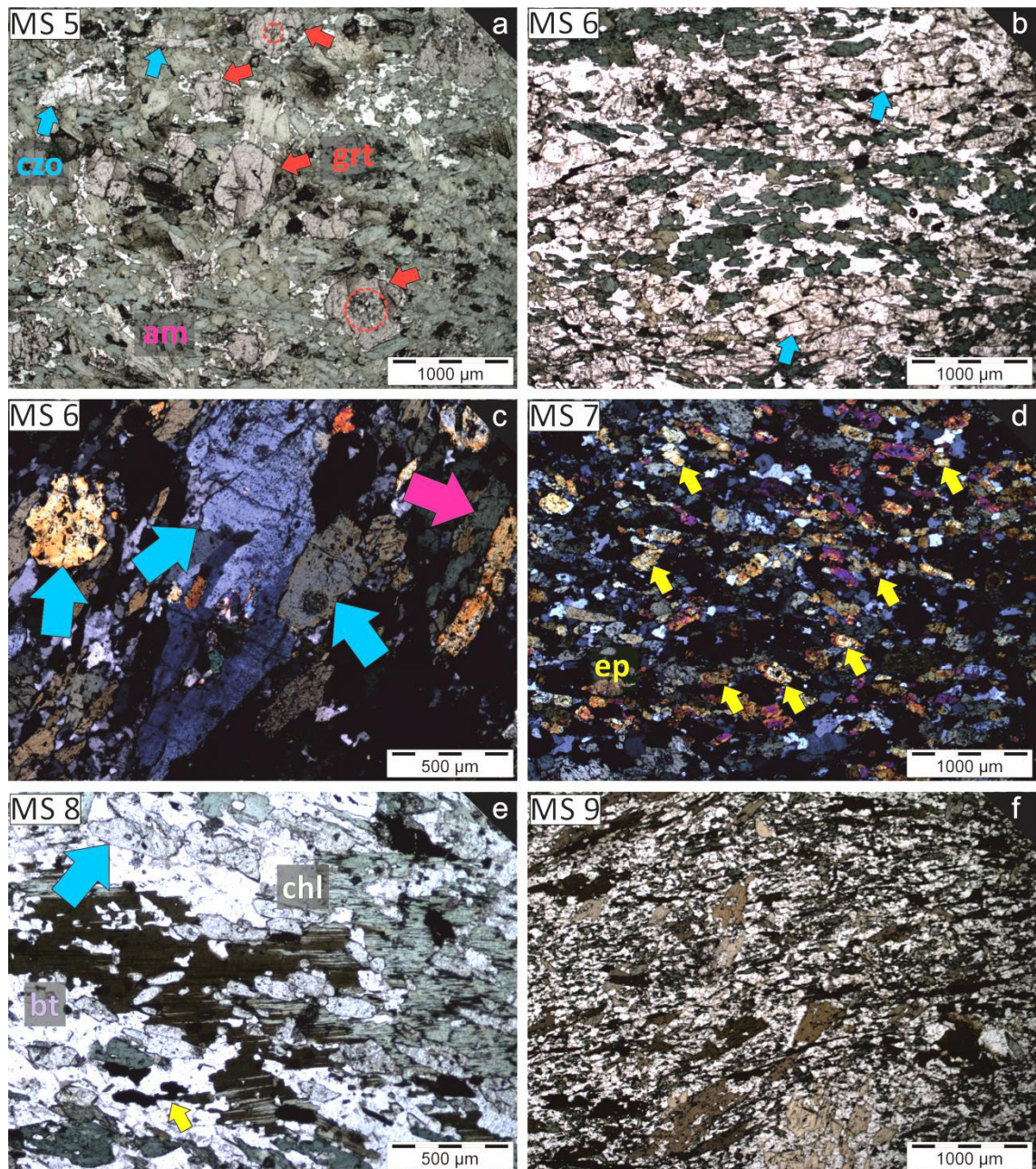


Figure 20 Detailed amphibolite profile along a dm thick layered amphibolite at Bärenhoppet. (a) Polymetamorphic garnets (grt, red arrows) within an amphibole- and clinozoisite-rich matrix from type I amphibolite layer. Red circle points to inclusion-rich garnet core. (b) Type II amphibolite layer with characteristic foliation made up by large grains of clinozoisite (czo, blue arrows) and amphiboles (am). (c) Type II: Clinozoisite (blue arrows) and amphiboles (magenta arrow) under crossed nicols. (d) Type II: Fine grained layer composed of epidote (ep, yellow arrows) amphibole and quartz, as well as clinozoisite in places. (e) Type III amphibolite layer with large biotite (bt) porphyroblasts locally retrogressed to chlorite (chl). Blue and yellow arrows exhibit clinozoisite and epidote, respectively. (f) Type IV foliated fine grained amphibolite layer.

Amphibolites along profile C exhibit similar characteristics to the amphibolite at Bärenhoppet area (profile part A). Significant differences however are coarse-grained partly retrogressed amphiboles (< 6 mm) and garnets up to 3 mm in size (Figs. 21a-d). The latter contain inclusions of quartz and opaque phases similar to garnet type III from the paragneisses/micaschists.

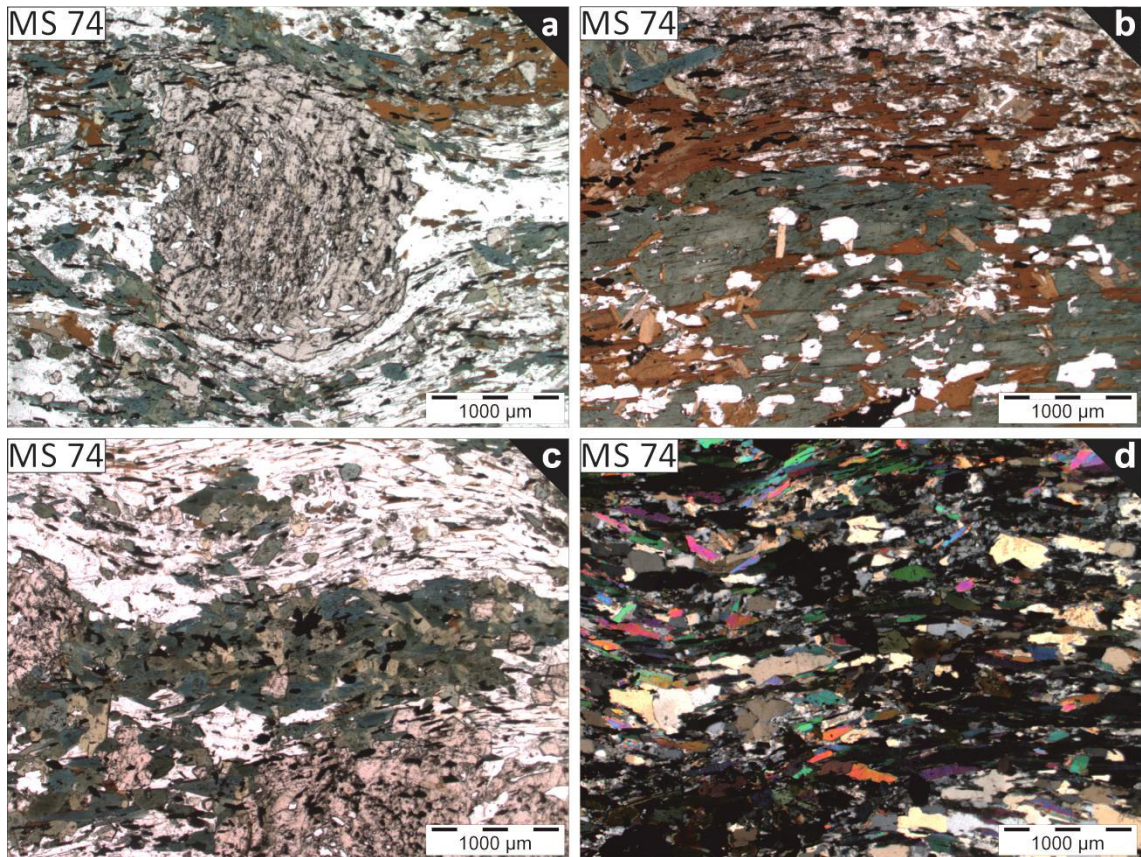


Figure 21 (a) Coarser grained amphiboles from profile C with inclusion-rich (quartz and opaque phases) type III garnet. (b) Local replacement of large amphiboles (up to 6mm) by biotite. (c) Fine grained amphiboles intercalated in foliated amphibolite layers. (d) Foliated amphibolite with white mica and quartz bands.

3.3.4 Mineral chemical analysis of amphibolites

Mineral chemical analysis (see Appendix 7) of amphiboles has been performed on representative polished thin sections to compare different amphibolites along the sampled profiles (A, B and C), for sample location of studied amphiboles (MS 6, MS 60, MS 75 and R 13) see Appendix 1 or 2, 3 and 4. The study was conducted with a scanning electron microscope JEOL JSM-6310, attached to a wavelength dispersive system with an acceleration voltage of 15 kV, at the University of Graz, Department of Mineralogy and Petrology.

To compare the different outcropping amphibolites in the studied profiles four amphibolites were selected and analyzed on representative polished thin sections:

- MS 6 from profile part A: clinozoisite-epidote bearing amphibolite
- R13 from profile part B: coarse-grained amphibolite
- MS 60 from profile part C: coarse-grained amphibolite
- MS 75 from profile part C: coarse-grained amphibolite

Chemical analyses of amphiboles from representative samples display no clear differences (Figs. 22a-c). They were identified as calcic amphiboles, plotting in the hornblende / edenite and tschermakite / pargasite fields (Fig. 22a) and differ in Si and Na+K contents in the tetrahedral or the A-site of the IMA-amphibole classification scheme after Leake et al. (2004), respectively. Al amounts in the tetrahedral site range between 1.614 and 1.002. Latter variations are interpreted as exchange reactions with enclosed minerals such as titanite and plagioclase. Magnesianhornblende and ferrohornblende have $(\text{Na}+\text{K})_A$ values < 0.5 , whereas edenite, pargasite and ferropargasite have $(\text{Na}+\text{K})_A$ values > 0.5 . Furthermore amphiboles show patchy optical zonation (Fig. 23). Thus similar metamorphic conditions, as well as similar origin can be assumed for the metabasites in the study areas.

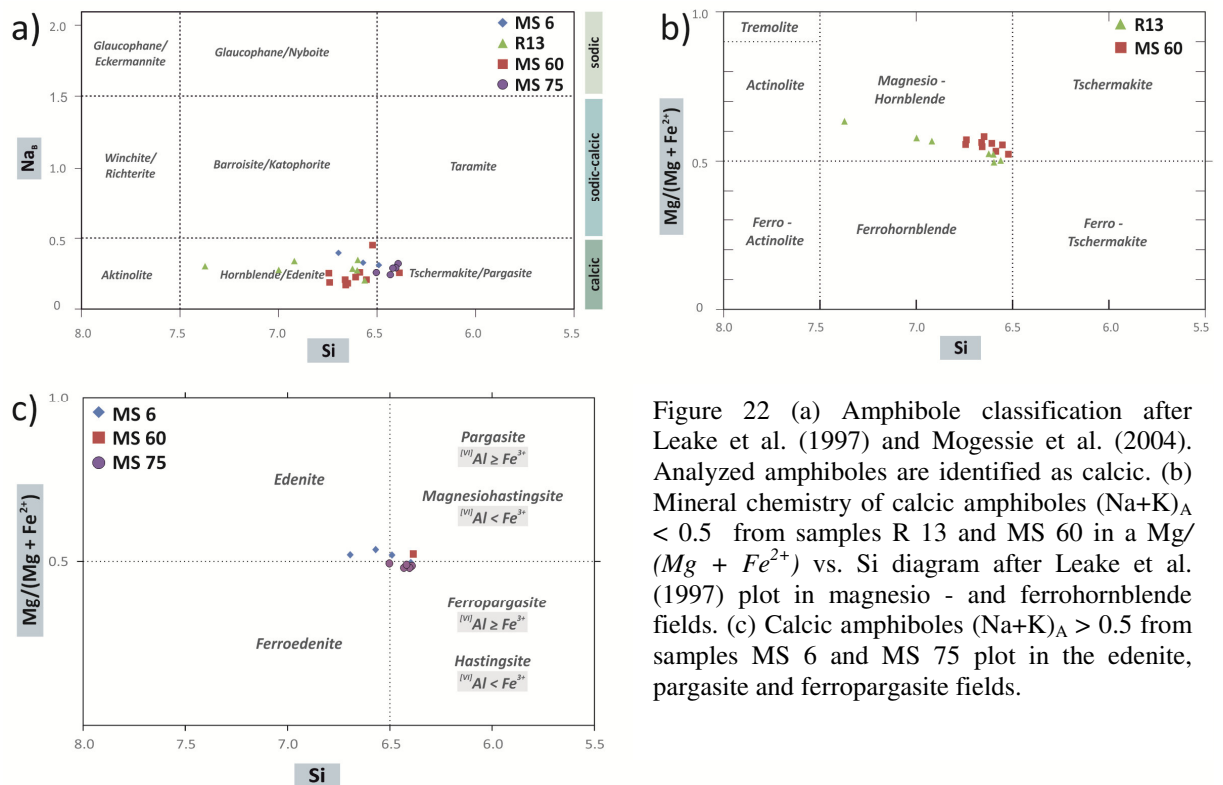


Figure 22 (a) Amphibole classification after Leake et al. (1997) and Mogessie et al. (2004). Analyzed amphiboles are identified as calcic. (b) Mineral chemistry of calcic amphiboles $(\text{Na}+\text{K})_A < 0.5$ from samples R 13 and MS 60 in a $\text{Mg}/(\text{Mg} + \text{Fe}^{2+})$ vs. Si diagram after Leake et al. (1997) plot in magnesian- and ferrohornblende fields. (c) Calcic amphiboles $(\text{Na}+\text{K})_A > 0.5$ from samples MS 6 and MS 75 plot in the edenite, pargasite and ferropargasite fields.

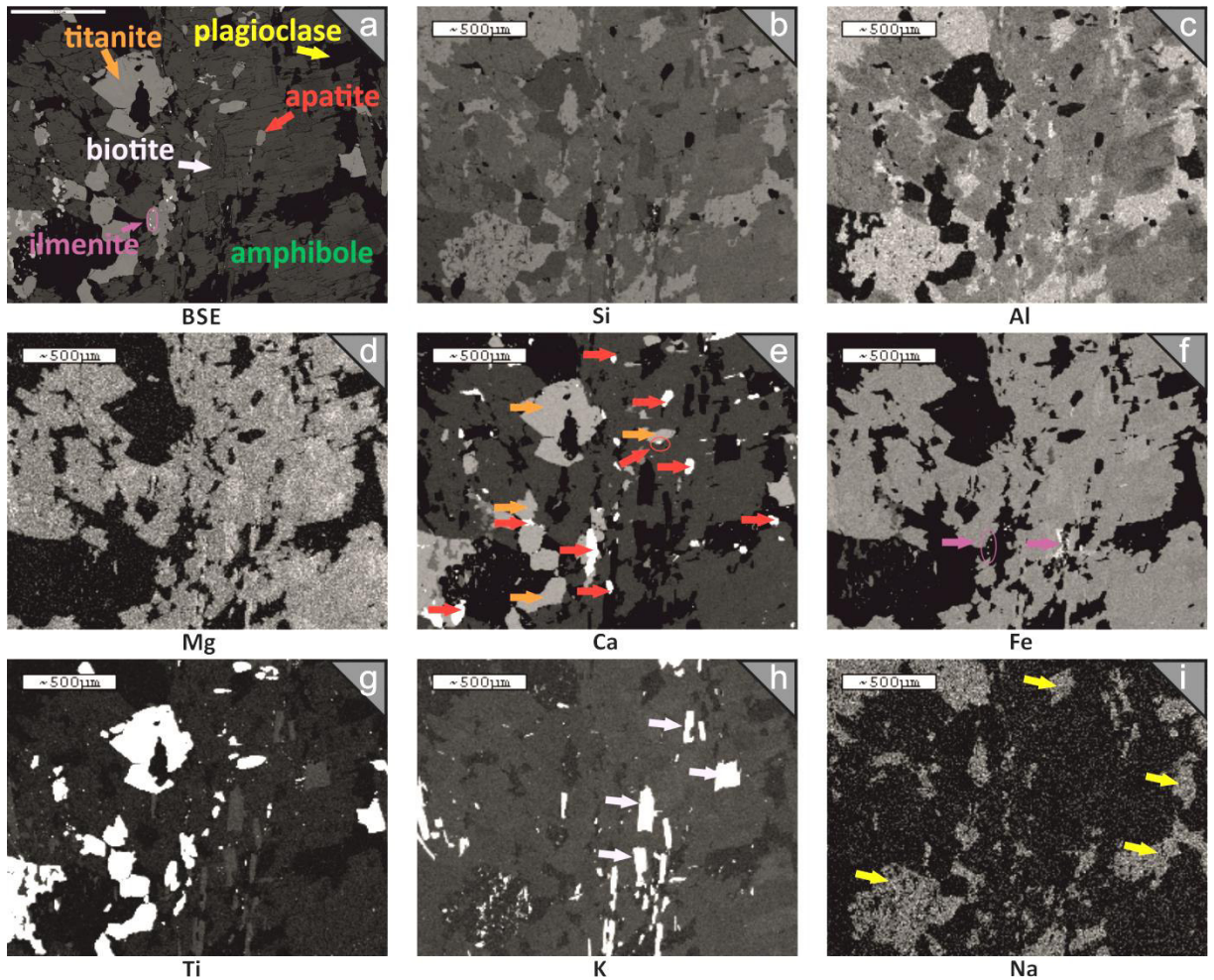


Figure 23 (a) Back scattered electron (BSE) image from amphiboles with inclusions of biotite (light purple), plagioclase (yellow arrow), titanite (orange arrows), apatite (red arrows) and ilmenite (pink arrows). (b) – (i) Element distribution images from amphiboles. (b) Si $K\alpha$; (c) Al $K\alpha$; (d) Mg $K\alpha$; (e) Ca $K\alpha$; (f) Fe $K\alpha$; (g) Ti $K\alpha$; (h) K $K\alpha$; (i) Na $K\alpha$;

3.3.5 Orthogneiss

Orthogneisses are made up by kalifeldspar + plagioclase + quartz + mica. Accessories are represented by tourmaline and epidote.

Kalifeldspar developed as large Karlsbader twins (< 3.5 mm) (Fig. 24a), whereas plagioclase forms polysynthetic twins. Further feldspar appearances are either in perthitic textures (Figs. 24a/b) or as sericitized plagioclase (< 3mm) (Figs. 24c/d). The weak foliation is composed of quartz (< 0.5 mm) and white mica (< 1.5 mm). The latter is locally accompanied by partly chloritized biotite laths. Small rounded or elongated epidotes overgrow these white mica bands. Quartz shows grain boundary migration recrystallization features, indicative for temperatures > 500°C. Feldspar exhibits bulging and locally core-mantle textures, indicative for temperatures > 500°C (Passchier and Trouw, 2005). Feldspar porphyroclasts display no sense of shear.

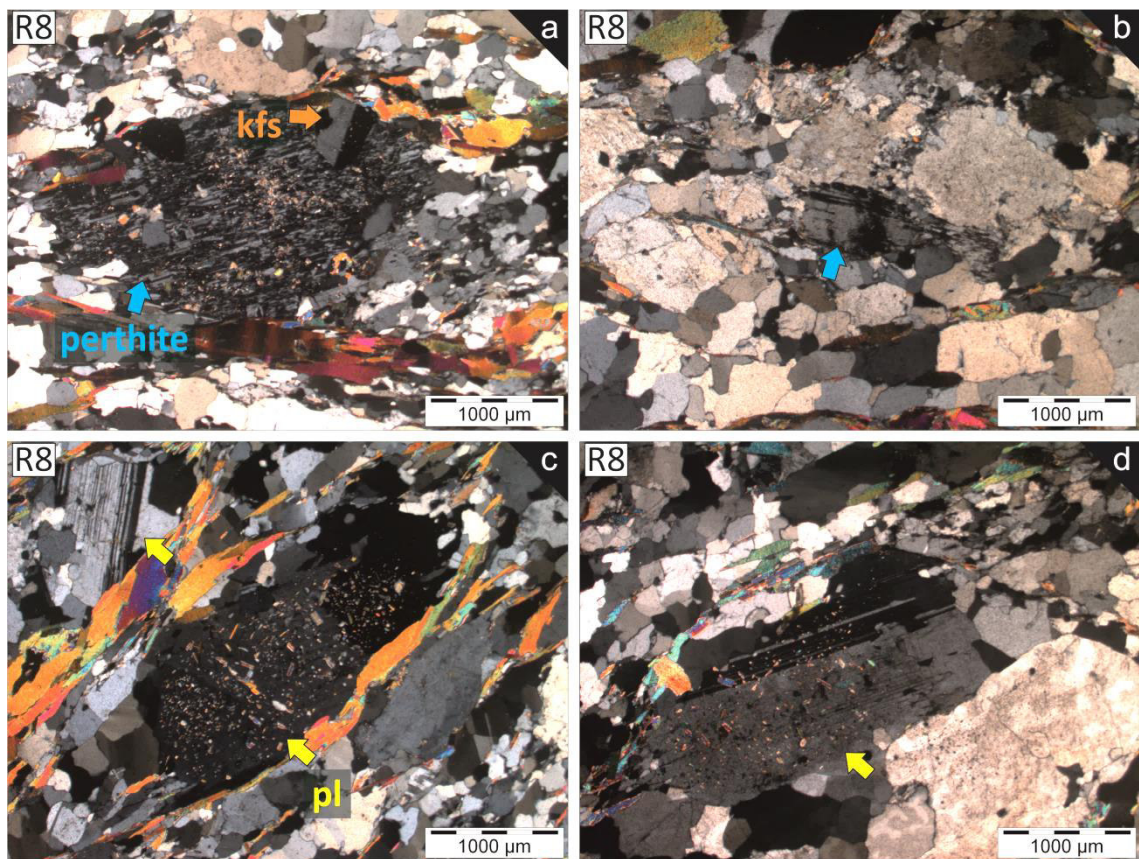


Figure 24 Orthogneisses. (a) Characteristic Karlsbader twins (kfs, orange arrow) with perthitic exsolution of two feldspars (blue arrows). (c/d) Partly sericitized coarse-grained plagioclase (pl, yellow arrows) with exsolution lamellae in (d).

4. Discussion

4.1 The low-angle normal fault near Ramolhut and the discrete shear zone at profile C (study area A in Fig. 25)

The ESE directed normal fault, defined as D4, can probably be linked with ESE directed Cretaceous extension tectonics (Duncan-Ela phase in Froitzheim et al., 1997). The discrete shear zone (D5) is documented by two stretching lineations which would indicate activity as result of transpressional or transtensional tectonics. A subhorizontal stretching lineation results from sinistral shearing. Locally steep plunging stretching lineations point to a vertical exhumation of deeper levels. In order to decide which system (transpressional or transtensional) already proposed fault systems nearby this study area should be discussed. Flöss (2009) and Speckbacher (2009) described the occurrence of sinistral transtensional shear zones in the Texel Complex that are related to movements along the Passeier-Jaufen-Fault.

4.2 Structures of the Ötztal Complex (ÖC) compared with structures of the Texel Complex (TC)

Regarding to the results of Exner et al. (2002) from the TC, near to Meran, South Tyrol petrographic similarities occur (study area C in Fig. 25). There at least three different orthogneiss types are described which consist of similar mineral assemblages and fabrics like the orthogneisses of this work, especially Wm-orthogneisses (study area A in Fig. 25). Additionally, Flöss (2009) and Speckbacher (2009) described in their unpublished master theses the N-directed continuation of an orthogneiss at the southwestern end of the Schneeberg Complex, in the Pfossen- and Zieltal area (study area D in Fig. 25). Thus it is proposed that the orthogneisses near the Ramoljoch represents the northern continuation from the TC to the ÖC (study area A in Fig. 25). Sölva et al. (2001) discussed the eo-Alpine deformation phases within the TC and defined four exhumation related deformation stages (study area B in Fig. 25). After foliation development D1, the presence of D2 shear folds and D3 large-scale tight folds suggests that the D2 and D3 folding events in the TC are similar to structures observed in the study area (study area A in Fig. 25). A sketch in figure 25 explains the

comparable folding events within the ÖC and within the TC. Differences in orientation of field structures may be the result from late indentation tectonics which probably results into rotation of eo-Alpine structures (e.g. Krenn et al., 2001).

Due to these petrographic and structural similarities of both complexes, which are currently considered as different tectonic units within the Austroalpine basement nappes, it is proposed that both complexes may arise from the same tectonic plate before and during eo-Alpine subduction. This would further argue for a lower tectonic plate position of the ÖC with its deeper subducted continuation, the TC, which contains eo-Alpine eclogites.

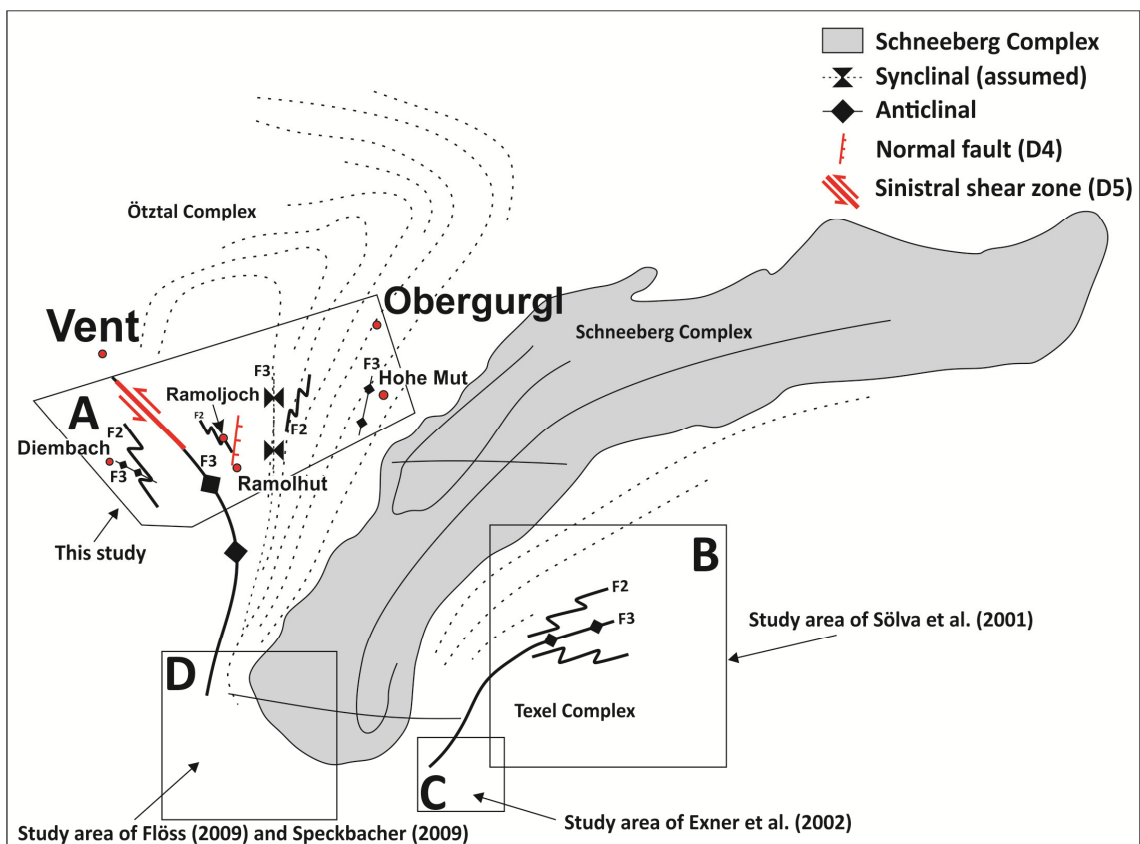


Figure 25 Sketch of the discussed study areas. Trend of the foliation (pointed lines) after Purtscheller (1978). A this study; B Sölva et al (2001); C Exner et al. (2002); D Flöss (2009) and Speckbacher (2009);

References

- Exner, U., Grasemann, B., Thöni, M., & Miller, C. (2002). Relative chronology and absolute age dating of structures related to eo-Alpine high-pressure metamorphism and Oligocene magmatism in the SE Ötztal complex (Texel Group, South Tyrol, Italy). *Mitteilungen naturwissenschaftlicher Verein Steiermark*(132), pp. 63-82.
- Flöss, D. (2009). Tektonometamorphe Entwicklung der westlichen Austroalpinen Einheiten: Geometrie und Kinematik der eoalpinen Kollision (Texel Komplex, Südtirol). *Unpublished master thesis*.
- Froitzheim, N., Conti, P., & van Daalen, M. (1997). Late Cretaceous, synorogenic, low-angle normal faulting along the Schlinig fault (Switzerland, Italy, Austria) and its significance for the tectonics of the Eastern Alps. *Tectonophysics*(280), pp. 267-293.
- Grasemann, B., Wiesmayr, G., Draganits, E., & Füsseis, F. (2004). Classification of Refold Structures. *The Journal of Geology*(112), pp. 119-125.
- Habler, G., Thöni, M., & Sölva, H. (2006). Tracing the high pressure stage in the polymetamorphic Texel Complex (Austroalpine basement unit, Eastern Alps): P-T-t-d constraints. *Mineralogy and Petrology*(88), pp. 269-296.
- Hoinkes, G. (1973). Die Anatexis des Winnebachgranites (Ötztaler Alpen, Österreich) am Beispiel eines Aufschlusses. *Tschermaks Mineralogische und Petrographische Mitteilungen*(20), pp. 225-239.
- Hoinkes, G. (1981). Mineralreaktionen und Metamorphosebedingungen in Metapeliten des westlichen Schneebergerzuges und des angrenzenden Altkristallins (Ötztaler Alpen). *Tschermaks Mineralogisch Petrographische Mitteilungen*(28), pp. 31-54.
- Hoinkes, G., & Thöni, M. (1993). Evolution of the Ötztal-Stubai, Scarl-Campo and Ulten basement units. (J. Raumer, & J. Neubauer, Eds.) *Premesozoic geology in the Alps*, pp. 485-494.
- Hoinkes, G., Koller, F., Rantitsch, G., Dachs, E., Höck, V., Neubauer, F., et al. (1999). Alpine Metamorphism of the Eastern Alps. *Schweizerische Mineralogische und Petrographische Mitteilungen*(79), pp. 155-181.
- Hoinkes, G., Kostner, A., & Thöni, M. (1991). Petrologic constraints for Eoalpine eclogite facies metamorphism in the Austroalpine Ötztal basement. *Mineralogy and Petrology*(43), pp. 237-254.
- Krenn, K. (2010). Fluid inclusions in quartz related to subsequent stages of foliation development during a single metamorphic cycle (Schneeberg Fault Zone, Eastern Alps, Austria). *Lithos*(118), pp. 255-268.
- Krenn, K., Kurz, W., Fritz, H., & Hoinkes, G. (2011). Eoalpine tectonics of the Eastern Alps: implications from the evolution of monometamorphic Austroalpine units (Schneeberg and Radenthein Complex). *Swiss Journal of Geosciences*(104), pp. 471-491.
- Leake, B., Mogessie, A., & Ettinger, K. (2004). Nomenclature of amphiboles: Additions and revisions to the International Mineralogical Association's amphibole nomenclature. *Mineralogical Magazine*(68), pp. 209-215.
- Leake, B., Woolley, A., Arps, C., Gilbert, M., Grice, J., Hawthorne, F., et al. (1997). Nomenclature of Amphiboles: Report of the subcommittee on amphiboles of the international mineralogical association, commission on new minerals and mineral names. *The Canadian Mineralogist*(35), pp. 219-246.
- Mauracher, J. (1980). Alpidische und voralpidische Metamorphose und Strukturprägung am Westende des Schneeberger Zuges (Ötztaler Alpen). *Unveröffentlichte Dissertation*.
- Miller, C., & Thöni, M. (1995). Origin of eclogites from the Austroalpine Ötztal basement (Tyrol, Austria): geochemistry and Sm-Nd vs Rb-Sr isotope systematics. *Chemical Geology*(122), pp. 199-225.
- Mogessie, A., Ettinger, K., & Leake, B. (2004). Nomenclature of amphiboles: Additions and revisions to the International Mineralogical Association's amphibole nomenclature. *Mineralogical Magazine*(68), pp. 209-215.
- Oberhänsli, R. (2004). Metamorphic structure of the Alps. *Mitteilungen der Österreichischen Geologischen Gesellschaft*(149), pp. 115-226.
- Passchier, C., and Trouw, R. (2005). *Microtectonics*. Berlin Heidelberg: Springer-Verlag.
- Purtscheller, F. (1969). Petrographische Untersuchungen an Aluminosilikatgneisen des Ötztaler-Stubai Altkristallins. *Tschermaks Mineralogisch Petrographische Mitteilungen*(13), pp. 35-54.
- Purtscheller, F. (1978). Ötztaler und Stubai Alpen. *Sammlung Geologischer Führer*(53).
- Schmid, S., Fügenschuh, B., Kissling, E., & Schuster, R. (2004). Tectonic map and overall architecture of the Alpine orogen. *Eclogae geologicae Helvetiae*(97), pp. 93-117.
- Schmidegg, O. (1964). Die Ötztale Schubmasse und ihre Umgebung. pp. 27-47.

- Schuster, R., & Stüwe, K. (2008). Permian metamorphic event in the Alps. *Geology*(36), pp. 603-606.
- Schuster, R., Koller, F., Hoeck, V., Hoinkes, G., & Bousquet, R. (2004). Metamorphic evolution of the Eastern Alps. *Mitteilungen der Österreichischer Mineralogischen Gesellschaft*(149), pp. 175-199.
- Schweigl, J. (1995). Neue geochronologische und isotopengeologische Daten zur voralpidischen Entwicklungsgeschichte im Ötztalkristallin (Ostalpen). *Jahrbuch der Geologischen Bundesanstalt*(138), pp. 131-149.
- Sölva, H., Grasemann, B., Thöni, M., Thiede, R., & Habler, G. (2005). The Schneeberg Normal Fault Zone: Normal faulting associated with Cretaceous SE-directed extrusion in the Eastern Alps (Italy, Austria). *Tectonophysics*(401), pp. 143-166.
- Sölva, H., Thöni, M., Grasemann, B., & Linner, M. (2001). Emplacement of eo-Alpine high-pressure rocks in the Austroalpine Ötztal complex (Texel group, Italy/Austria). *Geodinamica Acta*(14), pp. 345-360.
- Speckbacher, R. (2009). Die tektonometamorphe Entwicklung des Texel Komplexes: Strukturgeologie im Pfossental, Südtirol. *Unpublished master thesis*.
- Stipp, M., Stünitz, H., Heilbronner, R., & Schmid, S. (2002). The eastern Tonale fault zone: a 'natural laboratory' for crystal plastic deformation of quartz over a temperature range from 250 to 700 °C. *Journal of Structural Geology*(24), pp. 1861-1884.
- Thöni, M. (1981). Degree and evolution of the Alpine Metamorphism in the Austroalpine Unit W of the Tauern Window in light of K/Ar and Rb/Sr age determinations on Micas. *Jahrbuch der Geologischen Bundesanstalt*(124), pp. 111-174.
- Thöni, M., & Hoinkes, G. (1987). The Southern Ötztal Basement: Geochronological and Petrological Consequences of Eoalpine Metamorphic Overprinting. (H. Flügel, & P. Faupl, Eds.) *Geodynamics of the Eastern Alps*, pp. 379-406.
- Tropper, P., & Recheis, A. (2003). Garnet zoning as a window into the metamorphic evolution of a crystalline complex: the northern and central Austroalpine Ötztal-basement as a polymetamorphic example. *Mitteilungen der Österreichischen Geologischen Gesellschaft*(94), pp. 27-53.

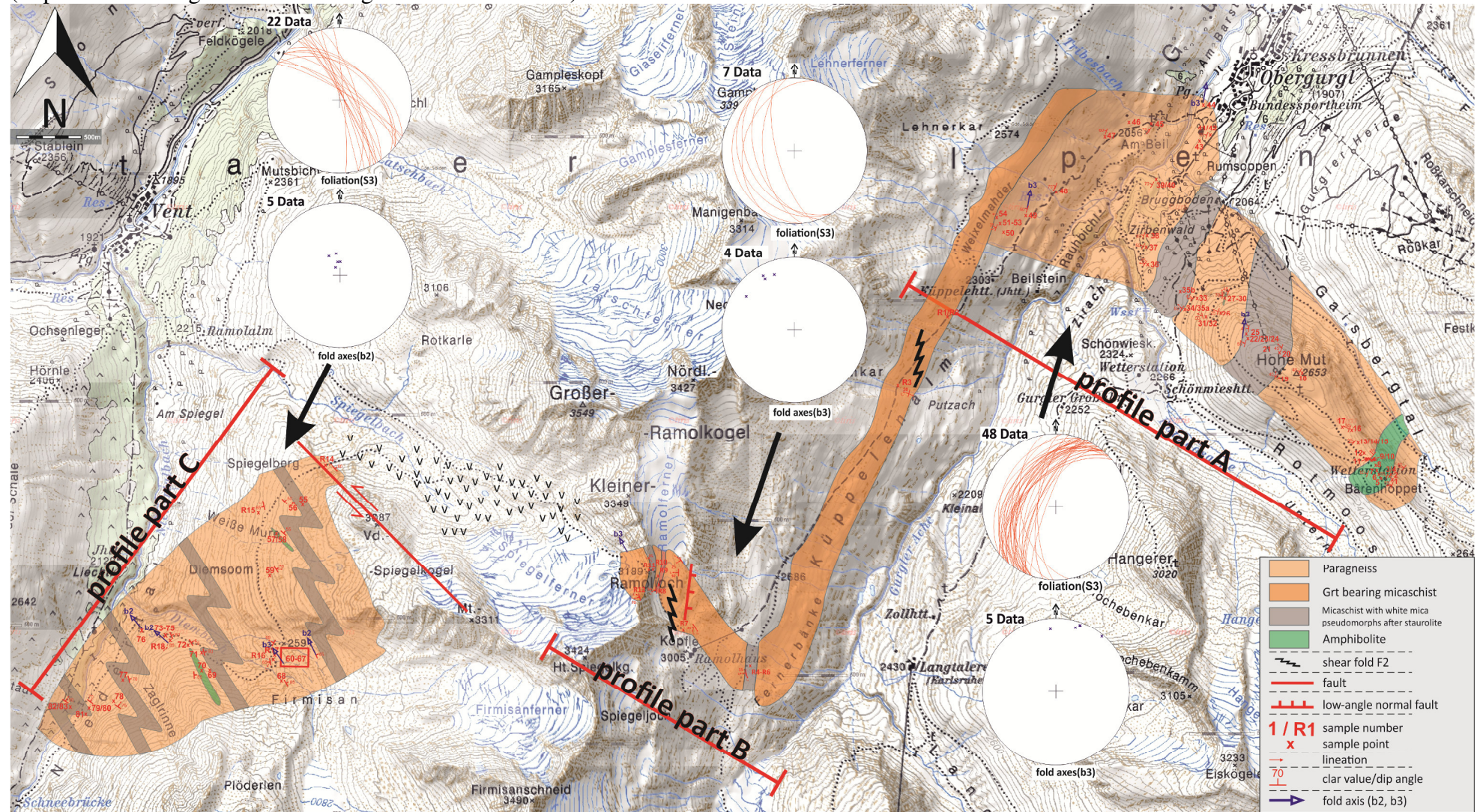
Figure Index

Figure 1 Sketch of the intracontinental subduction during Cretaceous times (modified after Krenn et al., 2011). PM Permomesozoic Cover; SCN Silvretta-Campo Nappe; SC Schneeberg Complex; TC Texel Complex; ÖC Ötztal Complex.....	3
Figure 2 Tectonic nappe subdivision of the Eastern Alps after Schmid et al. (2004). Red rectangle shows study area. PAL Periadriatic Lineament; EW Engadiner Window; SEMP Salzach-Ennstal-Mariazell-Puchberg Fault.....	4
Figure 3 Tectonostratigraphy after Schuster et al. (2004).....	5
Figure 4 (a-c) Sketches of the paleogeographic evolution from (a) Late Triassic to (c) Late Cretaceous times. G: Genf; W: Wien. (Schmid et al., 2004).....	6
Figure 5 (a/b) Austroalpine units at and around the study area after Tropper and Recheis (2003). Red rectangle points to study area. (b) Influence of Caledonian, Variscan and eo-Alpine metamorphism.	7
Figure 6 Geographical overview of the investigated area (from Google Earth, 2013). Yellow lines mark the sampled profiles.	10
Figure 7 Garnet micaschist with white mica pseudomorphs after staurolite. Ramolhut.	11
Figure 8 Garben schists arranged as boudins within folded paragneisses or micaschists. Diembach.....	12
Figure 9 Orthogneisses with large feldspar clasts. Vent village.	12
Figure 10 Sketch of deformation stages D0 to D5.	14
Figure 11 (a/b) Fold hinge with F3 fold axes plunging shallowly to the N. Hohe Mut/ Obergurgl village (c) Parasitic folds attributed to F3. (d/e) Isoclinal fold. Hohe Mut. (d) Dashed-dotted white line indicates axial plane foliation (S3). Black line characterizes the isoclinal parasitic fold of a large-scale tight fold (F3). (e) Sketch shows axial planes in red dipping to the NW; direction of the arrows illustrates the fold axes b3. (f) ECC-structure indicating N-directed shearing. Hohe Mut (g) Shear fold (F2) indicating NNE directed shearing (D2). Way up to the Ramolhut.	16
Figure 12 (a) More pronounced axial plane foliation in the micaschists (fold core), missing in the surrounding paragneisses. Near Ramolhut. (b) Meso-melanosome pygmatic folds in migmatized paragneisses. Near the Ramoljoch. (c) Z-shape fold structures (D3). Near the Ramoljoch.....	17

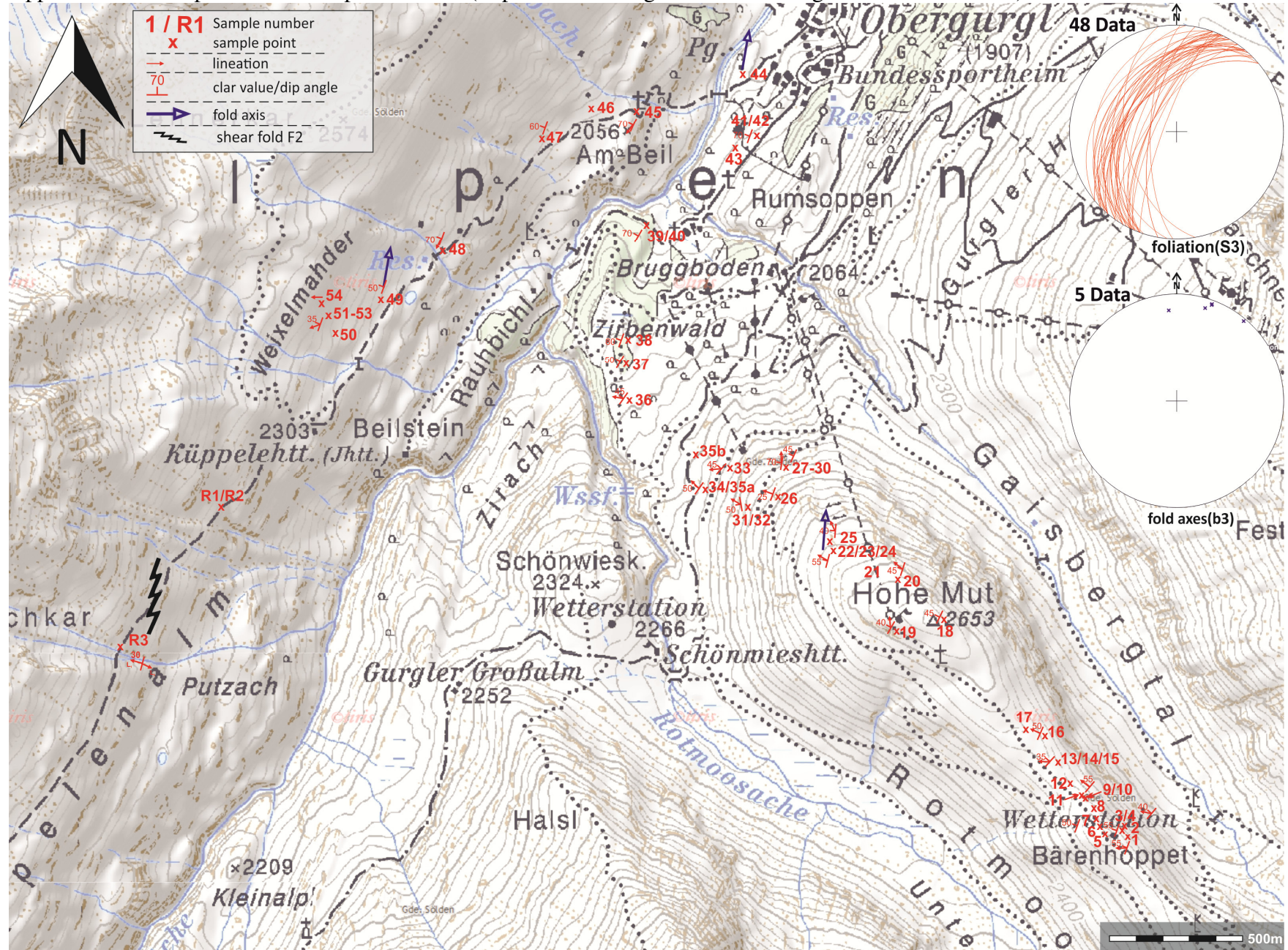
Figure 13 (a) Shear fold F2 and sigmoidal quartz clasts, both indicating shearing to the SE. Near Ramolhut. (b) Late ESE-directed normal faults.....	17
Figure 14 (a) Asymmetric shear fold F2. (b) Fold hinge attributed to F2 with steep NW dipping fold axis. Near Diembach.	18
Figure 15 (a) Superposition of shear fold F2 and fold F3, which results in a fold interference type O_2 after Grasemann et al. (2004). (b) Small-scale F2-parasitic structures. (c) Structural sketch of (a) for the fold interference type displayed in (d). Along Diembach (samples MS 60-68). (e) F2 and F3 fold structures. (f) SE-vergent F2 fold structure.	19
Figure 16 (a/b) Shear folds (F2) indicating a SE-directed shear sense. (c) D5-related en-echelon extension veins indicative for a vertical exhumation. (d) D5-related vein structure indicative for NW-directed shearing and vein opening. Near Diembach.....	20
Figure 17 (a) Besides GBM GBAR is the dominant deformation mechanism. (b) Mica band within heterogeneous paragneisses. (c) Strongly sericitized feldspar clasts. (d) Large garnets with no evidence for zonation. (e) Sigmoidal garnet porphyroclasts in mylonitic paragneiss indicative for NW-directed shearing. (f) Micafishes indicating vertical exhumation (average dip angle of 80°). Area at Diembach..	22
Figure 18 Most common garnet (grt) type along part A and B (a) garnet type I with inclusion-rich core and inclusions-less rim. (b) Garnet type II displays angular shape and sharp defined boundaries between inclusion-rich and inclusion-less rims. Garnet type II occurs only along a small area at the end of profile A, up to the Ramoljoch. Most common garnet type along part C (c/d) snowball garnets with inclusions of quartz (< 0.3 mm) and opaque phases in places.	23
Figure 19 (a) Characteristic staurolite (st) twins, replaced by white mica pseudomorphs after staurolite (white arrows). Inclusions within the extremely fine grained white mica and quartz matrix are garnet (grt, red arrows), tourmaline (tur, yellow arrows) and rutile (rt, blue arrows). (b) Pre- <i>eo</i> -Alpine foliation (S0) within staurolite. (c) Spaced foliation with microfolds in between. (d) Microlithons with coarse-grained mica.	24
Figure 20 Detailed amphibolite profile along a dm thick layered amphibolite at Bärenhoppet. (a) Polymetamorphic garnets (grt, red arrows) within an amphibole- and clinozoisite-rich matrix from type I amphibolite layer. Red circle points to inclusion-rich garnet core. (b) Type II amphibolite layer with characteristic foliation made up by large grains of clinozoisite (czo, blue arrows) and amphiboles (am). (c) Type II: Clinozoisite (blue arrows) and amphiboles (magenta arrow) under crossed nicols. (d) Type II: Fine grained layer composed of epidote (ep, yellow arrows) amphibole and quartz, as well as clinozoisite in places. (e) Type III amphibolite layer with large biotite (bt) porphyroblasts locally retrogressed to chlorite (chl). Blue and yellow arrows exhibit clinozoisite and epidote, respectively. (f) Type IV foliated fine grained amphibolite layer.	26
Figure 21 (a) Coarser grained amphiboles from profile C with inclusion-rich (quartz and opaque phases) type III garnet. (b) Local replacement of large amphiboles (up to 6mm) by biotite. (c) Fine grained amphiboles intercalated in foliated amphibolite layers. (d) Foliated amphibolite with white mica and quartz bands.	27
Figure 22 (a) Amphibole classification after Leake et al. (1997) and Mogessie et al. (2004). Analyzed amphiboles are identified as calcic. (b) Mineral chemistry of calcic amphiboles $(Na+K)_A < 0.5$ from samples R 13 and MS 60 in a $Mg/(Mg + Fe^{2+})$ vs. Si diagram after Leake et al. (1997) plot in magnesio- and ferrohornblende fields. (c) Calcic amphiboles $(Na+K)_A > 0.5$ from samples MS 6 and MS 75 plot in the edenite, pargasite and ferropargasite fields.	28
Figure 23 (a) Back scattered electron (BSE) image from amphiboles with inclusions of biotite (light purple), plagioclase (yellow arrow), titanite (orange arrows), apatite (red arrows) and ilmenite (pink arrows). (b) – (i) Element distribution images from amphiboles. (b) Si $K\alpha$; (c) Al $K\alpha$; (d) Mg $K\alpha$; (e) Ca $K\alpha$; (f) Fe $K\alpha$; (g) Ti $K\alpha$; (h) K $K\alpha$; (i) Na $K\alpha$;	29
Figure 24 Orthogneisses. (a) Characteristic Karlsbader twins (kfs, orange arrow) with perthitic exsolution of two feldspars (blue arrows). (c/d) Partly sericitized coarse-grained plagioclase (pl, yellow arrows) with exsolution lamellae in (d).	30
Figure 25 Sketch of the discussed study areas. Trend of the foliation (pointed lines) after Purtscheller (1978). A this study; B Sölvä et al (2001); C Exner et al. (2002); D Flöss (2009) and Speckbacher (2009);	32

Appendix

Appendix 1 Overall map of the studied profiles with field structures plotted on the lower hemisphere of the Schmidt net. (<https://www.tirol.gv.at/statistik-budget/tiris-kartendienste>)



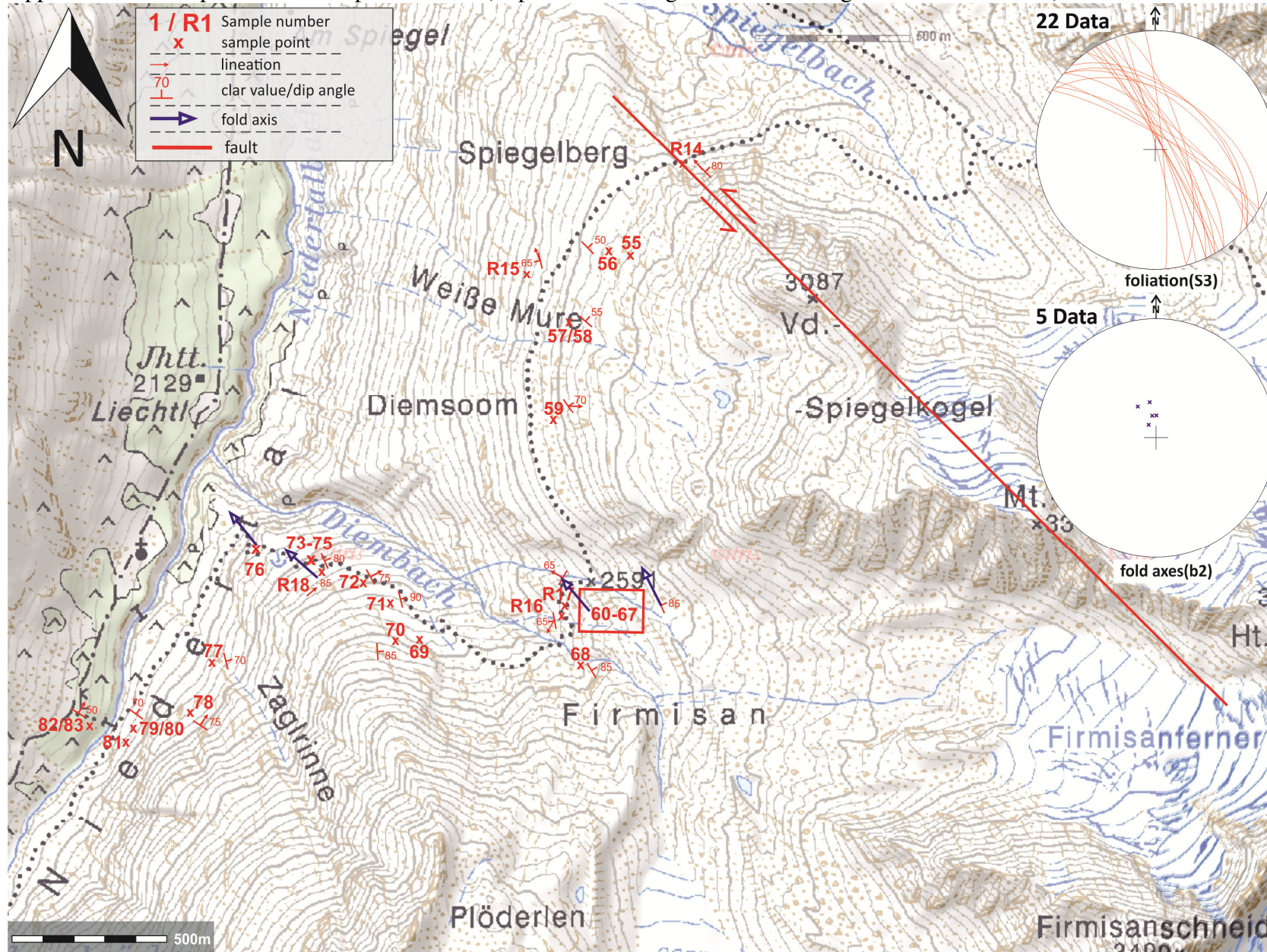
Appendix 2 Profile part A with sample locations (<https://www.tirol.gv.at/statistik-budget/tiris-kartendienste>).



Appendix 3 Profile part B with sample locations (<https://www.tirol.gv.at/statistik-budget/tiris-kartendienste>).



Appendix 4 Profile part C with sample locations (<https://www.tirol.gv.at/statistik-budget/tiris-kartendienste>).



Appendix 5 Used abbreviations.

Mineral abbreviations

am	Amphibole
ap	Apatite
bt	Biotite
cb	Carbonate
chl	Chlorite
cld	Chloritoid
czo	Clinozoisite
ep	Epidote
fsp	Feldspar
grt	Garnet
gr	Graphite
kfs	K-feldspar
ky	Kyanite
mca	Mica
qtz	Quartz
rt	Rutile
st	Staurolite
pm-st	white mica pseudomorphs after staurolite
ttn	Titanite
tur	Tourmaline
wm	White mica
zrn	Zircon

Other abbreviations

ÖC	Ötztal Complex
SC	Schneeberg Complex
TC	Texel Complex
N,E,S,W	North, East, South, West
Dn	Deformation increments
Sn	Foliation
Fn	Fold
bn	Fold axes
n	Number of deformation stage
GBM	Grain boundary migration
GBAR	Grain boundary area reduction

Appendix 6 Results of detailed petrography. X indicates presence of the mineral.

Appendix 6.1

Sample	Minerals															Accessory					Rock
	qtz	fsp	grt	bt	chl	mca	am	czo	ep	st	pm-st	ky	cb	cld	gr	tur	ttn	rt	zrn	ap	
MS1	X	X	X	X	X	X			X								X	X	X		Grt - bearing paragneiss
MS2	X	X	X	X	X	X			X									X	X		Grt - bearing paragneiss
MS3	X	X		X	X			X	X								X	X	X		Czo-ep - bearing amphibolite
MS4	X	X		X			X	X	X								X				Grt-czo-ep - bearing amphibolite
MS5	X	X	X				X	X	X				X				X	X			Czo-ep - bearing amphibolite
MS6	X						X	X	X								X	X			Czo-ep - bearing amphibolite
MS7	X						X	X	X				X								Czo-ep - bearing amphibolite
MS8	X	X		X	X		X	X	X								X	X		X	Czo-ep - bearing amphibolite
MS9	X		X	X			X		X												Czo-ep - bearing amphibolite
MS10	X		X	X	X		X	X	X												Czo-ep - bearing amphibolite
MS11	X	X	X	X		X												X			Grt - bearing paragneiss
MS12	X	X	X			X															Grt - bearing paragneiss
MS14	X	X	X	X	X	X										X		X			Grt - bearing paragneiss
MS15	X	X	X	X																	Grt - bearing paragneiss
MS17	X	X	X	X	X	X															Grt - bearing micaschist
MS19	X	X	X	X	X	X					X							X			Micaschist with pseudomorphs after st
MS20	X	X	X	X	X	X					X										Micaschist with pseudomorphs after st
MS21	X	X	X	X	X	X					X					X		X			Micaschist with pseudomorphs after st
MS22	X	X	X	X	X	X					X										Micaschist with pseudomorphs after st
MS23	X	X	X	X	X	X					X										Micaschist with pseudomorphs after st
MS24	X	X	X	X	X	X					X										Micaschist with pseudomorphs after st
MS25	X	X	X	X	X	X					X										Micaschist with pseudomorphs after st

Appendix 6.2

Sample	Minerals														Accessory					Rock	
	qtz	fsp	grt	bt	chl	mca	am	czo	ep	st	pm-st	ky	cb	cld	gr	tur	ttn	rt	zrn		ap
MS26	x	x	x		x	x															Grt-bearing micaschist
MS27				x			x		x									x	x		Amphibolite
MS28	x	x	x	x	x	x	x														Amphibolite
MS30	x			x	x		x	x	x				x								Czo-ep bearing amphibolite
MS31	x		x	x	x		x	x	x				x								Grt-czo-ep bearing amphibolite
MS32	x		x	x	x	x															Grt - bearing paragneiss
MS33	x	x	x	x	x	x												x	x		Grt - bearing paragneiss
MS34	x	x	x	x	x													x			Grt - bearing paragneiss
MS35	x	x	x	x	x	x															Micaschist with pseudomorphs after st
MS36	x	x	x	x	x	x												x			Grt - bearing paragneiss
MS37	x	x	x	x	x	x												x			Grt - bearing paragneiss
MS38	x	x	x	x	x	x												x			Grt - bearing paragneiss
MS39	x			x	x		x								x						Amphibolite
MS40	x	x	x	x	x	x												x			Grt - bearing paragneiss
MS41	x	x	x	x	x	x												x			Grt - bearing paragneiss
MS42	x	x	x	x	x	x												x			Grt - bearing paragneiss
MS43	x	x	x	x	x	x												x			Grt - bearing paragneiss
MS44	x	x	x	x	x	x												x			Grt - bearing paragneiss
MS45	x	x	x	x	x	x												x			Grt - bearing paragneiss
MS46	x	x	x	x	x	x												x	x		Grt - bearing paragneiss
MS47	x	x	x	x	x	x										x		x			Grt - bearing micaschist
MS48	x	x	x	x	x	x										x		x			Grt - bearing paragneiss

Appendix 6.3

Sample	Minerals															Accessory					Rock
	qtz	fsp	grt	bt	chl	mca	am	czo	ep	st	pm-st	ky	cb	cld	gr	tur	ttn	rt	zrn	ap	
MS49	x	x	x	x		x															Grt - bearing paragneiss
MS50	x	x	x	x	x	x										x					Grt - bearing micaschist
MS51	x	x	x	x	x	x												x			Grt - bearing micaschist
MS52	x	x	x	x	x	x			x							x		x			Grt - bearing micaschist
MS53	x	x	x	x	x	x												x			Grt - bearing paragneiss
MS54	x	x	x	x	x	x										x		x			Grt - bearing micaschist
R1	x	x	x	x		x															Grt - bearing micaschist
R2	x	x	x	x	x	x												x			Grt - bearing paragneiss
R3	x	x	x	x	x	x															Grt - bearing micaschist
R4	x	x	x	x	x	x					x										Micaschist with pseudomorphs after st
R5	x		x	x	x	x															Grt - bearing micaschist
R6	x		x	x	x	x					x			x	x				x		Micaschist with pseudomorphs after st
R7	x		x	x	x	x										x		x			Grt - bearing micaschist
R8	x	x		x	x	x			x							x					Orthogneiss
R9	x	x	x	x	x	x															Grt - bearing micaschist
R10	x		x	x	x	x					x										Pseudom. after st bearing micaschist
R11	x	x	x	x	x	x										x		x			Grt - bearing micaschist
R12	x	x	x	x	x	x										x					Grt - bearing micaschist
R13							x														Amphibolit
R14	x		x	x	x	x										x					Grt - bearing paragneiss
MS55	x		x		x	x					x					x		x			Micaschist with pseudomorphs after st
MS57	x	x	x	x	x	x															Grt - bearing paragneiss ± zoisite
MS58	x		x	x	x		x														Grt-Amphibolite

Appendix 6.4

Sample	Minerals															Accessory					Rock
	qtz	fsp	grt	bt	chl	mca	am	czo	ep	st	pm-st	ky	cb	cld	gr	tur	ttn	rt	zrn	ap	
MS59	x		x	x	x	x										x		x			Grt - bearing paragneiss
R16	x		x	x	x	x												x			Grt - bearing paragneiss
MS60							x	x	x				x				x				Czo-ep - bearing amphibolite
MS61	x		x	x	x																Grt - bearing paragneiss
MS62							x														Amphibolite
MS63	x		x		x		x	x					x						x		Czo-ep - bearing amphibolite
MS64	x		x	x	x	x	x								x				x		Grt - bearing paragneiss ± am
MS65	x	x	x	x	x	x															Grt - bearing paragneiss
MS66	x	x	x		x	x										x					Grt - bearing paragneiss ± zoisite
MS67	x	x	x	x	x	x													x		Grt - bearing paragneiss
MS68	x	x	x	x	x	x													x		Grt - bearing paragneiss
MS69	x		x		x	x													x		Quartzitic grt - bearing paragneiss
MS70	x		x	x			x						x								Amphibolite
MS71	x	x	x	x	x	x					x								x		Micaschist with pseudomorphs after st
MS72	x	x	x	x	x	x										x			x		Grt - bearing paragneiss
MS73	x		x	x	x	x										x			x		Grt - bearing paragneiss ± zoisite
MS74	x		x	x		x	x														Amphibolite
MS77	x	x	x	x	x	x					x					x			x		Micaschist with pseudomorphs after st
MS78	x	x	x	x	x	x													x		Grt - bearing paragneiss
MS79	x		x	x		x															Grt - bearing paragneiss
MS80	x	x	x	x	x	x					x								x		Micaschist with pseudomorphs after st
MS81	x	x	x	x	x	x					x					x			x		Micaschist with pseudomorphs after st
MS82	x	x	x	x	x	x					x								x		Micaschist with pseudomorphs after st
MS83	x	x	x	x	x	x					x	x							x		Micaschist with pseudomorphs after st

Appendix 7 Data of mineral chemical analysis of measured amphiboles.

Appendix 7.1

AMPHIBOLES

<i>Mineral</i>	Edenite	Edenite	Ferro- pargasite	Pargasite	Alumoferro- pargasite	Ferro- edenite
Sample no.	MS6_1	MS6_2	MS6_3	MS6_4	MS75_1	MS75_2
<i>Wt. %</i>						
SiO₂	44.56	43.90	42.16	43.26	42.92	43.02
TiO₂	0.50	0.48	0.55	0.54	0.48	0.39
Al₂O₃	11.45	12.21	13.21	12.71	14.86	13.74
Cr₂O₃	0.16	0.06	0.09	0.25	0.06	0.02
FeO	16.86	16.51	17.50	16.86	17.14	16.69
MnO	0.44	0.36	0.30	0.35	0.11	0.21
MgO	10.29	10.74	9.72	10.26	9.15	9.17
CaO	9.97	10.44	10.37	10.52	10.53	10.76
Na₂O	2.17	2.01	2.13	2.02	1.92	1.57
K₂O	0.28	0.38	0.62	0.47	0.51	0.55
F	0.25	0.16	0.18	0.37	0.44	0.30
Cl	0.01	0.00	0.00	0.00	0.06	0.13
Total	96.94	97.25	96.83	97.61	98.18	96.55
O = F, Cl	<i>0.11</i>	<i>0.07</i>	<i>0.08</i>	<i>0.00</i>	<i>0.20</i>	<i>0.16</i>
Total - O	96.832	97.183	96.754	97.454	97.981	96.394
<i>Normalization on the basis of 23 oxygens</i>						
Si	6.70	6.57	6.40	6.49	6.39	6.50
Al^[IV]	1.31	1.43	1.60	1.51	1.61	1.50
Total	8.00	8.00	8.00	8.00	8.00	8.00
Al^[VI]	0.72	0.72	0.76	0.74	1.00	0.95
Ti	0.06	0.05	0.06	0.06	0.05	0.04
Fe³⁺	0.00	0.00	0.00	0.00	0.00	0.00
Cr	0.02	0.01	0.01	0.03	0.01	0.00
Mg	2.31	2.40	2.20	2.30	2.03	2.07
Fe²⁺	1.84	1.77	1.93	1.83	1.89	1.91
Mn	0.06	0.05	0.04	0.04	0.01	0.03
Total	5.00	5.00	5.00	5.00	5.00	5.00
Fe²⁺	0.28	0.29	0.29	0.28	0.24	0.20
Ca	1.61	1.67	1.69	1.69	1.68	1.74
Na	0.12	0.03	0.02	0.03	0.08	0.06
Total	2.00	2.00	2.00	2.00	2.00	2.00
Ca	0.00	0.00	0.00	0.00	0.00	0.00
Na	0.51	0.55	0.61	0.56	0.48	0.40
K	0.05	0.07	0.12	0.09	0.10	0.11
Total	0.57	0.62	0.73	0.65	0.57	0.51
F	0.12	0.08	0.09	0.18	0.21	0.14
Cl	0.00	0.00	0.00	0.00	0.02	0.03
Total	15.57	15.62	15.73	15.65	15.57	15.51

Appendix 7.2

<i>Mineral</i>	Aluminoferro- pargasite	Ferro- pargasite	Ferro- pargasite	Magnesio- hornblende	Magnesio- hornblende	Magnesio- hornblende
Sample no.	MS75_4	MS75_5	MS75_6	MS60_1	MS60_2	MS60_3
<i>Wt. %</i>						
SiO₂	42.50	42.92	42.55	44.48	45.55	44.60
TiO₂	0.45	0.68	0.50	0.50	0.41	0.46
Al₂O₃	14.85	14.43	14.41	13.72	12.19	12.89
Cr₂O₃	0.01	0.05	0.10	0.11	0.00	0.05
FeO	16.82	16.79	16.65	15.34	15.20	15.12
MnO	0.17	0.11	0.14	0.24	0.23	0.19
MgO	8.75	8.74	9.01	9.82	10.66	10.77
CaO	10.59	10.95	10.59	10.98	11.01	11.18
Na₂O	1.79	1.78	1.84	1.54	1.30	1.43
K₂O	0.55	0.65	0.65	0.45	0.35	0.41
F	0.25	0.26	0.51	0.32	0.40	0.36
Cl	0.08	0.05	0.05	0.03	0.04	0.00
Total	96.81	97.41	97.00	97.53	97.34	97.46
O = F, Cl	0.12	0.12	0.23	0.14	0.18	0.15
Total - O	96.687	97.289	96.774	97.388	97.163	97.308
<i>Normalization on the basis of 23 oxygens</i>						
Si	6.40	6.43	6.42	6.59	6.74	6.61
Al^[IV]	1.60	1.57	1.58	1.41	1.26	1.39
Total	8.00	8.00	8.00	8.00	8.00	8.00
Al^[VI]	1.04	0.98	0.98	0.98	0.87	0.86
Ti	0.05	0.08	0.06	0.06	0.05	0.05
Fe³⁺	0.00	0.00	0.00	0.00	0.00	0.00
Cr	0.00	0.01	0.01	0.01	0.00	0.01
Mg	1.97	1.95	2.03	2.17	2.35	2.38
Fe²⁺	1.92	1.97	1.91	1.75	1.70	1.68
Mn	0.02	0.01	0.02	0.03	0.03	0.02
Total	5.00	5.00	5.00	5.00	5.00	5.00
Fe²⁺	0.20	0.14	0.19	0.15	0.18	0.19
Ca	1.71	1.76	1.71	1.74	1.75	1.78
Na	0.09	0.11	0.09	0.11	0.07	0.03
Total	2.00	2.00	2.00	2.00	2.00	2.00
Ca	0.00	0.00	0.00	0.00	0.00	0.00
Na	0.43	0.41	0.44	0.33	0.30	0.38
K	0.11	0.12	0.13	0.09	0.07	0.08
Total	0.54	0.53	0.57	0.42	0.37	0.46
F	0.12	0.12	0.24	0.15	0.19	0.17
Cl	0.02	0.01	0.01	0.01	0.01	0.00
Total	15.54	15.53	15.57	15.42	15.67	15.69

Appendix 7.3

<i>Mineral</i>	Magnesio- hornblende	Magnesio- hornblende	Magnesio- hornblende	Alumino- pargasite	Aluminomg- hornblende	Magnesio- hornblende
Sample no.	MS60_4	MS60_5	MS60_6	MS60_8	MS60_10	MS60_11
<i>Wt. %</i>						
SiO₂	45.18	45.44	44.80	43.28	43.88	44.77
TiO₂	0.39	0.48	0.51	0.48	0.43	0.42
Al₂O₃	12.47	11.56	13.00	15.10	14.62	12.53
Cr₂O₃	0.00	0.00	0.03	0.13	0.14	0.00
FeO	14.83	14.93	14.87	15.91	15.67	14.95
MnO	0.17	0.21	0.10	0.20	0.33	0.21
MgO	11.32	11.16	10.13	9.80	9.64	10.78
CaO	11.53	11.40	11.50	11.04	9.74	11.25
Na₂O	1.20	1.35	1.24	1.54	1.94	1.30
K₂O	0.38	0.32	0.36	0.54	0.38	0.33
F	0.30	0.33	0.27	0.38	0.27	0.24
Cl	0.01	0.01	0.03	0.01	0.01	0.01
Total	97.78	97.19	96.84	98.41	97.05	96.79
O = F, Cl	<i>0.13</i>	<i>0.14</i>	<i>0.12</i>	0.16	0.12	0.10
Total - O	97.651	97.049	96.72	98.248	96.934	96.687
<i>Normalization on the basis of 23 oxygens</i>						
Si	6.65	6.74	6.66	6.39	6.52	6.66
Al^[IV]	1.35	1.26	1.34	1.61	1.48	1.34
Total	8.00	8.00	8.00	8.00	8.00	8.00
Al^[VI]	0.81	0.76	0.94	1.01	1.08	0.86
Ti	0.04	0.05	0.06	0.05	0.05	0.05
Fe³⁺	0.00	0.00	0.00	0.00	0.00	0.00
Cr	0.00	0.00	0.00	0.02	0.02	0.00
Mg	2.48	2.47	2.24	2.16	2.14	2.39
Fe²⁺	1.64	1.69	1.75	1.74	1.68	1.68
Mn	0.02	0.03	0.01	0.03	0.04	0.03
Total	5.00	5.00	5.00	5.00	5.00	5.00
Fe²⁺	0.14	0.16	0.10	0.22	0.27	0.18
Ca	1.82	1.81	1.83	1.75	1.55	1.79
Na	0.04	0.03	0.07	0.03	0.18	0.02
Total	2.00	2.00	2.00	2.00	2.00	2.00
Ca	0.00	0.00	0.00	0.00	0.00	0.00
Na	0.30	0.36	0.29	0.41	0.38	0.35
K	0.07	0.06	0.07	0.10	0.07	0.06
Total	0.37	0.42	0.36	0.51	0.67	0.69
F	0.12	0.12	0.24	0.15	0.10	0.10
Cl	0.02	0.01	0.01	0.01	0.00	0.01
Total	15.37	15.42	15.36	15.51	15.67	15.69

Appendix 7.4

<i>Mineral</i>	Magnesio- hornblende	Edenite	Edenite	Magnesio- hornblende	Magnesio- hornblende	Magnesio- hornblende
Sample no.	MS60_12	R13_1	R13_1	R13_2	R13_3	R13_6
<i>Wt. %</i>						
SiO₂	44.24	43.31	43.31	44.74	44.80	46.93
TiO₂	0.45	0.86	0.86	0.50	0.61	0.34
Al₂O₃	13.41	12.72	12.72	13.43	13.38	10.90
Cr₂O₃	0.00	0.01	0.01	0.07	0.04	0.04
FeO	15.16	16.28	16.28	15.69	16.01	15.14
MnO	0.20	0.15	0.15	0.24	0.25	0.16
MgO	10.58	9.22	9.22	9.72	9.85	11.13
CaO	11.30	11.07	11.07	10.82	10.94	10.52
Na₂O	1.46	1.49	1.49	1.64	1.61	1.40
K₂O	0.41	0.95	0.95	0.46	0.53	0.45
F	0.46	0.00	0.28	0.28	0.28	0.17
Cl	0.00	0.00	0.00	0.01	0.00	0.03
Total	97.67	96.06	96.34	97.60	98.30	97.21
O = F, Cl	<i>0.19</i>	<i>0.00</i>	<i>0.12</i>	0.12	0.12	0.08
Total - O	97.476	96.06	96.222	97.48	98.182	97.132
<i>Normalization on the basis of 23 oxygens</i>						
Si	6.55	6.56	6.56	6.62	6.60	6.92
Al^[IV]	1.45	1.44	1.44	1.38	1.40	1.08
Total	8.00	8.00	8.00	8.00	8.00	8.00
Al^[VI]	0.89	0.83	0.83	0.97	0.92	0.81
Ti	0.05	0.10	0.10	0.06	0.07	0.04
Fe³⁺	0.00	0.00	0.00	0.00	0.00	0.00
Cr	0.00	0.00	0.00	0.01	0.01	0.01
Mg	2.34	2.08	2.08	2.15	2.16	2.45
Fe²⁺	1.70	1.97	1.97	1.79	1.81	1.68
Mn	0.03	0.02	0.02	0.03	0.03	0.02
Total	5.00	5.00	5.00	5.00	5.00	5.00
Fe²⁺	0.18	0.10	0.10	0.15	0.16	0.19
Ca	1.79	1.80	1.80	1.72	1.73	1.66
Na	0.02	0.11	0.11	0.14	0.11	0.15
Total	2.00	2.00	2.00	2.00	2.00	2.00
Ca	0.00	0.00	0.00	0.00	0.00	0.00
Na	0.40	0.33	0.33	0.34	0.35	0.25
K	0.11	0.12	0.13	0.09	0.11	0.12
Total	0.50	0.46	0.46	0.42	0.67	0.69
F	0.22	0.00	0.13	0.13	0.13	0.08
Cl	0.00	0.00	0.00	0.00	0.00	0.01
Total	15.50	15.46	15.46	15.42	15.67	15.69

Appendix 7.5

<i>Mineral</i>	Magnesio- hornblende	Ferro- hornblende	Magnesio- hornblende
Sample no.	R13_7	R13_8	R13_9
<i>Wt. %</i>			
SiO₂	46.96	44.06	51.26
TiO₂	0.62	0.70	0.37
Al₂O₃	9.39	13.62	6.84
Cr₂O₃	0.02	0.14	0.00
FeO	14.95	16.17	13.92
MnO	0.15	0.21	0.25
MgO	11.47	8.94	13.50
CaO	10.80	10.31	11.02
Na₂O	1.22	1.71	0.87
K₂O	0.59	0.74	0.21
F	0.36	0.25	0.17
Cl	0.00	0.03	0.02
Total	96.53	96.88	98.43
O = F, Cl	<i>0.15</i>	<i>0.11</i>	<i>0.08</i>
Total - O	96.378	96.768	98.354
<i>Normalization on the basis of 23 oxygens</i>			
Si	7.00	6.60	7.37
Al^[IV]	1.00	1.40	0.63
Total	8.00	8.00	8.00
Al^[VI]	0.65	1.00	0.53
Ti	0.07	0.08	0.04
Fe³⁺	0.00	0.00	0.00
Cr	0.00	0.02	0.00
Mg	2.55	2.00	2.89
Fe²⁺	1.72	1.88	1.51
Mn	0.02	0.03	0.03
Total	5.00	5.00	5.00
Fe²⁺	0.15	0.14	0.17
Ca	1.72	1.65	1.70
Na	0.13	0.20	0.13
Total	2.00	2.00	2.00
Ca	0.00	0.00	0.00
Na	0.23	0.29	0.11
K	0.11	0.14	0.04
Total	0.34	0.43	0.15
F	0.17	0.12	0.08
Cl	0.00	0.01	0.01
Total	15.34	15.43	15.15

Appendix 8 Sample locations with foliation and lineation. * indicates samples with a second lineation along foliation.

Appendix 8.1

Sample	Location		Foliation		Lineation	
	Latitude	Longitude	dip direction	dip angle	dip direction	dip angle
MS1	46°50'27.23"N	11° 2'23.01"E	290	55	270	50
MS2	46°50'27.50"N	11° 2'22.53"E	298	55		
MS3	46°50'27.83"N	11° 2'22.50"E	310	40	282	37
MS4	46°50'27.83"N	11° 2'22.50"E	310	40	282	37
MS5	46°50'27.33"N	11° 2'21.01"E				
MS6	46°50'28.54"N	11° 2'19.50"E				
MS7	46°50'29.99"N	11° 2'17.61"E	290	50		
MS8	46°50'31.89"N	11° 2'16.17"E				
MS9	46°50'32.66"N	11° 2'15.41"E				
MS10	46°50'32.66"N	11° 2'15.41"E	315	55		
MS11	46°50'33.53"N	11° 2'14.54"E	310	55	308	52
MS12	46°50'36.19"N	11° 2'10.77"E				
MS13	46°50'38.36"N	11° 2'7.35"E	312	35	272	30
MS14	46°50'38.36"N	11° 2'7.35"E				
MS15	46°50'38.36"N	11° 2'7.35"E				
MS16	46°50'45.44"N	11° 2'1.25"E	294	50	294	50
MS17	46°50'47.75"N	11° 1'56.76"E				
MS18	46°50'54.08"N	11° 1'49.01"E	296	45		
MS19	46°50'53.84"N	11° 1'43.92"E	300	40	355	25
MS20	46°50'55.84"N	11° 1'43.53"E	288	45	310	45
MS21	46°50'56.15"N	11° 1'42.40"E				
MS22	46°50'57.46"N	11° 1'39.19"E	300	40	280	40
MS23	46°50'57.46"N	11° 1'39.19"E	272	70	355	71
MS24	46°50'57.46"N	11° 1'39.19"E	305	50	300	50
MS25	46°50'58.11"N	11° 1'38.93"E	275	40	335	30
MS26	46°51'9.03"N	11° 1'21.65"E	290	25	290	25
MS27	46°51'12.26"N	11° 1'21.34"E	295	45		
MS28	46°51'12.26"N	11° 1'21.34"E	280	70	0	25
MS29	46°51'12.26"N	11° 1'21.34"E				
MS30	46°51'12.26"N	11° 1'21.34"E				
MS31	46°51'8.52"N	11° 1'18.49"E	300	55	320	45
MS32	46°51'8.52"N	11° 1'18.49"E	260	50	300	40
MS33	46°51'14.23"N	11° 1'13.03"E	312	45	265	40
MS34	46°51'8.37"N	11° 1'9.21"E	303	50	316	50
MS35a	46°51'8.37"N	11° 1'9.21"E	316	54		
MS35b	46°51'15.26"N	11° 1'7.05"E	293	50	293	50
MS36	46°51'23.59"N	11° 0'55.03"E	305	45	280	40
MS37	46°51'26.10"N	11° 0'55.37"E	300	50		
MS38	46°51'29.73"N	11° 0'54.83"E	290	80		
MS39	46°51'43.33"N	11° 0'59.06"E	296	70		
MS40	46°51'43.33"N	11° 0'59.06"E	305	70		
MS41	46°51'55.82"N	11° 1'21.60"E	295	65		
MS42	46°51'55.82"N	11° 1'21.60"E	280	70		
MS43	46°51'53.57"N	11° 1'15.98"E				
MS44	46°52'0.57"N	11° 1'16.03"E			17	10
MS45	46°51'56.36"N	11° 0'57.34"E	295	70	215	25
MS46	46°51'56.71"N	11° 0'48.33"E				
MS47	46°51'53.48"N	11° 0'41.92"E	290	60		
MS48	46°51'39.90"N	11° 0'22.59"E	293	70	206	35
MS49	46°51'35.43"N	11° 0'15.58"E	290	50	10	5
MS50	46°51'29.65"N	11° 0'4.38"E				
MS51	46°51'31.50"N	11° 0'3.12"E	295	35	250	15
MS52	46°51'31.50"N	11° 0'3.12"E				
MS53	46°51'31.50"N	11° 0'3.12"E			270	5
MS54	46°51'32.37"N	11° 0'3.21"E			270	5
R1	46°51'9.20"N	10°59'44.32"E				
R2	46°51'9.20"N	10°59'44.32"E				
R3*	46°50'52.81"N	10°59'26.43"E	285	30	115	5
R4*	46°49'49.05"N	10°58'20.68"E	265	15	165	5
R5	46°49'49.05"N	10°58'20.68"E				

Appendix 8.2

Sample	Location		Foliation		Lineation	
	Latitude	Longitude	dip direction	dip angle	dip direction	dip angle
R6*	46°49'49.05"N	10°58'20.68"E	250	45	175	10
R7*	46°49'53.39"N	10°58'6.37"E	240	35	200	30
R8	46°50'4.71"N	10°57'59.28"E	264	54	252	55
R9	46°50'5.10"N	10°57'58.92"E			270	30
R10*	46°50'5.56"N	10°57'58.50"E	240	25	310	10
R11	46°50'5.60"N	10°57'58.28"E			320	35
R12*	46°50'2.39"N	10°57'52.82"E	255	70	315	25
R13	46°50'18.81"N	10°57'31.18"E				
R14	46°50'34.13"N	10°55'55.99"E	45	80	320	30
MS55	46°50'21.26"N	10°55'48.49"E				
MS56	46°50'21.54"N	10°55'45.71"E	45	50		
MS57	46°50'15.93"N	10°55'37.09"E	40	55		
MS58	46°50'15.93"N	10°55'37.09"E				
R15	46°50'22.03"N	10°55'47.03"E	257	65	340	10
MS59	46°50'7.03"N	10°55'36.33"E	55	70	90	70
R16	46°49'43.38"N	10°55'41.76"E	260	65	210	55
MS60	46°49'42.98"N	10°55'42.04"E				
MS61	46°49'42.98"N	10°55'42.04"E	70	85		
MS62	46°49'42.98"N	10°55'42.04"E				
MS63	46°49'42.98"N	10°55'42.04"E	65	85		
MS64	46°49'42.98"N	10°55'42.04"E	65	85	330	85
MS65	46°49'42.98"N	10°55'42.04"E	60	85		
MS66	46°49'42.98"N	10°55'42.04"E	62	80	340	60
MS67	46°49'42.98"N	10°55'42.04"E	55	80	10	85
MS68	46°49'40.65"N	10°55'40.19"E	58	85		
MS69	46°49'45.13"N	10°55'18.30"E				
MS70	46°49'45.78"N	10°55'17.44"E	85	85	85	85
MS71	46°49'47.57"N	10°55'16.30"E	75	90		
MS72	46°49'49.15"N	10°55'14.31"E	60	75	60	75
MS73	46°49'52.24"N	10°55'6.61"E			310	65
MS74	46°49'52.24"N	10°55'6.61"E	65	75	65	75
MS75	46°49'52.24"N	10°55'6.61"E	60	85		
MS76	46°49'53.40"N	10°54'54.21"E			320	60
MS77	46°49'42.24"N	10°54'46.92"E	75	70		
MS78	46°49'38.88"N	10°54'43.39"E	32	75	32	75
MS79	46°49'37.45"N	10°54'36.31"E	40	50		
MS80a	46°49'37.45"N	10°54'36.31"E	35	80	35	80
MS80b	46°49'37.45"N	10°54'36.31"E	30	80		
MS81a	46°49'34.44"N	10°54'33.47"E	40	70		
MS81b	46°49'34.44"N	10°54'33.47"E				
MS82	46°49'35.37"N	10°54'31.16"E				
MS83	46°49'35.37"N	10°54'31.16"E	30	50	30	50